LIGHT TRAPPING IN SOLAR CELLS USING RESONANT NANOSTRUCTURES

Cover image: Crystalline silicon solar cell with metal-wrap-through front-contact pattern (copyright ECN). A mirror image of the solar cell can be seen in a flat uncoated Si wafer (on the left), which reflects more than 35% of the light. By using surface Si Mie nano-scatterers, the Si wafer can be made totally black (right), as the reflection is suppressed.

Ph.D. Thesis University of Amsterdam, December 2013
Light trapping in solar cells using resonant nanostructures
Pierpaolo Spinelli

ISBN 978-90-77209-76-9

A digital version of this thesis can be downloaded from http://www.amolf.nl.

LIGHT TRAPPING IN SOLAR CELLS USING RESONANT NANOSTRUCTURES

ACADEMISCH PROEFSCHRIFT

ter verkrijging van de graad van doctor
aan de Universiteit van Amsterdam
op gezag van de Rector Magnificus
prof. dr. D. C. van den Boom
ten overstaan van een door het college voor promoties
ingestelde commissie,
in het openbaar te verdedigen in de Agnietenkapel
op dinsdag 17 december 2013 te 10:00 uur

door

Pierpaolo Spinelli

geboren te Putignano, Italië

Promotiecommissie

Promotor:	Prof. dr. A. Polman
Overige Leden:	Prof. dr. T. Gregorkiewicz
	Prof. dr. R. E. I. Schropp
	Prof. dr. W. C. Sinke

Faculteit der Natuurwetenschappen, Wiskunde en Informatica

This work is part of the research program of the 'Stichting voor Fundamenteel Onderzoek der Materie' (FOM), which is financially supported by the 'Nederlandse organisatie voor Wetenschappelijk Onderzoek' (NWO). It is also funded by the European Research Council.

Contents

1

Introduction

1.1 Photovoltaics

Photovoltaics (PV) is the physical process of conversion of solar energy into electricity, by using semiconductor materials. The term photovoltaics is derived from the combination of the Greek word $\varphi\tilde{\omega}\varsigma$ (phōs) meaning "light" and the unit for electrical voltage, volt, named after the Italian physicist Alessandro Volta (1745-1827). Photovoltaic power generation typically uses solar modules, which are made of a number of interconnected solar cells. The physics and basic operation of a solar cell device is described in many academic textbooks [1–3], and we will not repeat this here. However, the importance of PV as a source of renewable energy, and its future perspectives are described first.

The average world power consumption in 2010 was 17 TW, and according to the International Energy Agency (IEA) this number is expected to double by 2050 [4]. In order to meet the increasing energy demand, we cannot rely on conventional fossil fuel sources (oil, carbon and gas) as their resources are limited and energy generation from these sources creates environmental pollution. Ideally, renewable and clean (i.e. CO_2-free) sources of energy must be used. Among these, PV has a great potential due to the virtually unlimited resources. The average amount of energy the Earth receives from the Sun is over 1000 times the total world consumption today. Even taking into account limited photovoltaic conversion efficiency of solar cells and the fact that only a small fraction of the surface of the Earth can be covered with solar panels, PV has the potential to become a major source of energy for our society.

An important reason that photovoltaics has not yet become a major source of energy so far is costs: in the past the cost of generating one kilowatt-hour of electric-

ity with solar panels was much higher than the cost of generating the same amount from fossil fuel sources or using nuclear energy. In the past few years however the cost of solar power has strongly decreased. At the same time, in the past decade the cost of "conventional" energy (while fluctuating in time) has strongly increased. In January 2013, the sales price of a crystalline Si solar module had dropped to only 0.69 $/Wp [5].

Today, about 0.1% of the total energy produced in the world is generated by photovoltaic systems [6]. While this is still a small number, the growth over the last ten years has been exponential and the share of solar energy in the total energy market is bound to increase rapidly. Figure 1.1, taken from the PV Status Report published by the Joint Research Center (JRC) [7], shows the cumulative installation of PV systems for the period 2000-2013. As can be seen, the installation of solar modules has soared over the last ten years, despite the world financial crisis that started in 2009. The total cumulative power installed up to 2012 was 100 GWp, with more than 70 GWp installed in Europe, with Germany and Italy the leaders.

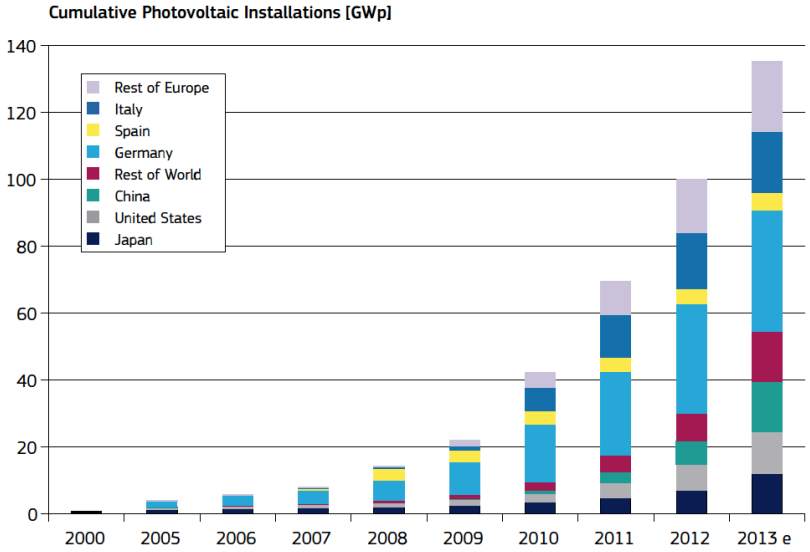

Figure 1.1: Cumulative solar module installation (MWp) for the period 2000-2013 (source: JRC PV Status Report 2013) [7].

The spectacular growth shown in Fig. 1.1 is due to many factors such as the reduced costs of solar modules, technological improvements that have lead to higher solar cell efficiencies and in some cases the introduction of government subsidies. Despite the impressive growth of PV installations worldwide, further advances in technology are required for PV to breakthrough as one of the major energy sources for our society.

1.2 Silicon solar cells

Silicon is the most widely used material for solar cells. Around 85% of the installed solar modules are based on Si [7]. Typical efficiencies of crystalline Si solar cell modules that are on the market today are between 15% and 21%. The world record efficiency for a crystalline Si solar cell is 25.0%, realized by the group of Green at the University of New South Wales (UNSW) in 1999, on a 4 cm^2 area cell [8]. This record still holds today.

A major factor limiting the efficiency of Si solar cells is carrier thermalization [1]. When a photon with energy higher than the bandgap energy is absorbed, at most an amount equal to the bandgap energy can be converted into electrical energy; the rest of the photon's original energy is lost by the creation of phonons [9]. This "quantum defect" effect is schematically shown in Fig. 1.2(a).

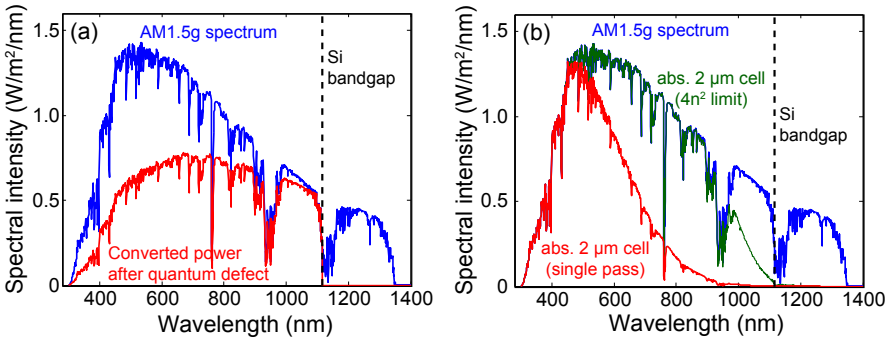

Figure 1.2: **(a)** Spectral intensity of the AM1.5 global solar spectrum (blue) and maximum spectral intensity that can be effectively converted to electricity, after taking into account quantum defect losses (red). **(b)** Spectral intensity of the AM1.5 global solar spectrum (blue) and spectrum that can be effectively absorbed by a 2 μm thick Si slab, in a single pass (red) and in the $4n^2$ limit (green). In both panels, the vertical dashed line indicates the Si bandgap wavelength (~1110 nm).

Figure 1.2(a) shows the spectral intensity of the AM1.5 global solar spectrum (blue), in the spectral range 300-1400 nm. The red line represents the spectral intensity that can be effectively converted to electricity assuming that every incident photon with an energy above the bandgap creates an electron-hole pair at an energy equal to the bandgap. As the wavelength is reduced below the bandgap, a progressively larger fraction of the incident photon energy is lost due to the quantum defect. The graph in Fig. 1.2(a) also shows a second important loss mechanism in the spectral range above the Si bandgap wavelength: photons with an energy smaller than the Si bandgap are not absorbed by the cell. The losses due to the quantum defect and above-bandgap losses can be tackled by using multi-junction cells [10, 11], which can be optically connected either in series (in a multi-layer stack) [12–14] or in parallel (with a spectrum-splitting element) [15–18]. The first concept has lead to devices with efficiencies up to 44.4% under

concentrated sunlight, but relies on expensive III-V semiconductors; the second concept is still in an early stage of development. In addition to this, so called third-generation photovoltaic concepts [19–21], such as quantum-cutting [22–25], quantum-pasting [24–26], multiple-exciton generation [27–29], hot-carrier collection [30, 31], and intermediate-band photovoltaics [32–34] are currently being investigated. Despite a large research effort, these third-generation concepts still await practical demonstration.

The theoretical efficiency limit for a single-junction solar cell, taking into account the quantum defect and above-bandgap photon losses, was first calculated by Shockley and Queisser in 1961 [35]. In this model for a p-n junction solar cell current is collected at a voltage determined by the quasi-Fermi level splitting in the semiconductor, which in turn is determined by the carrier collection and radiative recombination rates determined by detailed-balance thermodynamic arguments. Figure 1.3 shows the Shockley-Queisser (SQ) limit as a function of the bandgap energy of the solar cell material (black line). As can be seen, efficiencies up to 33.7% can be achieved for a semiconductor with a bandgap energy of 1.34 eV. The graph also shows the world record efficiencies, as of June 2013 [36], for crystalline Si (c-Si, red dot, 25.0%), GaAs (blue, 28.8%), InP (purple, 22.1%), copper-indium-gallium-selenide (CIGS, green, 20.4%), CdTe (light blue, 19.6%) and amorphous Si (a-Si, orange, 10.1%) solar cells. All world record efficiencies are well below the SQ limit. GaAs solar cells with a record efficiency of 28.8% come closest to the SQ limit (33.0% for a bandgap of 1.43 eV).

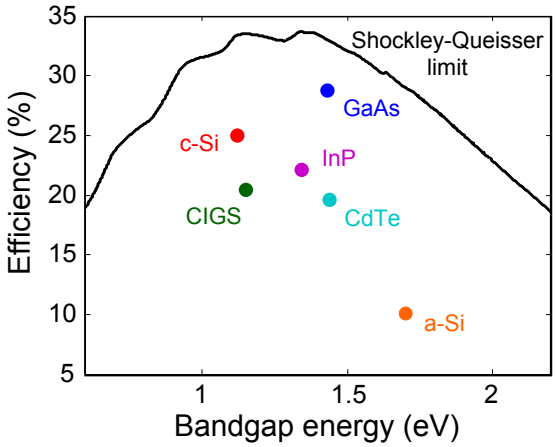

Figure 1.3: Shockley-Queisser efficiency limit as a function of the bandgap energy of the solar cell material (black line). The colored dots represent the current world record efficiencies for c-Si (red), GaAs (blue), InP (purple), CuInGaSe (CIGS, green), CdTe (light blue) and a-Si (orange) solar cells [36].

For a c-Si solar cell with a bandgap of 1.12 eV the SQ limit is 33.4%. This calculation however assumes a semiconductor in the radiative recombination limit, i.e. the

dark current of the p-n junction is not affected by non-radiative processes. In Si this limit cannot be achieved as Auger recombination, in which multiple carriers interact, is a loss mechanism that cannot be neglected. Moreover, due to the indirect bandgap, the radiative emission rate of Si is small, and competing non-radiative processes at impurities, point defects, grain boundaries and surfaces cannot be neglected.

Table 1.1 reports the short-circuit current (J_{SC}), open-circuit voltage (V_{OC}), fill factor (FF) and efficiency (η) of the best and second-best efficiency c-Si solar cells reported in the literature so far (first two rows). The short-circuit current, or the photocurrent at zero voltage, is directly related to the solar intensity spectrum, and is taken for 1-sun illumination; for Si, it is 43.8 mA/cm^2 assuming full absorption of the AM1.5 global solar spectrum (ASTM G173) [37] up to the bandgap and 100% photon-to-electron conversion efficiency. The open-circuit voltage, i.e. the voltage without current load, is much lower than the Si bandgap and is determined by the quasi-Fermi level splitting in the solar cell, which is in turn determined by the carrier densities across the p-n junction. Non-radiative recombination thus strongly affects V_{OC}. The theoretical maximum of V_{OC} depends on the cell thickness as thicker cells suffer from larger bulk recombination. For a 160 μm thick cell, and including Auger recombination, V_{OC} for a c-Si solar cell is calculated to be 770 mV [38]. The fill factor, defined as the maximum achievable power per unit area JV relative to the product $J_{SC}V_{OC}$, reflects the contribution of non-radiative recombination as well as that of series resistance in the Si wafer and the contacts and shunt resistance across the junction.

c-Si solar cell	*J_{SC} (mA/cm^2)*	*V_{OC} (mV)*	*FF*	*η*	*Ref.*
UNSW (PERL, >400 μm)	42.7 (43.8)	706 (760*)	82.8%	25.0%	[8]
Panasonic-Sanyo (HIT, 98 μm)	39.5 (43.8)	750 (780*)	83.2%	24.7%	[39]
Ideal cell (160 μm)	*43.8*	*770**	*83.2%*	*28.1%*	*[38]
Ideal cell (10 μm)	*43.8*	*810**	*83.2%*	*29.5%*	

Table 1.1: Short-circuit current (J_{SC}), open-circuit voltage (V_{OC}), fill factor (FF) and efficiency (η) measured for the best and second best c-Si solar cells (first and second row, respectively), and for two ideal cells with thickness 160 μm and 10 μm (third and fourth row, respectively). The calculated "ideal" J_{SC} for full light absorption and "ideal" V_{OC} (from Ref. [38]) for each thickness are indicated between brackets.

The world record efficiency Si solar cell is a passivated-emitter-rear-locally-diffused (PERL) p-n homo-junction cell realized at UNSW [8]. As can be seen, the J_{SC} is close to the maximum limit, indicating that the cell shows almost perfect absorption of the solar spectrum above the bandgap. This was achieved by using an effective inverted pyramid light-trapping scheme in combination with a Si_3N_4 antireflection coating and a relatively large cell thickness (>400 μm). However, the large cell thickness resulted in enhanced bulk carrier recombination that, together

with the highly recombination-active doped diffused emitter, limited the V_{OC} to 706 mV. This yields an efficiency of 25.0%.

The second-best efficiency c-Si solar cell is a hetero-junction-with-intrinsic-thin-layer (HIT) cell, made by Panasonic-Sanyo in 2013 [39]. This hetero-junction cell is based on a much thinner c-Si wafer (98 μm), on which a few-nanometer-thick hydrogenated amorphous Si (a-Si:H) layer is deposited to form a crystalline-amorphous Si hetero-junction. The advantage of the hetero-junction design is that no highly doped regions are required, thus reducing bulk carrier recombination. The relatively small thickness of the cell, the absence of a highly-doped emitter layer and the excellent surface passivation properties of a-Si yield V_{OC} as large as 750 mV. However, in these cells J_{SC} is limited by parasitic losses in the transparent conductive oxide (TCO) top contact layer and the a-Si:H layer. The reported efficiency of the best hetero-junction cell is 24.7%. If the light absorption in the active layer of the hetero-junction solar cell could be enhanced the efficiency could be increased further.

The third and fourth rows of Table 1.1 show the electrical characteristics of two ideal homo-junction cells with thicknesses of 160 μm and 10 μm, respectively. For both cell thicknesses, we assume maximum J_{SC} of 43.8 mA/cm^2. For V_{OC} we take optimum values calculated for thick (770 mV) and thin (810 mV) cells. We take the FF equal to that of the Panasonic-Sanyo HIT cell. The resulting efficiencies are 28.1% and 29.5% for the thick and thin cells, respectively. The higher efficiency of the thinner cell is due to the lower bulk recombination.

Table 1.1 defines the road to achieve c-Si solar cells with efficiency approaching the Shockley-Queisser limit. First, reducing the solar cell thickness is crucial to obtain high V_{OC}. Simultaneously, the use of thinner Si wafers allows a reduction in fabrication costs, as the Si wafer accounts for a significant fraction of the cost of a crystalline Si solar module [5]. Furthermore, perfect absorption of the solar spectrum is needed to achieve optimum J_{SC}. Finally, for thinner cells excellent surface passivation is crucial to achieve large V_{OC}.

Achieving all these goals at the same time time is a major challenge. The first challenge is to absorb the full solar spectrum in a thin Si layer. Figure 1.2(b) shows the spectral intensity of the AM1.5 global solar spectrum (blue), and the spectral intensity absorbed in a single pass through a 2-μm-thick Si slab (red). As can be seen, a significant fraction of the solar spectrum in the spectral range 600-1100 nm is not absorbed by the thin layer. In particular, photons in the near-bandgap spectral range are very poorly absorbed. In order to enhance absorption, a light-trapping scheme is essential. Light-trapping can be achieved by using scattering structures that increase the optical path length in the cell and/or trap light by total internal reflection [40].

The green line in Fig. 1.2(b) shows the maximum spectral intensity that can be absorbed in a 2-μm-thick Si cell using light trapping schemes in the classical ray-optics limit [41]. This is usually referred to as "$4n^2$ limit" as it has been shown that the maximum optical path length enhancement that can be achieved in a Si slab with Lambertian scattering surfaces is equal to $4n^2 = \sim 50$, where n is the refractive

index of Si [42]. As can be seen, even in the $4n^2$ limit, light in the spectral range near the bandgap of Si is not fully absorbed in a 2-μm-thick layer.

Conventional c-Si solar cells use micron-sized pyramidal surface texture as a light-trapping scheme [43, 44]. This geometry however cannot easily be applied to devices thinner than 20 μm, as the typical feature size is several microns. Furthermore, surface texture increases the surface area of the cell, and thus leads to enhanced surface recombination. Therefore, it is of great interest to investigate novel light scattering architectures that can serve to efficiently couple and trap light into thin Si layers. In the past few years, it is being realized that nanostructures integrated with the solar cell can serve to couple and trap light in the solar cell [40]. Nanostructures also offer the possibility to be integrated with passivated flat Si layers, without harming the surface passivation properties of the cell [45, 46].

In this thesis, we study the integration of metallic and dielectric resonant nanostructures with c-Si wafers and films, and study enhanced light absorption and light trapping. The implications for enhanced solar cell performance are discussed.

1.3 Resonant nanostructures for light management

The research field of Nanophotonics studies the behavior of light at the scale of nanometer, i.e. at a scale comparable to or smaller than the wavelength of light. The "elementary particles" of this field are metallic and dielectric nanoparticles (NPs) that can show resonant interaction with light.

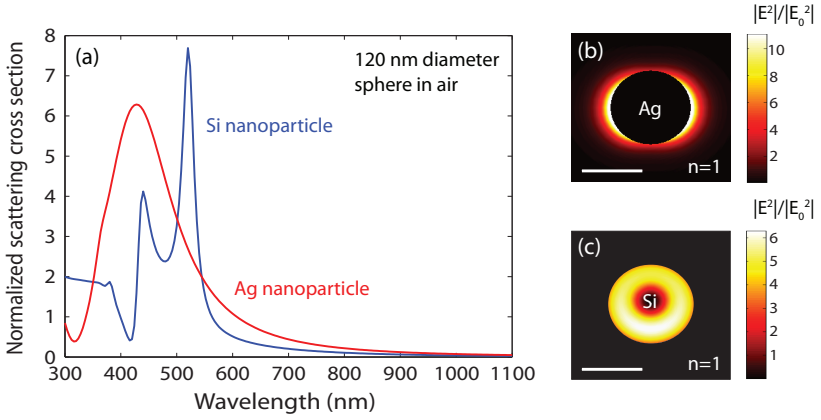

Figure 1.4: **(a)** Normalized scattering cross section spectra for a 120-nm-diameter Ag (red) and Si (blue) nanoparticle in air. **(b)** Electric field distribution for a localized surface plasmon resonance for Ag and **(c)** Mie resonance for Si. Scale bars represent 100 nm.

Figure 1.4(a) shows the normalized scattering cross section of a 120-nm-

diameter Ag (red) and Si (blue) sphere in air. The normalized scattering cross section is defined as the particle scattering cross section divided by its geometrical cross section (i.e. the NP projected area). The spectrum for a Ag NP shows a clear resonance at a wavelength of 430 nm, whereas for the Si NP two resonances are observed, at wavelengths of 440 nm and 520 nm. The nature of these optical resonances in a Ag and Si nanoparticle is very different, due to the intrinsic difference in the optical constants of metals and dielectrics. Metal NPs are characterized by localized surface plasmon resonances (LSPRs), which originate from the collective excitation of the free electrons in the metal by the electric field of the incident light [47]. At resonance, the field is confined at the NP surface (Fig. 1.4(b)). Dielectric nanoparticles, on the other hand, possess geometrical resonances where light is confined in a well-defined geometrical mode inside the NP [48]. Figure 1.4(c) shows the electric field distribution inside the Si NP, for the resonance at 520 nm. The geometrical resonances are also called Mie resonances, after the German physicist Gustav Mie (1869-1957) who first solved the Maxwell's equation for a plane wave incident on a spherical particle in a homogeneous medium. Note that Mie theory holds for particles made of any material, i.e. both dielectrics and metals. However, the different dielectric permittivity of metals and dielectrics results in the distinctly different resonance spectra and field distributions shown in Fig. 1.4(a) and Figs. 1.4(b,c). For both metallic and dielectric NPs, the scattering cross section at resonance can be as large as 5-10 times the NP geometrical cross section. This means that when a material is covered with an array of NPs with surface coverage of only 10-20% nearly full interaction with incident light with the scattering nanostructures can be achieved.

The strong resonant scattering of light by metallic or dielectric nanoparticles can be used to couple and guide light in thin solar cells. To do so, the relatively narrowband resonances shown in Fig. 1.4(a) need to be made broadband. As we will show in this thesis, this can be done by changing the NP size, shape or distribution, as well as the degree of coupling to the substrate. Furthermore, as it turns out, light scattering from the NPs occurs preferentially in the forward direction, into the solar cell, due to the high density of optical states in the substrate, in particular for high-index materials.

In the past few years, several designs for "light management" in solar cells using resonant nanostructures have been proposed [40]. They include designs in which NPs are placed at the front [49–55], at the back [56–65] or inside the solar cell active layer [66–73]. Despite this earlier work, fundamental understanding of the light scattering and trapping phenomena in solar cells with metallic and dielectric nanoparticles is lacking.

In this thesis we investigate the fundamental aspects of resonant scattering of light by metallic and dielectric nanoparticles placed on top of a high-index Si substrate. The novel insights gained by these fundamental studies enable future studies of light trapping architectures for solar cells with higher efficiency. We discuss several practical implementations of nanostructures in solar cell devices.

1.4 Thesis outline

In this thesis, each of the Chapter 3 - 9 presents an advance in understanding the scattering properties of metallic (Chapters 3 - 5) and dielectric (6 - 9) NPs for application to light trapping in solar cells.

Chapter 2 introduces the nanofabrication techniques used in some of the following chapters to fabricate the nanoparticles. Substrate conformal imprint lithography (SCIL) is presented as a large area, non-expensive, high-fidelity technique to fabricate NP arrays on full wafers. Furthermore, a reactive ion etching (RIE) recipe based on fluorine compound gases is used to fabricate Si nano-pillar arrays on large-area Si wafers.

In **Chapter 3**, we study the scattering of light by plasmonic (Ag) NPs placed on a substrate. In particular, the key role of Fano resonances is identified and used to define guidelines for designing a plasmonic antireflection coating (ARC) for Si solar cells.

Based on these results, a plasmonic ARC with better performance than a standard flat Si_3N_4 ARC is presented in **Chapter 4**. This is a result of a full parameter space optimization carried out with numerical simulations. We use electron beam lithography (EBL) to fabricate Ag NP arrays on crystalline Si solar cells. Reflection spectroscopy is used to quantify the light coupling into the Si solar cells.

Chapter 5 explores the possibility to use the near-field enhancement of plasmonic (Ag) NPs embedded in a solar cell, to enhance the optical absorption in the active layer. We find that this approach is strongly limited by the Ohmic losses in the metal NP, and cannot be used for crystalline or amorphous Si solar cells. However, it can be used to enhance the absorption of light in ultrathin organic/polymer based solar cells.

In **Chapter 6**, a new way of suppressing the reflection of light from a Si surface is presented. The reflectivity of a full-size Si wafer is reduced from over 35% to 1.3% (averaged over the solar spectrum) by covering the wafer with an optimized array of Si Mie resonators. The wafer patterned with a Si NP array appears thus completely black. The fundamental physics of light scattering by Mie resonances in the Si NPs is studied.

The same Si Mie coating is used in **Chapter 7** to study light trapping in thin (20-100 μm) and ultrathin (1-20 μm) crystalline Si solar cells. Numerical simulations are used to calculate the absorption in the thin Si slab covered with the Si Mie coating. An electrical model including bulk and surface recombination is then used to estimate the solar cell efficiency. We find that for realistic values of surface recombination velocity and carrier bulk lifetime, a 20-μm-thick cell with 21.5% efficiency can be made.

Chapter 8 presents an experimental demonstration of light trapping in thin film Si slabs on glass, patterned with arrays of Si Mie NPs. Total reflection and transmission spectroscopy is used to measure the absorption spectrum of the thin Si slab with the Si Mie coating, and compare it to that of a flat Si slab. In the infrared spectral range, optical path length enhancements up to a factor of 65 are measured,

well beyond the geometric Lambertian $4n^2$ limit for Si at this wavelength.

In **Chapter 9**, a TiO_2/Al_2O_3 Mie coating is presented. This coating combines very good antireflection properties with excellent surface passivation. The antireflection effect stems from the preferential forward scattering of light by Mie resonances in the TiO_2 NPs and yields a solar-spectrum averaged reflectivity as low as 1.6%. An ultrathin Al_2O_3 layer provides excellent passivation of the Si surface, with surface recombination velocity of only 3.3 cm/s after fabrication of the TiO_2 NPs.

Finally, **Chapter 10** presents several new concepts and ideas for integrating plasmonic and Mie NPs on realistic solar cell designs. We show that resonant nanostructures can be beneficial not only for several crystalline Si solar cell designs, but also for GaAs and polymer cells. Practical aspects such as the effect of polymer and glass encapsulation of solar modules are also analyzed.

Altogether, this thesis provides fundamental insights in light scattering and trapping phenomena of resonant metallic and dielectric nanostructures integrated with thin and thick Si wafers. The results may be used to design novel Si solar cell architectures with higher efficiency that can be made at lower costs.

2

Nanofabrication techniques

We present the nanofabrication procedures used to make large-area arrays of Si and TiO_2 nanopillars on Si substrates. We use substrate-conformal imprint lithography (SCIL) and reactive ion etching (RIE) to fabricate Si nanopillars arrays on a Si wafer. A RIE recipe using CHF_3, SF_6 and O_2 gases is optimized to yield a smooth, anisotropic Si etch, with a ~1:3 selectivity with respect to SiO_2. The TiO_2 nanopillars are obtained by means of evaporating TiO_2 in a nanoimprinted resist hole pattern, followed by lift-off of the resist.

2.1 Introduction

Nanofabrication refers to the realization of 1-, 2- or 3-dimensional structures with length scales below 100 nm. Common nanofabrication techniques used in research studies include electron bean lithography (EBL) and focused ion beam (FIB) milling. Both techniques offer the possibility to fabricate arbitrary patterns on a wafer surface. However, both processes are relatively slow and expensive. They can thus be used to pattern small areas (typically a few mm^2) but are not usable for industrial scale production. Deep ultra-violet interference lithography can be used to pattern large-area wafers. However, the resolution of this technique is limited to the diffraction limit of light. Furthermore, only periodic or quasi-periodic arrays can be fabricated. Nanoimprint lithography techniques offer the possibility to fabricate arbitrary patterns on a large scale. These techniques are

based on the replication of a master pattern by means of a stamping process in which a stamp with inverse pattern is brought in physical contact with a resist material and used to mold the master pattern into the resist. Usually nanoimprint lithography is based on either a rigid stamp, which offers better resolution but can only be used on small flat substrates, or a soft stamp, which offers more flexibility but poorer resolution. Recently, substrate-conformal imprint lithography (SCIL) has shown to be capable to fabricate nanostructures with resolution below 10 nm, over large-area substrates [74, 75]. In this chapter, we describe the use of SCIL to fabricate dielectric nanoparticles on top of a Si wafer, for application to solar cell devices.

2.2 SCIL for fabrication of dielectric nanoparticles

In SCIL, a master pattern is first made, usually on a Si wafer, by EBL or interference lithography followed by reactive ion etching (RIE). Then, a poly-di-methyl-siloxane (PDMS) stamp is molded from the master wafer. The stamp is composed of 2 layers of PDMS: a high-Young's modulus layer (H-PDMS) holding the features, which gives features with sharper corners and avoids adjacent features from collapsing or sticking to each other; and a low-Young's modulus PDMS layer, which is flexible and hence allows conformal contact to the substrate. The flexible stamp can then be applied either by a dedicated SCIL imprint mechanical tool or by hand onto a sol-gel resist layer spin-coated on the sample. The sol-gel resist used contains silicon oxide precursors, specifically tetramethylorthosilicate (TMOS, or $Si(OCH_3)_4$) and methyltrimethoxysilane (MTMS, or $C_4H_{12}O_3Si$). Several reactions take place during the sol-gel formation and nanoimprint [74]. The net result of these reactions is the formation of O-Si-O bonds, which form a porous SiO_2 layer [74].

Figure 2.1(a) and 2.1(b) shows schematics of two different SCIL sequences used to fabricate large-area arrays of dielectric nanoparticles. Figure 2.1(a) shows a schematic of the procedure used to fabricate arrays of Si nanopillars on a Si(100) wafer. A silica sol-gel resist is spin-coated on the Si wafer at 800 rpm for 45 s, followed by a very short 1000 rpm spin to remove the thick liquid resist on the edges. This procedure yields a total resist thickness of about 70 nm. A PDMS stamp patterned with a square array of circular holes is then applied by hand on the wafer to perform the SCIL. Due to capillarity forces the sol-gel resist easily fills the nanoholes in the PDMS stamp. After a curing period of 20 min, the stamp is removed and an array of sol-gel nanopillars is obtained. The height, diameter and spacing of the nanopillars are fully controlled by the stamp design. For the experiments described in this chapter, the sol-gel nanopillars have a height of 100 nm, diameter of 250 nm and the inter-particle spacing of the square array is 450 nm. A residual sol-gel layer of about 40 nm is left over in between the nanopillars and the Si wafer after the nanoimprint. The sol-gel nanopillar array is then transferred to the Si wafer by means of a double-step reactive ion etch (RIE) process. The first step is a breakthrough etch of the residual sol-gel layer, performed by using a mixture of

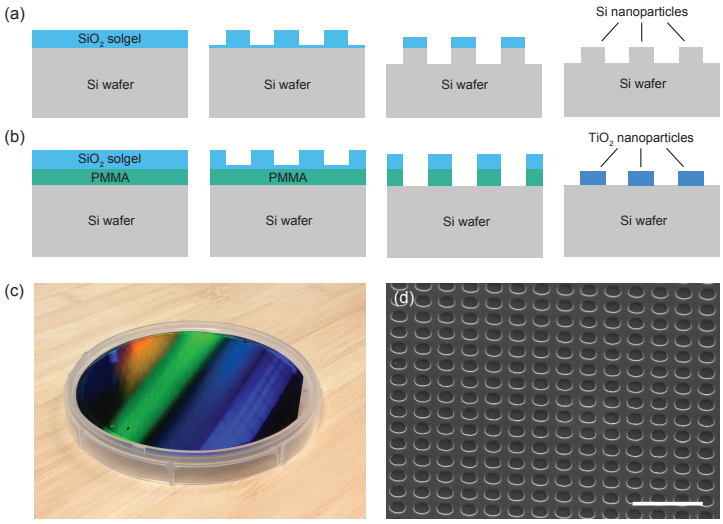

Figure 2.1: **(a)** Schematic of the nanoimprint fabrication procedure used to make Si nanopillar arrays. **(b)** Schematic of the nanoimprint fabrication procedure used for TiO_2 nanopillar arrays. **(c)** Full 4-inch Si wafer nanopatterned with sol-gel nanopillars. **(d)** SEM image of a hole pattern in a sol-gel layer after the nanoimprint with SCIL (scale bar is 1.5 μm).

CHF_3 and Ar gases. The second RIE step is the actual transfer etch into the Si wafer, and is performed by using a mixture of SF_6, CHF_3 and O_2, as will be discussed in the following paragraph. After the RIE, the residual silica sol-gel mask is etched away with a 1% HF solution in water.

Figure 2.1(b) shows a schematic of the procedure used to fabricate arrays of TiO_2 nanopillars on a Si(100) wafer. First, a PMMA (35k) resist layer is spin-coated on the Si wafer at 1000 rpm for 45 sec, yielding a thickness of about 300 nm. This thickness can be tuned by changing the spin-coating rotation speed; it should be chosen as ~3 times the desired height of the TiO_2 nanoparticles. A low-bias O_2 plasma etch is then performed for 3s in order to make the PMMA surface hydrophilic. Next, a sol-gel layer is spin-coated in a similar manner as described for Fig. 2.1(a). The SCIL nanoimprint is performed using a PDMS stamp patterned with a square array of nanopillars. In this case, a pattern of holes is obtained in the sol-gel layer after curing and stamp removal. The pattern of holes is then transferred to the PMMA by means of a double-step breakthrough RIE process, including a CHF_3/Ar etch of the residual sol-gel layer and an O_2 etch of the PMMA resist. The O_2 etch is deliberately carried out for a long time (12 min), in order to create an undercut profile in the resist to facilitate the lift-off process. A TiO_2 layer is then deposited by means of electron beam (e-beam) evaporation and subsequently lift-off is performed by dissolving the PMMA in acetone at 50°C. This leaves an array of TiO_2 nanopillars on the Si surface.

Figure 2.1(c) shows a photograph of a 4-inch wafer that is fully patterned with sol-gel nanopillars by manually applying the PDMS stamp. The color effects are caused by diffraction of light by the grating formed by the nanopillars. A few black spots can be noticed on the surface, as a result of small air inclusions during the SCIL nanoimprint. Figure 2.1(d) shows a scanning electron microscope (SEM) image of an array of holes imprinted in sol-gel resist.

2.3 Si reactive ion etching

Reactive ion etching (RIE) is used to transfer the SiO_2 sol-gel nanopattern into the Si wafer. RIE of Si can be performed with various gases, including Cl_2 or fluorine compounds like SF_6, CHF_3 or XeF_2. The latter is well known for yielding a smooth, isotropic etch of Si, and is widely used for micro-fabrication of microelectromechanical systems (MEMS) [76]. Using Cl_2 also yields a very smooth Si etch, with a high degree of anisotropy and selectivity with respect to SiO_2 [77, 78]. In this paragraph, we present a Si RIE recipe based on SF_6 and CHF_3 gases that combines high anisotropy with a ~1:3 etch selectivity with respect to SiO_2. First, a standard RIE recipe [79] was used to investigate the dependence on plasma pressure and forward power. This recipe uses CHF_3 (17 sccm), SF_6 (20 sccm) and O_2 (14 sccm). The plasma pressure was varied between 20 and 100 mTorr; the forward power was varied between 150 and 350 W. All samples were etched for 45 sec in an Oxford Plasmalab 80+ plasma etcher.

Figure 2.2 shows SEM images of Si nanopillars etched with the recipe above, using a plasma pressure of 20 mTorr (a, b, c), 60 mTorr (d, e, f) and 100 mTorr (g, h, i) and a forward power of 150 W (a, d, g), 250 W (b, e, h) and 350 W (c, f, i). The initial SiO_2 layer thickness was 100 nm. In each SEM image, the SiO_2 layer on top of the Si nanopillars was imaged as well, to allow estimation of the etch selectivity. The first trend that can be noticed in Fig. 2.2 is that the highest SiO_2/Si selectivity is achieved at the lowest plasma pressure (panels a, b, c). The etch rate is slowest for the lowest pressure. At low forward power, a minor reduction in the SiO_2 mask thickness is observed for increasing plasma pressure. In order to compare the anisotropic properties of the RIE, we define an anisotropy factor as: A = 1 - D/H, where D is the absolute value of the difference between upper and lower diameter of the nanopillar and H is the height. Comparing Fig. 2.2(c) with Fig. 2.2(i) shows that, for a fixed forward power of 350 W, a plasma pressure of 20 mTorr etches ~50 nm of Si, with A = 0.9; a plasma pressure of 100 mTorr etches ~300 nm of Si with A = 0.5. The lower anisotropy factor for the plasma with higher pressure can be explained by the larger amount of inter-ion collisions in the plasma [80].

Second, we analyze the effect of the plasma forward power. Figure 2.2 shows that increasing the forward power increases the etch rate. For example, at a plasma pressure of 20 mTorr, a plasma etch with forward power of 150 W etches 30 nm of Si (Fig. 2.2(a)); a forward power of 350 W leads to an etch depth of 70 nm (Fig. 2.2(c)). This is explained by the higher energy of the ions that interact with the Si sur-

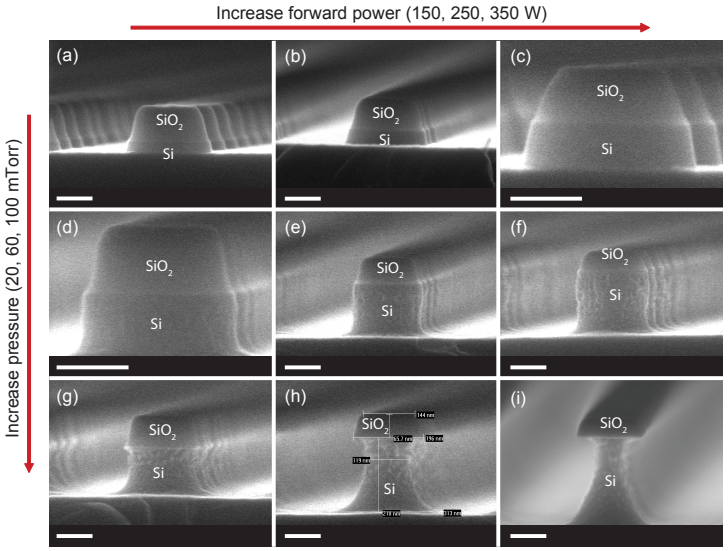

Figure 2.2: Si nanopillars etched into a Si(100) wafer patterned with SiO_2 nanocylinders using SCIL. The RIE is performed using CHF_3 (17 sccm), SF_6 (20 sccm) and O_2 (14 sccm), at a plasma pressure of 20 mTorr **(a, b, c)**, 60 mTorr **(d, e, f)** or 100 mTorr **(g, h, i)** and a forward power of 150 W **(a, d, g)**, 250 W **(b, e, h)** and 350 W **(c, f, i)**. The scale bar in all panels represents 100 nm.

face [81]. However, the SiO_2 mask thickness is reduced from ~95 nm (Fig. 2.2(a)) to ~75 nm (Fig. 2.2(c)). The selectivity for a 150 and 350 W forward power is thus ~1:6 and ~1:3, respectively. From the analysis above, we conclude that low pressure and low forward power are desirable to obtain an anisotropic and selective etch.

Next, we study the effect of the SF_6 and O_2 gas concentration. A fixed CHF_3 flow rate of 25 sccm was used for this etch test. It has been shown that the presence of CHF_3 in the plasma yields smoother etched surfaces [79]. On the other hand, higher CHF_3 concentrations reduce the etch selectivity with respect to the SiO_2 mask. We found that a CHF_3 flow rate of 25 sccm yields a smooth etched surface, while maintaining good selectivity. We use a fixed pressure of 7 mTorr and forward power of 150 W. All samples were etched for 4 min.

Figure 2.3 shows SEM images of Si nanopillars etched with the recipe described above, using an SF_6 flow rate of 15 (panels a, c) and 25 sccm (b, d), with no O_2 (a, b) and with an O_2 flow rate of 10 sccm (c, d). As can be seen, an increase in SF_6 concentration yields a deeper etch; comparing panels (a) and (c) with panels (b) and (d) shows that the Si nanopillar height increases from ~95 nm to ~175 nm. It can also be noted that for lower SF_6 concentration, the SiO_2 mask is completely consumed during the etch, whereas for higher SF_6 concentration, a 10-nm-thick SiO_2 layer is still present on top of the nanoparticles (see inset of Fig. 2.3(d)). This is explained by the fact that at low SF_6 concentration, the contribution of CHF_3 in the

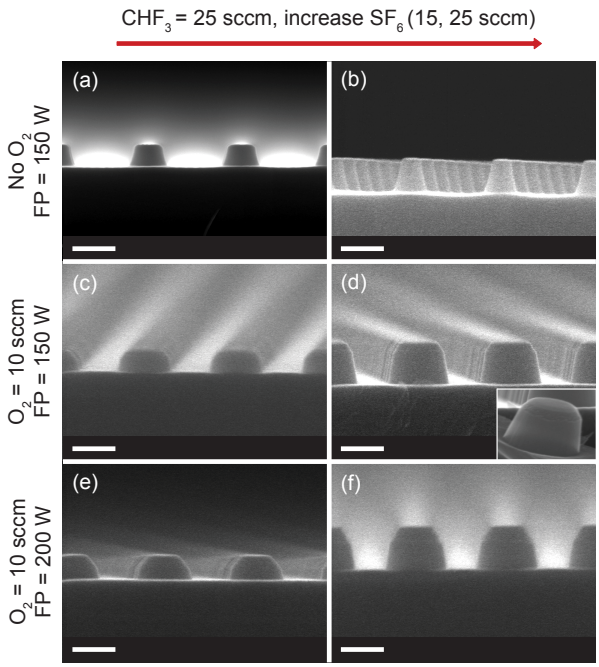

Figure 2.3: Si nanopillars etched into a Si(100) wafer with the RIE, using a CHF_3 flow rate of 25 sccm, an SF_6 flow rate of 15 **(a, c)** and 25 sccm **(b, d)**, with no O_2 **(a, b)** and with an O_2 flow rate of 10 sccm **(c, d)**. A plasma pressure of 7 mTorr and forward power of 150 W were used and the etch time was 4 min. The scale bar in all panels represents 200 nm. The inset in **(d)** is a high-resolution SEM image of a single nanopillar, showing the residual SiO_2 mask on the top part.

etch process is dominant, yielding a faster etch of SiO_2 with respect to Si. The faster etch of the SiO_2 mask for lower SF_6 concentration explains why the nanoparticle height is smaller.

Finally, we analyze the effect of O_2 on the Si etch. Comparing Fig. 2.3(a,b) with Fig. 2.3(c,d) shows that the presence of O_2 in the plasma yields nanoparticles with larger diameter. In particular, when no O_2 is present, the Si nanoparticles are significantly smaller than the mask size (250 nm). In contrast, for an O_2 flow rate of 10 sccm, the nanopillar size is close to the mask size. This can be explained by the fact the presence of O_2 in the plasma creates a passivation layer on the vertical etched Si surfaces which prevents the plasma from etching along the horizontal directions [82]. Overall, the recipe used for Fig. 2.3(d) gives the best anisotropy, selectivity and smoothness to fabricate cylindrical Si pillars on a Si(100) wafer. The recipe is summarized in the table below.

The recipe in table 2.1 was used to etch 250 nm wide, 150 nm high Si nanocylinder arrays on (100) Si wafers, in order to study the antireflection and light trapping

Parameter	Value
CHF_3 flow	25 sccm
SF_6 flow	25 sccm
O_2 flow	10 sccm
Forward Power	150 W
Pressure	7 mTorr
Resulting etch rate	45 nm/s

Table 2.1: RIE parameters used for fabricating Si nanocylinders on (100) Si wafers.

properties (see Chapters 6 and 8). Figure 2.4 shows an SEM image of the etched structure after the removal of the SiO_2 mask in diluted HF.

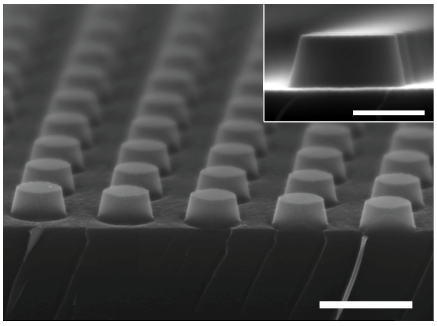

Figure 2.4: SEM image of a Si nanopillar array etched with RIE, using the recipe reported in table 1. The scale bar is 500 nm. Inset: single Si nanopillar, showing the slightly tapered shape. Scale bar is 200 nm.

The Si nanoparticle surface appears smooth, with roughness below 5 nm. The particle shape is a slightly tapered cylinder (see inset), with upper diameter of ~240 nm and lower diameter of ~270 nm. The particle height is 150 nm. From numerical simulations, it was found that the deviation of the actual shape from an optimal cylindrical shape does not significantly change the optical properties of the nanoparticles that will be reported further on in this thesis.

2.4 Conclusion

We have used substrate-conformal imprint lithography to fabricate large-area arrays of Si and TiO_2 nanopillars on Si substrates. The TiO_2 nanopillars are obtained by means of evaporating TiO_2 in a nanoimprinted resist hole pattern, followed by lift-off of the resist. The Si nanopillars are obtained by transferring a nanoimprinted pattern of pillars into a Si wafer, by means of RIE etching. A RIE recipe using CHF_3,

SF_6 and O_2 gases was optimized to yield a smooth, anisotropic Si etch, with a ~1:3 selectivity with respect to SiO_2. The effect of gas concentrations and plasma pressure and forward power on the Si etch were systematically studied.

3

Controlling Fano lineshapes in plasmonic light coupling into a substrate

We study the effect of particle shape and substrate refractive index on the plasmonic resonances of silver nanoparticles and we systematically relate this to the efficiency of light scattering into a substrate. The light coupling spectra are dominated by Fano resonances for the corresponding dipolar and quadrupolar scattering modes. Varying the particle shape from spherical to cylindrical leads to large shifts in the Fano resonance for the dipolar mode, reducing the light incoupling integrated over the AM1.5 spectral range. Using a dielectric spacer layer, good light coupling is achieved for cylinders in the near-infrared. An asymmetric environment around the particles turns quadrupolar resonances into efficient radiators as well.

3.1 Introduction

Metal nanoparticles have attracted much interest for their optical properties, which are very different from those of bulk material. The strong surface plasmon resonance (SPR) of these particles results in strong optical scattering and a strongly enhanced optical near-field around the particle [48, 83]. Recently, the scattering properties of metal nanoparticles are being investigated as a possible way to achieve light trapping in thin-film solar cells [40]. It has been shown experimentally [49, 50, 54, 84, 85] and numerically [51, 86] that arrays of metal nanoparticles placed on

the surface of a substrate can enhance the transmission of light into the substrate. From a fundamental point of view, it has been shown that Fano resonances play an important role in light incoupling into a substrate, reducing light transmission for frequencies below resonance due to destructive interference between scattered and incident light [87, 88]. Thus, good control of the scattering properties is needed in order to maximize the incoupling of light into a substrate for different wavelengths. Recent studies have investigated light scattering from metal nanoparticles of different material, size, shape and placed in different dielectric environment. We have shown earlier that cylindrical and hemispherical particles have a better near-field coupling to the substrate than spherical particles, due to the reduced spacing between the effective dipole moment and the substrate [51]. In another paper, Hägglund *et al.* propose that small spherical particles, rather than cylinders, are closer to the ideal shape for efficient light scattering into a substrate, due to the better coupling of the dipolar-like resonance of a sphere with respect to the quadrupolar-like resonance of a cylinder [89]. In this Chapter we clarify to what extent the near-field distribution of the particle modifies its scattering properties and thus the light incoupling into the substrate. By using Finite Difference Time Domain (FDTD) simulations, we analyze how the scattering efficiency spectrum is modified when the particle shape is gradually changed from a sphere to a cylinder and when the refractive index of the substrate is gradually increased. We systematically compare the scattering cross section spectrum with the total transmission spectrum, showing that an increase in transmission occurs at wavelengths above each scattering resonance, while a reduction occurs below resonance. In the last part of the Chapter, we use these results for photovoltaic applications. Cylindrical particles are found to be less efficient for light incoupling in the visible and near infra-red than spheres, due to a strongly red-shifted dipolar resonance. The introduction of a transparent dielectric spacer layer can re-establish efficient light transmission in the near infrared even for cylinders by blue-shifting the dipole resonance, an aspect that is relevant for experimental fabrication procedures.

3.2 Shape and environment effect on plasmonic resonance

We start our analysis by calculating the scattering cross section of silver nanoparticles on crystalline silicon, by means of FDTD calculations [90]. The simulation setup is shown in the inset of Fig. 3.1. A single silver nanoparticle is placed on the top of a semi-infinite silicon substrate. Perfectly Matched Layers (PMLs) are used at the boundaries of the simulation volume to prevent non-physical scattering at the boundaries. The simulation box size is 1×1×0.8 μm^3. A mesh size of 1 nm is used in the entire region containing the particle and at the substrate-air interface, and a smaller (0.2 nm) mesh grid is used around the sharp features at the particle-substrate contact point. We use a "Total-Field Scattered-Field" (TFSF) source [91] to simulate a broadband (wavelength 300-1100 nm) plane wave pulse incident on

the particle from the top. Usually, the scattering cross section is calculated in FDTD by placing frequency-domain monitors in the "scattered-field" region of a TFSF source. In this case, the presence of an absorbing substrate implies that part of the field does not reach the "scattered-field" region, due to absorption in the substrate. For this reason, we use a time-domain field monitor positioned 1 nm below the Si surface and we calculate the spectrum of the power scattered in the Si with a Fourier transform of the field measured by this time-domain monitor, after subtracting the incident field. The total power transmitted into the substrate, which will be analyzed in the next section, is directly measured by a frequency-domain monitor placed 1 nm below the Si surface. Optical constants for Ag were taken from Palik [92] and fitted using a Drude-Lorentz model; data for Si were taken from Palik as well.

The Ag particle is defined by a cylindrical body and two spheroids, one on top and one at the bottom, whose horizontal radius matches the radius of the cylinder (see inset in Fig. 3.1(a)). The shape of the particle is changed by varying the round edge parameter h, i.e. the vertical radius of the spheroids. The volume and the in-plane diameter of the particle are kept constant when varying the shape (thus the particle height changes) to ensure the same scattering volume. Figure 3.1(a) shows the scattering cross section spectrum, normalized to the geometrical cross section, for three different particle shapes: a sphere (green), a cylinder with a 10 nm round edge (red) and a cylinder with sharp edge (h = 0 nm, blue). We observe that all spectra present two resonances. The quadrupole resonance around 450 nm wavelength does not shift when varying the particle shape. On the contrary, the dipole resonance is strongly red-shifted when the shape is changed from a sphere (resonance at 500 nm) to a 10 nm round edge particle (800 nm) to a cylindrical particle (resonance out of range of the graph, above 1100 nm). Note that the small oscillations in the scattering cross section spectra are the result of hot-spots in the contact region of the particle with the substrate, due to the finite size of the mesh grid in the simulation setup.

In order to understand the origin of the different resonances that appear in the spectra for the three different shapes, we study the scattering cross section starting from the very simple, but instructive case of a single silver nanoparticle in homogenous medium. For spherical particles, Maxwell's equations can be solved exactly, and the scattering cross section can be calculated using Mie theory [48, 83]. For particles of different shape, FDTD calculations were performed. Figure 3.2 shows the normalized scattering cross section (indicated by the gray scale) as a function of wavelength and (a) particle size, (b) surrounding refractive indices, and (c) particle shape. The latter is once again defined by the round edge parameter shown in the inset of Fig. 3.1(a). The trends seen in Fig. 3.2 (a) and (b) are all well known [47, 48]: as the particle size (Fig. 3.2(a)) or the refractive index of the surrounding medium (Fig. 3.2(b)) increases higher-order multipolar modes appear (dipole, quadrupole, octupole, etc.), and all resonances red shift and broaden, due to increased retardation across the particle. Varying paricle shape (Fig. 3.2(c)) we notice a small red-shift of the dipolar and quadrupolar resonance, when the par-

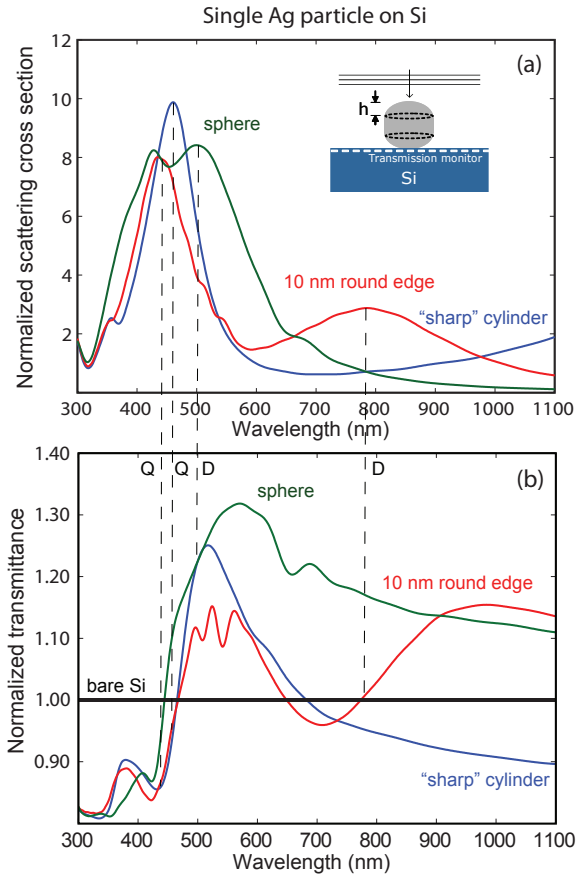

Figure 3.1: Normalized scattering cross section spectra **(a)** and normalized transmittance **(b)** for particles of three different shapes on top of a crystalline Si substrate. The dipole resonance is strongly red-shifted when particle shape is changed from a sphere (green), to a 10 nm round edge cylinder (red), to a sharp edge cylinder (blue). The normalized transmittance spectrum shows a reduction below each resonance, due to the Fano effect. The inset in **(a)** shows the simulation geometry. Data are calculated for a box size of 1×1×0.8 μm^3. The peak resonance wavelengths are indicated by the dashed vertical lines.

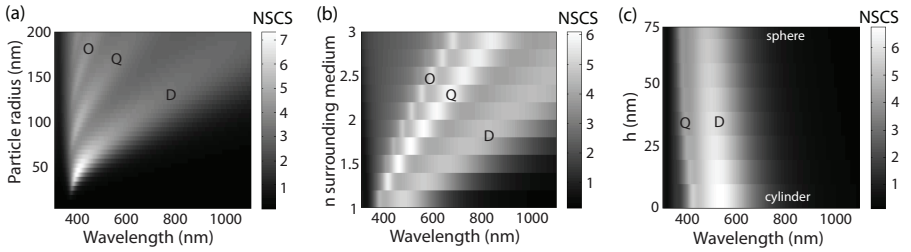

Figure 3.2: Normalized scattering cross section (NSCS) spectra (gray scale) for a Ag sphere in air as a function of particle size **(a)**, for a 150 nm diameter Ag sphere as a function of different surrounding refractive index **(b)**, and for a nanoparticle in air as a function of the round edge parameter h **(c)**. Panels **(a)** and **(b)** are calculated using Mie theory; panel **(c)** is the result of FDTD calculations. A redshift of the resonances is observed as the particle size or the surrounding refractive index increase and when the shape is changed from a sphere to a cylinder. Dipolar (D), quadrupolar (Q) and octupolar (O) resonances are indicated.

ticle shape is changed from a sphere (75 nm round edge, top of the graph) to a cylinder (0 nm round edge, bottom of the graph), which we attribute to slightly enhanced retardation across the particle.

The next step is to analyze how the scattering cross section of particles of different shapes changes when a substrate is introduced. Mie theory can no longer be used, due to the breaking of the symmetry in the surrounding environment. Thus, we use FDTD simulations to calculate the scattering efficiency. Figure 3.3 shows the normalized scattering cross section (gray scale) for a sphere (a), a 10 nm round edge cylinder (b) and a sharp edge cylinder (c), as a function of wavelength and substrate index. The three particle shapes clearly show different trends. In

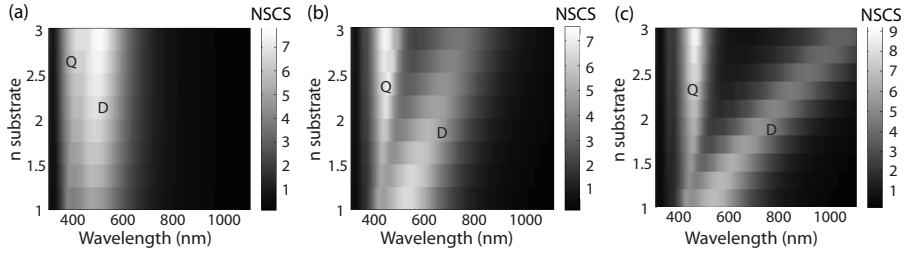

Figure 3.3: Normalized scattering cross section spectra (NSCS, gray scale) for a sphere **(a)**, a 10 nm round edge cylinder **(b)** and for a sharp cylinder **(c)**, all with an in-plane diameter of 150 nm, as a function of the substrate refractive index. A redshift of the dipolar resonance is observed as the substrate index increases. This effect is very large for cylindrical particles. The quadrupolar resonance is only slightly affected by the presence of the substrate.

the case of a spherical particle (Fig. 3.3(a)), both the dipolar and the quadrupolar resonance are nearly unaffected by the presence of the substrate. On the other

hand, for a 10 nm round edge cylinder (Fig. 3.3(b)) the graph shows a strong redshift for the dipolar resonance, whereas the quadrupole resonance is nearly unchanged. Finally, for a sharp cylinder (Fig. 3.3(c)), the redshift of the dipolar resonance is even larger; the quadrupolar peak is again nearly unaffected.

In order to understand the origin of the large red-shift of the dipolar resonance of the cylindrical particle on a substrate, we investigate the field distribution inside the cylinder at the resonance wavelengths. Figure 3.4 shows the scattered field distribution at dipole (a) and quadrupole (b) resonance in air, and at dipole (c) and quadrupole (d) resonance on a n=3 substrate. The scattered field is obtained subtracting the incident field from the total field. As can be seen, the presence of a

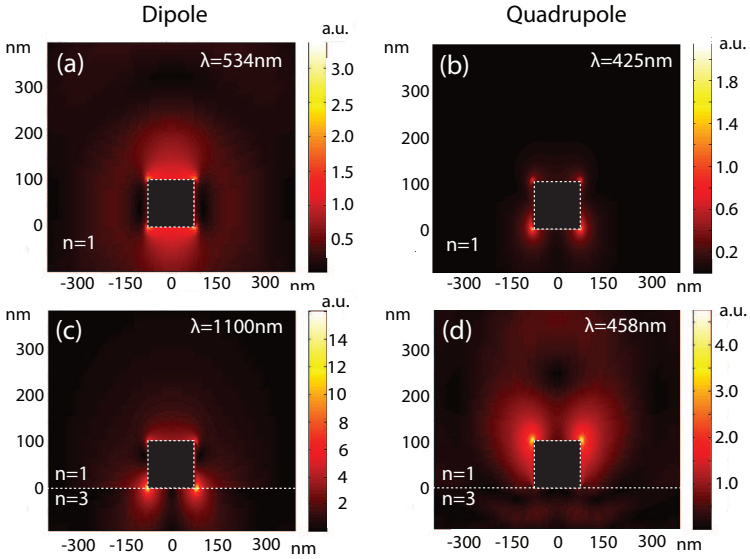

Figure 3.4: Scattered electric field intensity distribution for the dipolar **(a)** and quadrupolar **(b)** resonance in air and for the dipolar **(c)** and quadrupolar **(d)** resonance for a 150 nm diameter cylinder on a n=3 substrate. The presence of the substrate strongly modifies the field distribution of the particle at resonance. The field distribution due to the dipolar resonance is located at the interface with the substrate, whereas the quadrupolar resonance field is located at the particle-air interface.

high-index substrate changes the field distribution of particle at resonance. For the dipole resonance, the symmetric field distribution of a particle in air (a) is turned in a dipolar-like field distribution at the interface with the substrate (c). On the contrary, for the quadrupole resonance, the symmetric field plot in air (a) turns into a dipolar-like distribution at the particle-air interface (d). This result is in agreement with the observation of Hägglund *et al.* [89]. For this reason, the dipolar resonance residing at the particle-substrate interface, is more sensitive to the changes in the local environment when the substrate index is increased, thus resulting in the pro-

nounced red shift shown in Fig. 3.3(c). The quadrupolar resonance, on the other hand, is less sensitive to the change of substrate index, as the corresponding field is located at the particle-air side. Thus, its resonance wavelength is only slightly changed when the substrate index is increased.

3.3 Effect on light incoupling into a substrate

The results obtained above on the scattering cross section spectra for different shapes and substrate index are closely related to the efficiency of light incoupling into a substrate by metal nanoparticles. We study the light incoupling into a silicon substrate by means of FDTD calculations. The simulation setup is shown in the inset of Fig. 3.1(a): a frequency-domain monitor positioned just below the surface measures the total power that is coupled into the Si (transmission).

Figure 3.1(b) shows the transmission spectrum of a single Ag nanoparticle on top of Si, normalized to the transmission spectrum of a bare Si substrate. Note that the absolute values of the normalized transmittance depend on the simulation box size, which is 1×1×0.8 μm^3 in this case. The small features present in these spectra are again attributed to the finite mesh size of the simulation setup. The dashed lines between Figs. 3.1(a) and 3.1(b) correspond to the dipole and quadrupole resonance peak wavelengths. The graph shows that in spectral ranges above resonance the transmission is enhanced by the presence of the nanoparticle. The mechanism behind this effect is the preferential scattering of light at the particle resonance into the high-index substrate, due to the higher density of states in the substrate [93]. This enhancement is seen for both the dipolar and quadrupolar mode for the sphere and rounded cylinder in Fig. 3.1(b); for the sharp cylinder the dipole resonance is outside the range of the graph. In contrast, a clear reduction of the incoupled power occurs below each resonance. This reduction occurs due to a Fano effect, i.e. a destructive interference between scattered and incident light occurring at wavelengths below resonance [87]. The shift of the plasmon resonance to the red occurring when the shape is changed from a sphere to a cylinder, leads to a broadening of the Fano reduction for wavelengths below resonance. For a sharp cylinder, with the dipolar resonance above 1100 nm, the reduction in transmission becomes very broadband (see Fig. 3.1(b)).

3.4 Example: plasmon-enhanced light coupling into c-Si solar cells

Clearly, the use of metal nanoparticles to increase transmission into the substrate requires a careful choice of particle shape, depending on the wavelength of interest, in order to tune the effect of these Fano resonances on the incoupling. From now on, we focus on the metal nanoparticles of these arrays for photovoltaic applications.

Figure 3.5 shows the wavelength integrated transmission calculated for different values of the round edge parameter, ranging from 0 nm (sharp cylinder) to 75 nm (sphere), normalized to transmission for bare Si, by integrating over the AM1.5 solar spectrum from 300 to 1100 nm. The enhancement factor is thus an index of how good the incoupling of sunlight into the Si solar cell is. The graph clearly shows

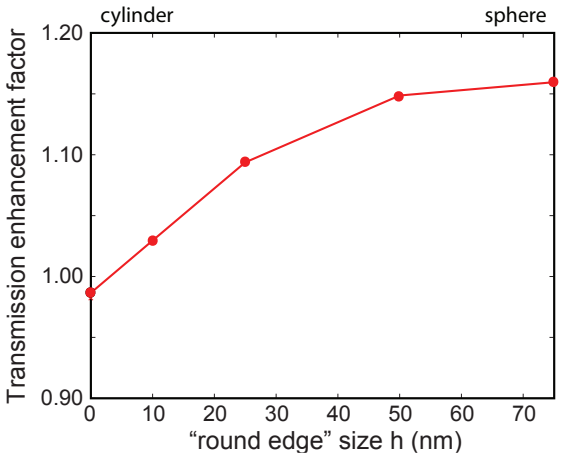

Figure 3.5: Transmission enhancement factor, calculated by integrating transmission spectra such as in Fig. 3.1(b) over the AM1.5 solar spectrum, normalized to a bare Si substrate, as a function of the round edge parameter. Spherical particles (75 nm round edge) show better incoupling of light than cylindrical particles (0 nm round edge). The simulation box size is 1×1×0.8 μm^3.

an increase in the enhancement factor as the shape is varied from a cylinder to a sphere. The lower value for a sharp edge cylinder is explained by the broadband Fano reduction below the dipolar resonance in the infrared region (Fig. 3.1(b)). As the particle is made rounder and rounder, the dipolar resonance is shifted towards the blue, and the Fano reduction becomes less significant. Thus, the transmission enhancement factor increases.

The data presented in Fig. 3.5 show that for bare particles placed on a Si substrate a round shape is better than a cylindrical one. We now solve the controversy with literature regarding the optimal shape. Catchpole *et al.* showed that cylindrical shapes show better near-field coupling into the substrate than a sphere. Our work shows that this comes at the expense of a large red-shift of the Fano resonance, which when integrated over the solar spectrum is detrimental, leading to the spherical shape as the preferred one, in agreement with Hägglund's prediction.

It has already been shown that the introduction of a dielectric spacer layer between particles and substrate yields a blue-shift of the dipole resonance [94, 95]. However, the effect of this shift on the light coupling to a substrate taking into account the Fano interference has not been studied so far. Figure 3.6 shows the effect on the scattering cross sections and on the transmission spectra of introducing a

Si_3N_4 (n=2.00) dielectric spacer layer between a cylindrical Ag nanoparticle and the Si substrate. The upper panel (Fig. 3.6(a)) shows the scattering cross section

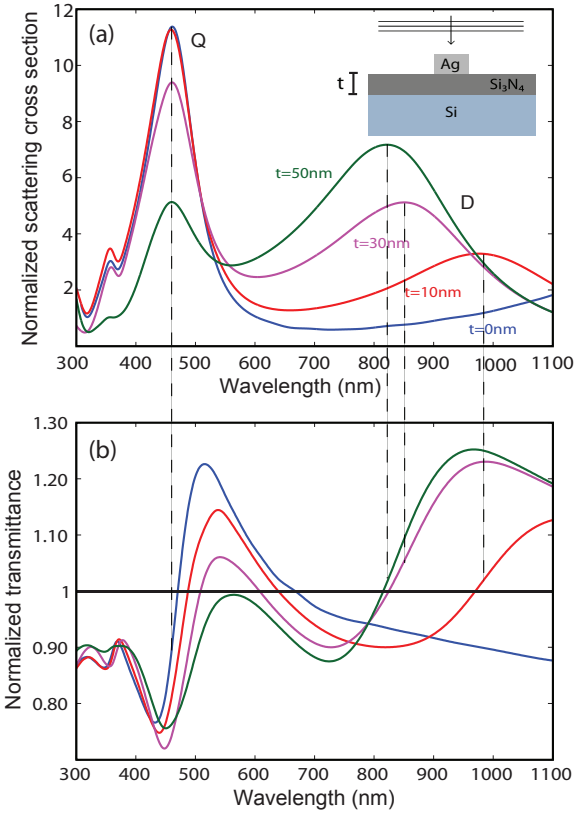

Figure 3.6: Normalized scattering cross section **(a)** and normalized transmittance **(b)** spectra for a cylindrical Ag particle on top of Si (blue) and on top of 10 nm (red), 30 nm (purple) and 50 nm (green) thick Si_3N_4 layer. Data in **(b)** are normalized to the transmission for a Si substrate with the corresponding Si_3N_4 layer thickness. The dipolar resonance is shifted to the blue as the Si_3N_4 layer thickness is increased. The normalized transmittance spectrum shows a reduction below each resonance, due to the Fano effect.

of a cylindrical (0 nm round edge) Ag nanoparticle directly on Si (blue), and on top of a 10 nm (red), 30 nm (purple) and 50 nm (green) thick Si_3N_4 spacer layer. The lower panel (Fig. 3.6(b)) shows the normalized transmission spectrum for the same geometries. Note that in this case the reference is different for each curve, as the transmission has been normalized to the case of a Si substrate with a Si_3N_4 layer on top, with the corresponding thickness. This normalization allows to isolate the effect due to the particle scattering only, corrected for the intrinsic anti-reflection effect due to the Si_3N_4 layer.

We observe a strong blue-shift of the dipolar resonance as the Si_3N_4 thickness is increased from 0 to 50 nm. This phenomenon is explained by the reduction of the effective index in the near-field region of the particle, which results in a shift of the resonance to lower wavelengths, as shown before (see Fig. 3.3(c)). As a consequence, an increase of the total transmission is observed in the near infrared due to the narrowing of the range where the Fano related reduction is present. This work also shows that creating a strong field asymmetry around the particle due to the presence of a high-index substrate can turn a quadrupole mode into an efficiently radiating mode. Interestingly, Fig. 3.6 also shows a strong reduction in the strength of the quadrupole resonance as the Si_3N_4 thickness is increased. This is due to the fact that for Ag particles that are strongly coupled to the Si substrate the quadrupole field distribution becomes more dipolar in nature (see Fig. 3.4) resulting in more effective radiation into the substrate. Thus, a thicker Si_3N_4 spacer layer causes enhanced transmission (compared to the bare Si_3N_4 case) in the infrared but reduced transmission in the visible.

3.5 Conclusion

We have systematically studied the effect of Ag particle shape and substrate on the plasmon mediated light coupling to a high-index substrate.The dipole resonance is strongly redshifted when the shape is changed from a sphere to a cylinder due to the increased near-field coupling of the dipolar field with the substrate. The Ag particles scatter preferentially into the substrate. We determine the transmission spectra for different shapes and compare these to the scattering spectra. Strong Fano-type lineshapes are observed in the transmission spectra, originating from the interference of the direct and scattered light fields. Destructive interference leads to reduced transmission below resonance and is then very sensitive to particle shape. The strong red-shift observed for cylindrical particles reduces the incoupling for a spectral band corresponding to the AM1.5 solar spectrum due to the Fano effect. The introduction of a dielectric spacer layer results in good light incoupling for the near-infrared also for cylindrical particles, by shifting the dipolar resonance to the blue. In a strongly asymmetric dielectric environment the quadrupole mode is an efficient radiator as well. The insights given in this Chapter clarify the role of near-field coupling and Fano resonances in the scattering of light and transmission of light into a substrate. These results open new perspectives for designing and fabricating metal nanoparticle arrays for light trapping in thin-film solar cells.

4

Light coupling into silicon substrates using coupled plasmonic nanoparticle arrays

We perform a systematic numerical and experimental study of the light incoupling into a Si substrate by arrays of Ag nanoparticles in order to achieve the best impedance matching between light propagating in air and in the substrate. We identify the parameters that determine the incoupling efficiency, including the effect of Fano resonances in the scattering, inter-particle coupling, as well as resonance shifts due to variations in the near-field coupling to the substrate and spacer layer. The optimal configuration studied is a square array of 200 nm wide, 125 nm high spheroidal Ag particles, at a pitch of 450 nm on a 50 nm thick Si_3N_4 spacer layer on a Si substrate. When integrated over the AM1.5 solar spectral range from 300 to 1100 nm, this particle array shows 50% enhanced incoupling compared to a bare Si wafer, 8% higher than a standard interference antireflection coating. Experimental data show that the enhancement occurs mostly in the spectral range near the Si band-gap. This study opens new perspectives for antireflection coatings and light management in Si solar cells.

4.1 Introduction

The coupling of light into a dielectric material is always associated with (usually unwanted) reflection. Reflection can be reduced by using a dielectric interference

coating. These coatings are optimized for a given wavelength and incident angle and thus reduce reflectance over a relatively narrow bandwidth. Recently, metal nanoparticles deposited onto a substrate have been studied to increase the coupling of light into a substrate [40, 86]. These particles interact strongly with the incident light and preferentially scatter light into the high-index substrate, leading to enhanced transmittance and thus reduced reflectance. The resonant scattering is due to plasmon resonances in the metallic particles, and leads to reduced reflection over a broad spectral range.

So far, most experimental work on anti-reflection (AR) effects from particle scattering has focused on ensembles of metal nanoparticles made using self-assembly, which leads to random nanoparticle configurations, with limited control over the particle geometry [49, 50, 54, 55, 84, 96, 97]. As a result, the effect of particle geometry has not been systematically studied experimentally. Theoretical work, using finite-difference time domain (FDTD) simulations, has focused mostly on the scattering from single particles, thereby neglecting inter-particle coupling [51, 52, 94]. Thus, so far no systematic studies have been made of the critical parameters that determine the optimum impedance matching of light using metal nanoparticle arrays. Moreover, no previous work has made a systematic comparison between particle arrays and standard dielectric AR coatings.

In this Chapter, we perform a systematic study of the coupling of light into a crystalline silicon substrate, through scattering of light from silver nanoparticle array geometries. We investigate the effect of particle shape, size and array pitch on the incoupling, using both experiment and simulation. Furthermore, we study the effect of a dielectric spacer layer between the particle array and the substrate. We find that an optimized array of Ag nanoparticles, combined with a Si_3N_4 spacer layer of suitable thickness, yields better light incoupling into a silicon substrate over a broad spectral range than a traditional Si_3N_4 interference AR coating.

We identify the parameters that determine the incoupling efficiency, including the effect of Fano resonances in the scattering, inter-particle coupling, as well as resonance shifts due to variations in the near-field coupling to the substrate and the dielectric spacer layer. The insights given in this Chapter provide general guidelines for the optimization of impedance matching using plasmonic scattering, opening new perspectives for application of these coatings in photovoltaics [85, 98], photodetectors, and optical components in general. For the photovoltaic application, the use of metal nanoparticles as an AR coating provides additional benefits, such as an enhanced optical path length as a result of angular redistribution of light inside the semiconductor, and light trapping in thin-film solar cells by coupling to waveguide modes [64].

4.2 Light scattering from single particles: FDTD simulations

As a first step, we use three-dimensional FDTD simulations [90] to study the basic case of a single silver nanoparticle on top of a semi-infinite silicon substrate. The FDTD simulation geometry is shown schematically in the inset of Fig. 4.1. A broadband pulse (wavelength 300-1100 nm) is used to simulate a plane wave incident on the particle from the top. A monitor positioned at the surface measures the total power that is coupled into the Si substrate (transmittance). Perfectly Matched Layer (PML) boundary conditions were used in the incident direction to prevent non-physical scattering at the boundaries, thereby effectively simulating an infinitely-thick Si layer. PMLs are also used at the boundaries of the simulation volume, to simulate a single-particle configuration. Optical constants for Ag were taken from Palik [92] and fitted using a Drude-Lorentz model; data for Si were taken from Palik as well. Figure 4.1 shows the transmission spectrum of three differ-

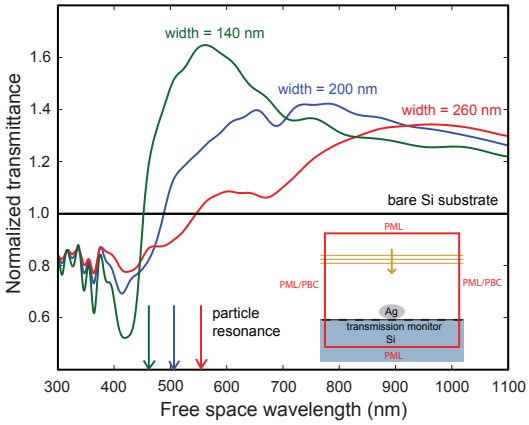

Figure 4.1: Transmittance spectrum for three different single Ag spheroids with 175 nm height and 140 nm (green), 200 nm (blue) and 260 nm (red) width, on top of a Si substrate, calculated using FDTD. Data are normalized to the transmittance for a bare Si substrate. For each particle, the transmission is enhanced for wavelengths above the Ag particle plasmon resonance, and suppressed for wavelengths below (Fano effect). The inset shows a schematic of the simulation geometry.

ent single Ag spheroids on top of a Si substrate, normalized to the transmission spectrum of a bare Si substrate. Particle height is 175 nm and particle widths are respectively 140 nm (green), 200 nm (blue) and 260 nm (red). The arrows in the graph indicate the plasmon resonance wavelengths for each of the particle derived from the peak in the simulated scattering spectrum. Note that the values of the normalized transmittance depend on the size of the simulation box (1×1 μm); the data in Fig. 4.1 therefore only serve to study the spectral trends in the transmission. Absolute values will be addressed in the next section when studying particle arrays.

For wavelengths above resonance, the transmission is enhanced by the presence of the nanoparticle. The mechanism behind this effect is the scattering of light by the dipolar resonance of the particle, which redirects the light preferentially into the high-index substrate [51, 99]. On the other hand, a reduced transmission is consistently observed below the particle resonance for each of the three particle sizes. This reduction occurs due to a Fano effect, i.e. the destructive interference between scattered and unscattered light that occurs below resonance [87, 88, 100, 101]. Figure 4.1 therefore shows that proper tuning of the plasmonic resonance wavelength is important in order to optimize the light coupling into the substrate [51, 52, 94]

4.3 Light scattering from particle arrays: FDTD simulation

Next, we study the case of a square array of Ag nanoparticles on top of a Si substrate. The FDTD geometry is identical to the single-particle case (inset in Fig. 4.1), with the exception of the use of periodic boundary conditions (PBCs) in the lateral direction instead of PML boundary conditions. The array pitch is thus equal to the simulation box size.

We have simulated the transmission spectrum for different Ag spheroid array geometries on Si. For each configuration, we determine an incoupling enhancement factor by integrating the enhancement over the spectrum and weighting to the AM1.5 standard solar spectrum in the 300-1100 nm spectral range. Figure 4.2 shows the enhancement factor for geometries with varying particle width (a), particle height (b) and array pitch (c). On the right axis, the absolute transmittance is shown for reference. The enhancement factor is taken relative to that for a bare Si layer. The enhancement for a Si wafer coated with an 80 nm thick Si_3N_4 AR coating is also shown for reference.

All curves show a clear optimum for 200 nm wide, 175 nm high oblate spheroids in an array with 450 nm pitch. This optimal configuration results in a 35% higher transmission with respect to the bare Si case, corresponding to an overall transmittance of 77%. The Si_3N_4 AR coating yields a 41% enhancement (80% transmittance).

The presence of an optimum in particle width and height is the consequence of a trade-off between different effects. Small particles show strong absorption and small scattering, thus reducing the amount of light transmitted into the substrate. On the other hand, tall particles have a reduced near-field coupling to the substrate, and wide particles have a strongly red-shifted resonance, resulting in a reduced transmittance in the lower-wavelength range due to the Fano effect (see Fig. 4.1). An optimum in the array pitch is also expected, as a smaller pitch also results in an undesired red-shift of the plasmonic resonance, due to a stronger coupling between the particles, and a large pitch corresponds to a small surface coverage, reducing the overall light scattering. It is important to note that the overall transmission enhancement is most sensitive to array pitch (Fig. 4.2(c)). This

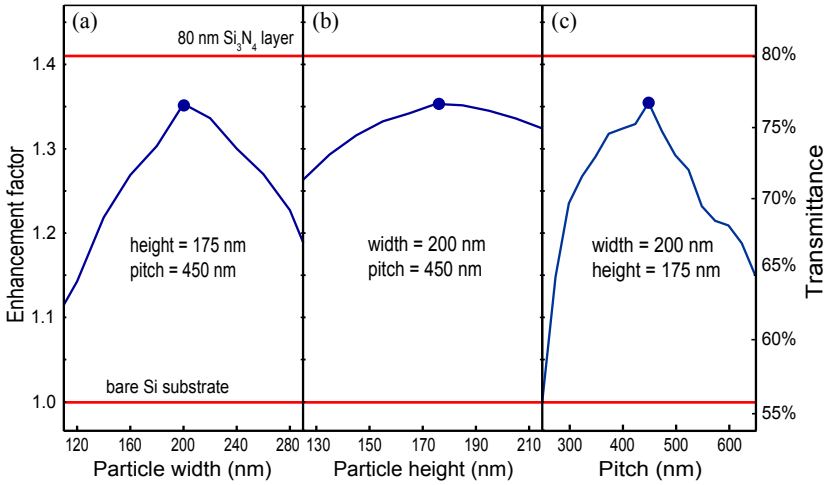

Figure 4.2: Transmission enhancement for Ag nanoparticle arrays on top of Si, for different geometries, varying particle width **(a)**, height **(b)** and array pitch **(c)**, integrated over the AM1.5 solar spectrum, relative to a bare Si substrate. The optimal configuration (solid dots) yields 35% better light incoupling with respect to bare Si and an overall integrated transmittance of 77%. The enhancement due to an 80 nm thick Si_3N_4 AR coating is also shown for reference.

implies that self-assembly techniques in which pitch is not well controlled are not suitable for the fabrication of these arrays.

Figure 4.3 shows the enhancement factor, defined as before, for 200 nm wide Ag spheroids with an array pitch of 450 nm, placed on a Si_3N_4 spacer layer over a Si substrate. Data are shown as a function of particle height with a 50 nm thick Si_3N_4 spacer layer (a), and for 125 nm high particles as a function of Si_3N_4 layer thickness (b). Particle width and array pitch were taken equal to the optimal values found in Fig. 4.2. The introduction of the spacer layer made it necessary to re-optimize the particle height, as the dielectric layer affects the near-field coupling to the substrate.

Figure 4.3(a) shows an optimal particle height of 125 nm, which is reduced compared to the optimum height without the spacer layer (Fig. 4.2, 175 nm). Figure 4.3(b) shows an optimal thickness of 50 nm for the Si_3N_4 spacer layer. For this configuration, a net incoupling enhancement of 49% with respect to the bare Si case is found, a value 8% higher than that for the standard 80 nm Si_3N_4 AR coating. The maximum value for the absolute transmittance is 84%.

The reduction of the optimal particle height is the result of an optimized near-field coupling between the particle and the Si substrate, since the distance between the particle and the substrate has been increased due to the introduction of a spacer layer. An optimum in Si_3N_4 thickness is found as thicker spacer layers lead to reduced near-field coupling, while thinner layers cause a redshift of the

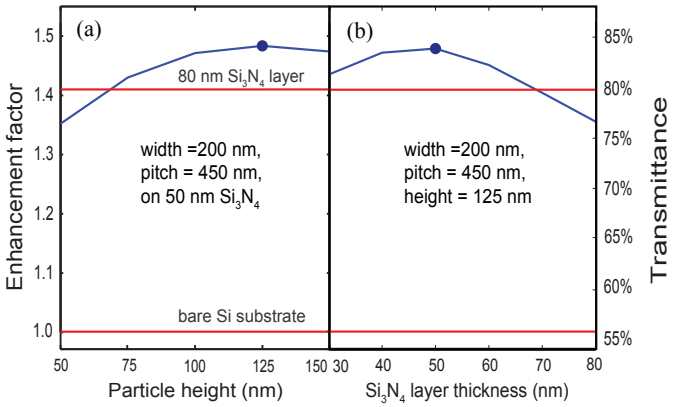

Figure 4.3: Transmission enhancement for Ag particle arrays on Si with a Si_3N_4 spacer layer, integrated over the AM1.5 solar spectrum, relative to a bare Si substrate. Data are shown for different particle heights with a 50 nm spacer layer **(a)** and for 125 nm high particles as a function of Si_3N_4 spacer layer thickness **(b)**. The best geometry increases the light incoupling by almost 50% with respect to bare Si, 8% higher than for a standard AR coating on Si.

plasmon resonance, as the near-field couples more strongly to the high-index Si substrate [95]. Moreover, the (thinner) Si_3N_4 layer serves as an AR coating in the blue spectral range.

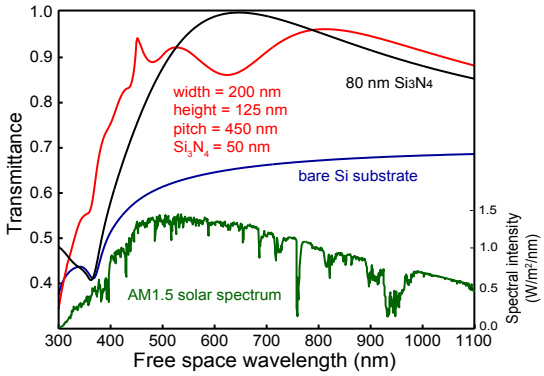

Figure 4.4: Spectra of transmission into Si for a bare Si substrate (blue), a Si substrate coated with 80 nm Si_3N_4 (black, standard AR coating) and the optimal configuration of Ag nanoparticles on a Si_3N_4 spacer layer (red). The presence of the particle array increases the light coupling in the near infrared, above 800 nm. The enhanced transmission in the blue is due to the reduced Si_3N_4 layer thickness compared to the 80 nm layer geometry. The AM1.5 solar spectrum is shown for reference.

Figure 4.4 shows the simulated transmittance spectra for a semi-infinite Si sub-

strate (blue), an 80 nm thick Si_3N_4 coated Si substrate (black) and for the optimal nanoparticle array on top of a 50 nm thick Si_3N_4 layer (red). The AM1.5 solar spectrum is also shown for reference (scale on the right axis). The optimized configuration shows a higher transmittance than the standard AR coating over almost the entire spectrum, with the exception of a narrow band around a wavelength of 600 nm. The transmittance enhancement in the blue can be explained by a blue-shift of the AR optimum for a 50 nm Si_3N_4 layer, compared to that of a 80 nm thick layer. The enhancement at longer wavelengths is a result of the strong metal particle scattering into the substrate (see also Fig. 4.1). The combination of the two effects results in a plasmonic AR coating that is optimized for a broad spectral range.

4.4 Light scattering from particle arrays: experiment

The enhanced coupling of light into a substrate due to the plasmonic coating was studied experimentally by means of reflectance spectroscopy. The samples were 300 μm thick p-type single-side polished monocrystalline Si wafers, with a phosphorous-diffused emitter, coated with a Si_3N_4 layer using plasma-enhanced chemical vapor deposition, on top of which Ag nanoparticle arrays were fabricated by means of electron beam lithography (EBL), silver evaporation and lift-off. A scanning electron microscopy (SEM) image of one of the arrays is shown in the inset in Fig. 4.5. The samples have a uniform Al back contact formed by screen printing. The image clearly shows the dense arrayed Ag particles, with a surface coverage of 20%.

In order to determine experimentally which geometry shows optimal light incoupling, we fabricated different Ag particle arrays in fields of 100 μm by 100 μm, each field with different particle width and array pitch, on samples with different Si_3N_4 thicknesses. The specular reflectance spectrum for each field was measured in an optical microscope, in the wavelength range 450-900 nm. For each field configuration, a reflection coefficient was calculated as the averaged specular reflectance spectrum, weighted by the AM1.5 solar spectrum in the 450-900 nm spectral range. Figure 4.5 shows the reflection coefficient for varying particle width (a), array pitch (b) and spacer layer thickness (c). The average reflection coefficient for a Si substrate coated with a 67 nm Si_3N_4 layer is also shown for reference (red line, 5.7%).

The trends shown in Fig. 4.5 for the specular reflectance closely match the optima in the simulation results shown in Fig. 4.2, indicated by arrows in Fig. 4.5. An optimal configuration is found for 180 nm wide particles (compared to a 200 nm optimal width from FDTD simulations), with a 450 nm array pitch (same as FDTD). The specular reflection coefficient is reduced from 5.7% to 1.4% by the presence of the particle array. The small deviations between the experimentally found optima and those from the FDTD results are attributed to the differences in particle shape (spheroidal in the simulation, cylinder-like in the experiment) and to the slightly different spectral ranges over which the averages are taken.

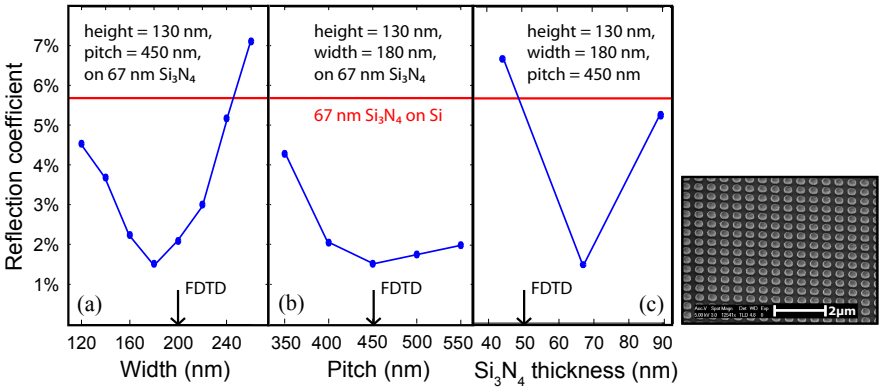

Figure 4.5: Measured specular reflection coefficient for different particle geometry on a Si substrate, with a Si_3N_4 spacer layer, averaged over the AM1.5 solar spectrum in the 450-900 nm spectral range. The particle width **(a)**, array pitch **(b)** and Si_3N_4 thickness **(c)** is varied. The data show a clear minimum, with a reflection coefficient of 1.4%. The red line indicates the reflection coefficient measured on a Si substrate with a 67 nm Si_3N_4 layer (5.7%), for reference. The arrows indicate the configuration for minimum reflectivity found in FDTD (Figs. 4.2 and 4.3). The inset on the right shows a SEM image of a silver nanoparticle array, fabricated by EBL.

In order to investigate the absorption in the Si layer, we have performed measurements of the total reflectivity in an integrating sphere setup. A 2×2 mm^2 array of silver nanoparticles, with the optimal parameters found in Fig. 4.5 was fabricated by using EBL on a sample with a 67 nm thick Si_3N_4 spacer layer. The angle-integrated reflectivity spectra were then measured in the 300-1200 nm spectral range, for an angle of incidence of 8°. Figure 4.6 shows the total reflectivity spectrum for this sample (blue), and for the same sample without Ag nanoparticles (red).

The reflection spectrum for a Si substrate coated with 67 nm of Si_3N_4 shows the typical trend for an interference AR coating, yielding a minimum in reflection around 600 nm. Adding the particle array yields a broadband reduction in total reflection above 850 nm, and, with the exception of the relatively small enhancement in the 600-800 nm range, does not drastically affect the light incoupling for lower wavelengths. Note that the sudden reflection increase above 1050 nm in both curves is due to light that is reflected from the back contact and that is not absorbed in the Si substrate. Indeed, the absorption length of Si at 1050 nm equals 600 μm, i.e. twice the cell thickness. The dashed lines in Fig. 4.6 are extrapolations of the data, representing the reflectivity of a semi-infinite substrate sample, made using a linear fit for the bare substrate (red), and a Lorentian fit for the substrate with particles (blue) on the data set in the 600-1000 nm spectral range.

The total reflection spectrum can be used to calculate the absorption in the solar cell, using the relation: A=1-R-T, where A is the absorbance, R the reflectance and

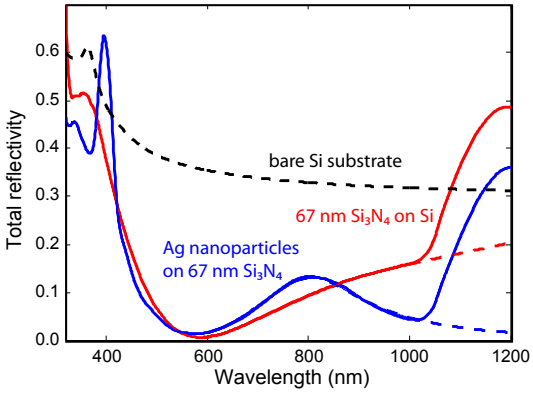

Figure 4.6: Measured total reflection spectrum from a 300 μm crystalline Si cell coated with 67 nm Si_3N_4 (red) and the same sample with an optimized Ag particle array on top (blue). The particles reduce the reflection for wavelengths above 800 nm, improving the incoupling of light into the Si substrate. The dashed lines are extrapolated data representing the reflection from a semi-infinite substrate. The calculated reflectance of a semi-infinite Si substrate is shown for reference (dashed black line).

T the transmittance. In this case, T is zero, since the sample has an Al back reflector. Figure 4.7 shows the calculated absorption spectrum for the sample with the metal nanoparticles on top (blue), normalized to the absorption in the reference sample (67 nm Si_3N_4 on Si, red line). The Si band-gap wavelength is also shown in the graph for reference (vertical dashed line).

Figure 4.7 shows a broadband absorption enhancement above 850 nm, with a peak larger than 120% near the Si band-gap wavelength, i.e. in the region where Si is a poor absorber of light. With the exception of a narrow dip around 400 nm, the spectrum below 850 nm is only slightly affected by the presence of the particle array.

Our experimental data clearly demonstrate that metal nanoparticle arrays result in strongly enhanced light coupling and thus enhanced impedance matching into a Si substrate. When compared to a standard AR coating, light coupling is enhanced over a broad spectral range in the near-infrared.

While the major effect observed in this Chapter is enhanced impedance matching into a Si substrate, a minor light trapping effect is also observed in the total reflectivity measurement in Fig. 4.7. A signature of the light trapping effect can be observed in the small change in the slope of the curve around 1050 nm (see arrow in Fig. 4.7). In the 1050-1200 nm spectral range, i.e. the range where light is not fully absorbed in the 300 μm thick Si substrate, the absorption enhancement in the Si substrate is due to both the AR effect analyzed in this Chapter and light trapping. Based on the data, it is possible to derive a rough estimate of the relative influence of the two different effects on the absorption enhancement. From the extrapolated

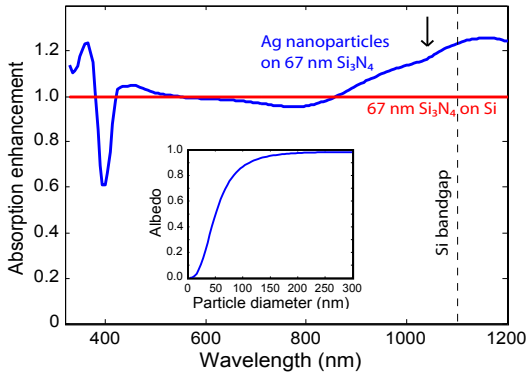

Figure 4.7: Absorption enhancement due to the presence of a silver nanoparticle array on top of a 67 nm Si_3N_4 layer on a Si substrate. A broadband enhancement is observed in the near-infrared, for wavelengths above 800 nm. The arrow indicates a small kink in the data that indicates the onset of light trapping. In the inset, the calculated albedo for a silver nanoparticle in air is shown as a function of particle diameter. For 180 nm diameter particles, as used in the experiment, the albedo amounts to 97%, meaning that only 3% of the light is absorbed in the metal.

data in Fig. 4.6 (dashed lines), we can estimate what part of the absorption is purely due to the enhanced AR effect, and compare it to the total absorption enhancement measured on the finite-thickness sample (Fig. 4.7). At 1120 nm (Si band-gap), we find that the enhancement due to the AR effect amounts to 20%, while the total measured enhancement is found to be 25%. From this we estimate that the remaining 5% of the absorption enhancement is a result of light trapping. The next step is to apply these results on much thinner Si wafers where the effect of light trapping will become apparent at a much broader spectral range and compare it with standard light trapping methods such as surface texturing.

Finally, we point out that the absorption spectrum shown in Fig. 4.7 includes both absorption in the Si substrate and Ohmic dissipation in the metal nanoparticles. The inset in Fig. 4.7 shows the calculated albedo of a silver nanoparticle in air as a function of particle diameter. For particles of 180 nm diameter, as used in the experiment, the albedo amounts to 97%, meaning that only 3% of the light is absorbed in the Ag nanoparticle. For particles on a higher index substrate, the albedo is even higher, as the scattering is enhanced due to the higher density of states in the substrate. It is therefore correct to neglect dissipation in the metal nanoparticles and attribute the absorption measured in Fig. 4.7 solely to the Si substrate.

4.5 Conclusion

We have performed a systematic study of light coupling into a Si substrate coated with an array of Ag nanoparticles that show a strong plasmon resonance. We have shown by means of FDTD simulations that a properly chosen array of Ag nanoparticles on a Si_3N_4 spacer layer acts as a better antireflection coating than a standard Si_3N_4 interference coating, over a broad spectral range. The coupling is determined by competing effects of Fano resonances in the scattering, inter-particle coupling, and resonance shifts due to variations in the near-field coupling to the substrate and spacer layer. We find that 200 nm wide, 125 nm high spheroidal Ag particles in a square array with 450 nm pitch on top of a 50 nm thick Si_3N_4 layer provide the best impedance matching for a spectral distribution corresponding to the AM1.5 solar spectrum. Using the optimal array configuration, simulations predict a 8% improvement of light incoupling to Si compared to the best standard interference AR coating, and an improvement of almost 50% with respect to a bare Si substrate. Our simulation results are confirmed experimentally by reflection and absorption spectroscopy on fabricated Ag nanoparticle arrays. For wavelengths near the Si bandgap, where light is poorly absorbed, a small light trapping effect is also observed. The results obtained in this work can be used to design antireflection and light trapping coatings for thin Si solar cells and may have applications for photodetectors and other optical components as well.

5

Prospects of near-field plasmonic absorption enhancement in semiconductor materials using embedded Ag nanoparticles

We use numerical simulations to calculate the near-field absorption enhancement of light due to Ag nanoparticles embedded in crystalline Si, amorphous Si, a polymer blend, and Fe_2O_3. We study single Ag particles in a $100 \times 100 \times 100$ nm semiconductor volume, as well as periodic arrays with 100 nm pitch. We find that in all cases Ohmic dissipation in the metal is a major absorption factor. In crystalline Si, while Ag nanoparticles cause a 5-fold enhancement of the absorbance in the weakly absorbing near-bandgap spectral range, Ohmic losses in the metal dominate the absorption. We conclude crystalline Si cannot be sensitized with Ag nanoparticles in a practical way. Similar results are found for Fe_2O_3. The absorbance in the polymer blend can be enhanced by up to 100% using Ag nanoparticles, at the expense of strong additional absorption by Ohmic losses. Amorphous Si cannot be sensitized with Ag nanoparticles due to the mismatch between the plasmon resonance and the bandgap of a-Si.

5.1 Introduction

Metal nanoparticles (NPs) present unique optical properties, which are very different from those of bulk material. The localized surface plasmon resonance (LSPR) of

these particles results in strong optical scattering and a strongly enhanced optical near-field around the particle [48, 83]. Recently, metal NPs have been investigated as a possible way to improve the performance of thin-film solar cells [40]. Three different configurations have been proposed to achieve this goal: (1) particles placed at the front-surface of a solar cell, (2) metallic nanostructures integrated with the back contact of the solar cell, and (3) metal nanoparticles embedded in the active layer of a solar cell [40]. The first geometry has been broadly studied both theoretically and experimentally, and it has been shown that enhanced transmission of light into a high-index substrate can be achieved due to the strong forward scattering of plasmonic NPs [49–53]. In addition, this geometry enhances light trapping in thin-film devices [54, 55]. The second configuration has also been studied in detail and showed strong absorption enhancement in thin-film solar cells due to coupling of scattered light to waveguide modes in the thin layer [63–65].

The third configuration with embedded NPs has also been studied extensively, but in contrast to the other geometries, with mixed success. Metal NPs embedded in a semiconductor material act as antennas for the incident light and store energy in the LSPR. This energy can be either absorbed in the semiconductor material due to the strong plasmonic near-field that evanescently extends into the semiconductor, absorbed in the metal NP by Ohmic dissipation, or scattered into the far field. For small NP (diameter below 30 nm) scattering is only a small effect, due to the low albedo [102]. Some experimental work has shown that photocurrent enhancement can be achieved in (ultra)thin-film organic solar cells [66–70] and dye-sensitized solar cells [71–73], due to the plasmonic near-field coupling of small metal NPs. Also, Au NPs embedded in Fe_2O_3 photoanodes enhance the efficiency of photoelectrochemical water splitting [103]. Theoretical modeling of plasmonic NPs embedded in a semiconductor layer has shown increased optical absorption in crystalline Si [89, 104], polymer blends [70] and copper phthalocyanine [105] substrates. Despite the fact that some absorption enhancement has been demonstrated in various semiconductor layers, there is no systematic study towards the limitations for such absorption enhancement as a result of the intrinsic Ohmic losses in the metal NPs [14, 106, 107].

In this Chapter we use numerical calculations to systematically compare the absorption in the semiconductor with the losses in the metal NP, for different NP geometries and semiconductor materials. We identify the role of key parameters such as particle size, material optical properties, and layer thickness, in determining the absorption enhancement in the semiconductor material. We show that the total average absorption in polymeric materials can be enhanced by up to 100%. However, in other semiconductors, such as silicon or iron oxide absorption in the metal strongly limits the maximum achievable absorption. Based on these insights, we define design guidelines for achieving optimal absorption enhancement due to plasmonic near-field coupling and show the limitations of this approach for most semiconductors. Note that only plasmonic near-field absorption enhancement by embedded metal nanoparticles is considered in this Chapter. Plasmon-mediated scattering mechanisms, which have already been shown to be beneficial for light

trapping in solar cells [51–55, 63–65, 102], are not investigated in this work.

5.2 Simulation results

We use Finite Difference Time Domain (FDTD) simulations [90] to study the near-field absorption of a single Ag NP embedded in a semiconductor material. The simulation setup is sketched in the inset of Fig. 5.1(b). The simulation volume is a cube with size of 100×100×100 nm, and is fully filled with semiconductor material. Perfectly Matched Layers (PMLs) boundary conditions are used on all boundaries for the single-particle simulations. The spherical Ag NP is placed at the center of the cube and has a diameter ranging from 5 to 60 nm. A mesh size of 1 nm is used over the entire volume, with a refinement of 0.5 nm in the region occupied by the NP. Optical constants of Ag are taken from Palik [92] and fitted using a Drude-Lorentz model. Optical constants of Si, polymer blend and Fe_2O_3 were taken from Refs. [92, 108, 109] respectively. A broadband (wavelength 300-1100 nm) plane wave is incident on the NP from the top. Frequency-domain field and index monitors are placed over the entire simulation volume to determine the electric field intensity and the complex refractive index in each mesh-cell of the simulation volume. The optical power absorbed in the semiconductor and in the Ag NP are calculated according to

$$P_{abs}(\omega) = \frac{1}{2}\omega \int \mathrm{Im}(n(x,y,z,\omega))|E(x,y,z,\omega)|^2 dV \tag{5.1}$$

where ω is the angular frequency, n the refractive index, E the electric field vector, and the integration is carried over the volume occupied by the semiconductor and the NP, respectively. In order to study the plasmonic near-field absorption, a relatively small simulation volume was chosen, such that absorption of light that is resonantly scattered from the NP is negligible. The situation of a realistic device geometry, where resonant scattering also plays a role, will be considered in the last part of this Chapter. The simulation setup also allows to determine the optical power leaving the simulation volume, which corresponds to light that is neither absorbed in the NP nor in its near field.

Figure 5.1(a) shows the simulated absorption spectra of a bare crystalline silicon (c-Si) volume (black dashed line), of a c-Si volume with a 30 nm diameter Ag NP (blue) and of the Ag NP (red). Note that the absorption spectra of the bare Si volume and of the volume containing the NP are obtained by integrating Eq. 5.1 over the volumes occupied by the semiconductor only, which are different in the two cases due to the absence or presence of the NP. The absorption spectrum of the NP shows a clear peak at a wavelength of 870 nm, coinciding with the dipolar plasmonic resonance of the NP embedded in Si (n=3.5-4.0). The graph for absorption in Si with the embedded NP shows a strong peak at the dipolar resonance, corresponding to enhanced absorption in the Si due to the plasmonic near field. As can be seen, the absorption in the semiconductor is enhanced up to a factor 5 compared to the absorption in the bare semiconductor. It is important to note that despite the

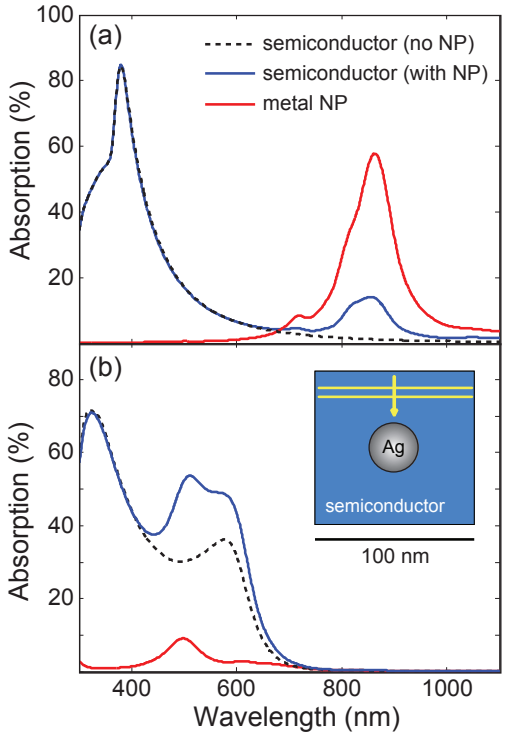

Figure 5.1: Simulated absorption spectra of a bare substrate (black dashed line), absorption in the substrate with a 30-nm-diameter Ag NP (blue) and absorption in the Ag NP (red), for a c-Si **(a)** and a PF10TBT:PCBM **(b)** hosting semiconductors. A clear increase in absorption is observed for wavelengths around the NP plasmon resonance. In the case of a c-Si substrate, the near-field absorption in the NP is much stronger than in the semiconductor. The inset shows a sketch of the simulation geometry.

strong absorption enhancement at resonance, the overall absorption in the c-Si volume with the NP is only 15% at this wavelength, a value well below that of the absorption losses in the Ag NP (59%). This is due to the fact that the LSPR occurs at a wavelength where c-Si is poorly absorbing (absorption length in c-Si is 10 μm at λ=870 nm), and therefore the plasmon energy dissipation occurs mostly in the metal.

Figure 5.1(b) shows a similar graph for the polymer poly[9,9-didecanefluorene-alt-(bis-thienylene) benzothiadiazole] blended with the fullerene derivative [6,6]-phenyl-C61-butyric acid methyl ester (PF10TBT:PCBM), which is commonly used in organic solar cells [108]. A clear LSPR peak is observed in the NP absorption spectrum (red) at λ=500 nm. It is strongly blue-shifted compared to the case for Si shown in Fig. 5.1(a) due to the low refractive index of the polymer (n=1.9). Ab-

sorption of the substrate containing the NP (blue) is enhanced with respect to absorption in the bare organic material (black dashed line) in the spectral range near the plasmonic dipole resonance, similar to the case for Si in Fig. 5.1(a). In this case however, the overall absorption in the substrate with the NP (53% at resonance) is much larger than the absorption in the metal (9% at resonance). This is due to the fact that the LSPR occurs in a spectral range where the absorption of the polymer is strong. Moreover, due to the lower index of the PF10TBT:PCBM, a larger fraction of the plasmonic near-field is in the semiconductor, leading to a stronger absorption enhancement.

Comparing Fig. 5.1(a) and Fig. 5.1(b) shows that high absolute absorption in a semiconductor hosting plasmonic NPs can only be achieved in a wavelength range where the semiconductor itself is quite strongly absorbing.

The plasmonic resonance wavelength is determined by the refractive index of the embedding medium, which is fixed for a given material, and by the particle size, which can be changed. To study the effect of particle size, we have simulated the absorption spectrum for different hosting semiconductors and Ag NPs with diameters varying between 5 and 60 nm. In each case, an average absorptance in the semiconductor is calculated by weighing the absorption spectrum over the AM1.5 solar spectrum in the 300-1100 nm spectral range. We then define the absorption enhancement as the ratio between the average absorptance of the semiconductor hosting the NP and the average absorptance of the bare semiconductor.

Figure 5.2 shows the absorption enhancement (left axes) as a function of the particle diameter, for c-Si (a), PF10TBT:PCBM (b), amorphous silicon (a-Si, c) and iron oxide (Fe_2O_3, d) hosting materials. The latter is a semiconductor commonly used for water splitting applications [109]. We study a-Si because it is used as a model system in many light trapping experiments. The trends in the data for a-Si could be taken representative for other high-index direct bandgap semiconductors such as GaAs. The average absorptance is also shown for reference (right axes). In each graph, the inset shows the NP plasmon resonance wavelengths as a function of particle diameter. The black lines indicate the dipole resonance (D) and the red lines refer to the quadrupole resonance (Q). This latter is observed only for particles larger than 30 nm in optical media with relatively large refractive index (e.g., c-Si and a-Si).

Figure 5.2(a) shows that the absorption in a c-Si layer can be enhanced by at most 20% by the presence of a silver NP (left axis in the graph), provided large (>35 nm) diameter NPs are used. This behavior seems in contradiction with the fact that for larger NPs the resonance shifts towards larger wavelengths, i.e. to a spectral region where silicon is less absorbing. However, this effect is counterbalanced both by the increase of the particle near-field volume in the Si and the larger absorption cross section for larger particles. Furthermore, for particle diameters larger than 30 nm the onset of a quadrupole resonance in the 700-800 nm spectral range is observed (see inset, red line). This resonance also contributes to enhanced near-field absorption in the c-Si. Overall, the absorption enhancement in c-Si is thus limited to 20%, while the average absorptance of the c-Si substrate remains below

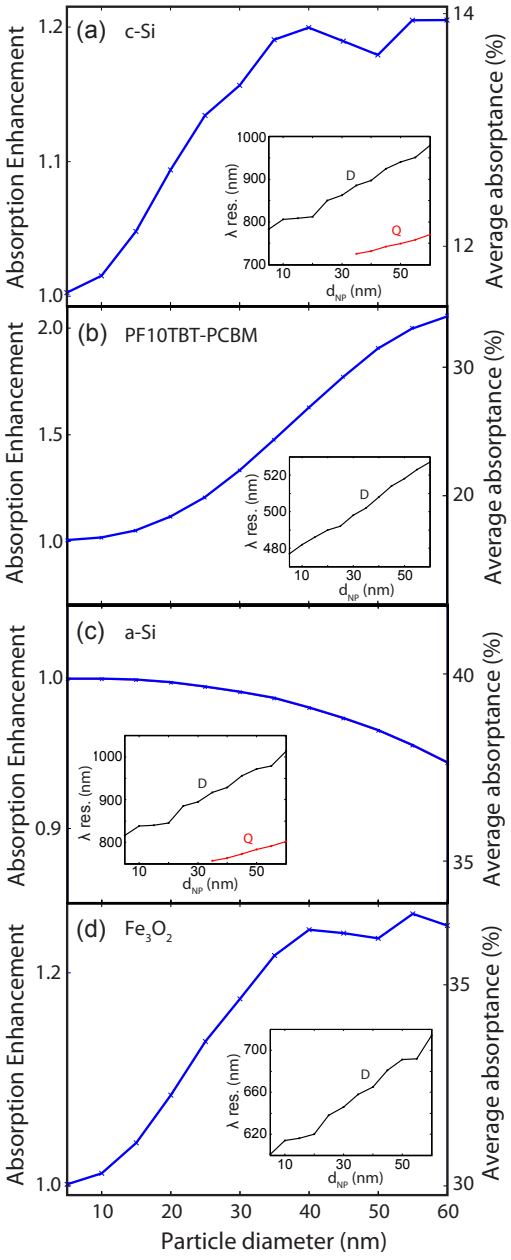

Figure 5.2: Absorption enhancement (left axis) and average absorptance (right axis), weighted over the AM1.5 solar spectrum in the 300-1100 nm spectral range, as a function of the Ag NP diameter. The panels refer to c-Si **(a)**, PF10TBT:PCBM **(b)**, a-Si **(c)**, and Fe_2O_3 **(d)** embedding media. In each panel, the inset shows the dipolar (D, black) and quadrupolar (Q, red) LSPR wavelengths. An absorption enhancement up to a factor of 2 can be achieved in the polymer substrate, due to the spectral match of the LSPR resonance with the spectral range where the polymer is strongly absorbing. In c-Si or Fe_2O_3, the LSPR resonance is in a spectral region where the material is poorly absorbing, and absorption is thus strongly limited by the losses in the metal NP. In a-Si, the resonant wavelength is larger than the bandgap wavelength, and no absorption enhancement is observed.

14% (right axis in Fig. 5.2(a)). It must thus be concluded that embedding Ag NPs in c-Si does not provides a means to achieve strong NP-enhanced absorption of light in the c-Si.

Figure 5.2(b) shows that a 100% absorption enhancement can be achieved in the PF10TBT:PCBM substrate, due to the plasmonic near-field coupling. Here too, the absorption enhancement increases for larger particle diameter as a result of the increased near-field volume and larger NP absorption cross section. The average absorptance (right axis) is increased from 17% to 34% by the presence of the Ag NPs for increasing nanoparticle diameter and then levels off.

Figure 5.2(c) shows that by embedding a silver NP in an a-Si substrate the absorption in the semiconductor actually decreases for larger diameters. This is due to the fact that the plasmon resonance of Ag particles in a-Si occurs for wavelengths (see inset) that are larger than the bandgap wavelength of a-Si (750 nm). Thus, the strong interaction of light with the NP occurs in a spectral range where the material is only very poorly absorbing. The reduced absorption for larger diameters is due to the fact that in the simulations the total volume of a-Si decreases, as the simulation box size is fixed.

In the case of a Fe_2O_3 substrate (Fig. 5.2(d)), the embedded plasmonic NP enhances the absorption in the semiconductor up to a factor of 24%. The average absorptance is increased from 30% to 37%. Similarly to the case of c-Si, the resonance wavelength (inset) is below the bandgap wavelength of the material (765 nm), but in a spectral region where Fe_2O_3 is poorly absorbing [103, 109].

Overall, Fig. 5.2 demonstrates that large absorption enhancements can be achieved in several semiconductors due to the plasmonic near field enhancement. However, as observed in the spectra of Fig. 5.1, significant optical losses occur due to Ohmic dissipation in the NPs. Figure 5.3 compares the fraction of the incident power that is absorbed in the semiconductor (blue), in the metal NP (red) or is not absorbed (green), as a function of particle diameter, for c-Si (a), PF10TBT:PCBM (b), a-Si (c) and Fe_2O_3 (d). All data are averaged by weighting over the AM1.5 solar spectrum in the 300-1100 nm spectral range. Note that the non-absorbed part (green) represents the light that exits the simulation box, i.e. it accounts both for light that does not interact with the NP and for light that is scattered by the NP.

For c-Si (Fig. 5.3(a)), the graph shows that increasing the particle diameter from 5 to 60 nm drastically increases the absorption in the NP from 0 to 20%, due to the increased volume of the metal NP. On the other hand, the absorption in the c-Si (blue) is increased only from 12% to 14%. The maximum achievable absorption enhancement in the c-Si is limited by the large absorption in the metal NP. It must be concluded that the poorly absorbing indirect semiconductor Si can not be efficiently sensitized by Ag NPs. While the absorption in a very poorly absorbing Si slab can be enhanced (see Fig. 5.1) to make it slightly less poor, full absorption in the Si as desired for photovoltaic applications cannot be achieved with Ag NPs.

Figure 5.3(b) shows that increasing the particle diameter in PF10TBT:PCBM significantly increases the absorption in the polymer from 17% to 34% (see also Fig. 5.2(b)) while absorption in the NP increases from 0 to 10%. In this case, the

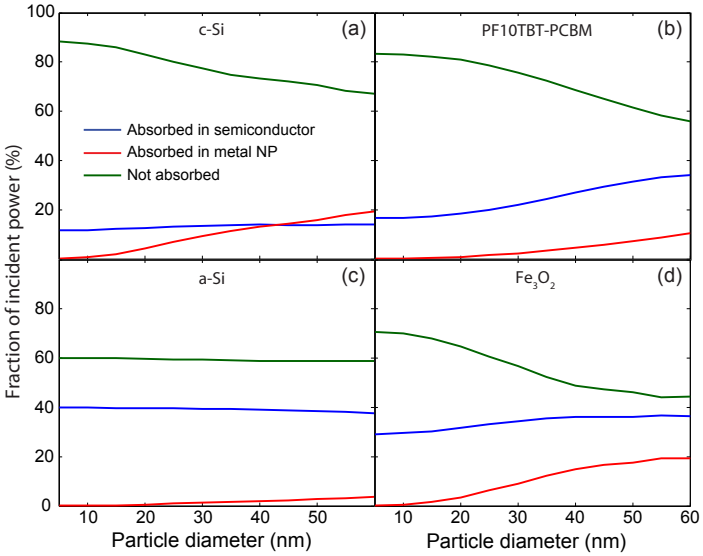

Figure 5.3: Fraction of the incident power that is absorbed in the semiconductor (blue), in the metal NP (red) or not absorbed (green), as a function of particle diameter, for c-Si **(a)**, PF10TBT:PCBM **(b)**, a-Si **(c)** and Fe_2O_3 **(d)**. All data are averaged by weighting over the AM1.5 solar spectrum in the 300-1100 nm spectral range. The reduction of the non-absorbed power (green) is associated with an increase of the absorption in the substrate and in the NP. For the polymer substrate, the absorption in the active layer is larger than the losses in the metal. For a c-Si and Fe_2O_3 substrates, the strong absorption in the NP strongly limits the plasmonic near-field absorption enhancement in the substrate. In an a-Si substrate no significant change is observed as a result of the resonant wavelength being larger than the bandgap wavelength.

absorption in the semiconductor is thus significantly enhanced while absorption in the metal remains modest (compared to the case for c-Si). The data indicate, however, that increasing diameter the relative contribution of absorption in the metal increases. For larger particles scattering of light will also become dominant, due to the larger albedo, and a reduction of the near field absorption will occur.

Figure 5.3(c) shows the data for a-Si. A very small variation in both the absorbed and the non-absorbed fraction of incident power are observed as the particle diameter is increased from 5 to 60 nm, because the plasmon resonance occurs at a wavelength above the bandgap. The absorption in the metal NP (red) is relatively low (< 3%) because a-Si is a strong absorber. For Fe_2O_3 (Fig. 5.3(d)) a behavior similar to that for c-Si is observed. For large diameters a significant fraction of the light (20%) is absorbed in the NPs, while the absorption in the semiconductor is only slightly enhanced.

The analysis conducted so far shows the importance of matching the wavelength of the plasmon resonance with a spectral range where the hosting material

is a good absorber. In particular, for materials like c-Si and a-Si, the large refractive index shifts the resonance to larger wavelengths where these materials are poorly absorbing. One possible way to shift the plasmon resonance to shorter wavelengths is to coat the NP with a thin dielectric layer (core-shell particle). The presence of such a dielectric shell can also serve, in a photovoltaic device, as an electrical passivation of the metal surface to avoid carrier recombination at the NP interface.

We have simulated the absorption cross-section spectra for core-shell Ag-SiO_2 particles embedded in a c-Si substrate (see inset in Fig. 5.4(b)). The core particle diameter is 30 nm, and the shell thickness is varied between 0 and 5 nm. Figure 5.4(a) shows the LSPR resonance wavelength as a function of the shell thickness. A strong blue shift is observed as the shell thickness increases, as expected due to the reduced refractive index in the plasmonic near field. Figure 5.4(a) (top axis) also shows the absorption coefficient of c-Si as function of wavelength. The graph shows that increasing the shell thickness to 5 nm shifts the resonance to a spectral range where the c-Si is more strongly absorbing.

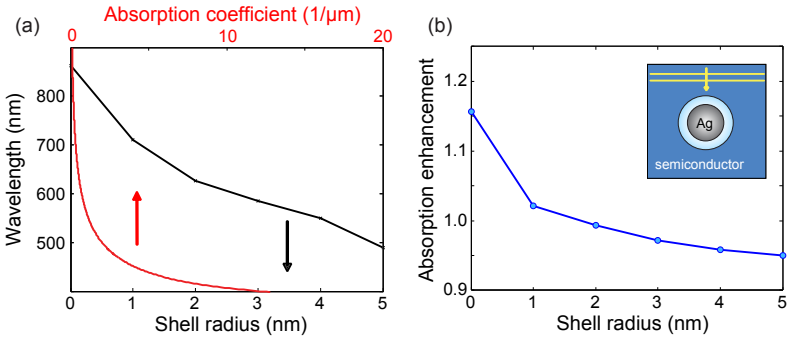

Figure 5.4: **(a)** LSPR dipolar resonance wavelength (black line, vertical axis) as a function of the shell thickness (bottom axis), for a Ag/SiO_2 core-shell particle embedded in a c-Si layer. The Ag core diameter is 30 nm. A strong blue shift is observed as the silica shell thickness increases. Also shown is the absorption coefficient of c-Si (red line, top axis) as a function of wavelength. Increasing the shell thickness shifts the resonance into a spectral range where Si is more absorbing. **(b)** Absorption enhancement, averaged by weighting over the AM1.5 solar spectrum in the 300-1100 nm spectral range, in the c-Si substrate as a function of the shell thickness. A reduction in absorption is observed for larger shell thicknesses as a result of the reduced overlap of the near-field with the active material.

Figure 5.4(b) shows the absorption enhancement in the c-Si substrate as a function of the shell thickness, again integrated over the AM1.5 solar spectrum from 300-1100 nm. The graph shows a clear reduction of the absorption enhancement as the shell thickness increases. Despite the fact that the dipole resonance is shifted into a spectral range where c-Si is more absorbing, the fraction of the near-field that overlaps with the c-Si substrate is reduced due to the presence of the dielectric layer around the particle. The net effect is a reduction of the absorption in the semicon-

ductor layer. Similar results were found for all other semiconductors shown in Figs. 5.2 and 5.3. The use of a dielectric shell to tune the LSPR is thus not an effective way to enhance the absorption in the semiconductor.

An alternative way to tune the NP plasmonic resonance is by changing its shape. Figure 5.5 shows the average absorption, integrated over the AM1.5 solar spectrum for prolate (crosses) and oblate (circles) Ag spheroids with size aspect ratios ranging from 0.1-1.0. Data are shown for a spheroidal NP embedded in c-Si (a) and PF10TBT:PCBM (b) The particle volume for the spheroids is kept equal to that of a 30-nm-diameter sphere. Absorption in the semiconductor (blue) and in the Ag NP (red) is shown as a function of the size aspect ratio (short over long axis length) of the spheroid. The data for size aspect ratio 1 (i.e. spheres) equals that in the corresponding panels of Fig. 5.3. The absorption in a semiconductor volume without the NP is shown for reference in Fig. 5.5 (dashed black line).

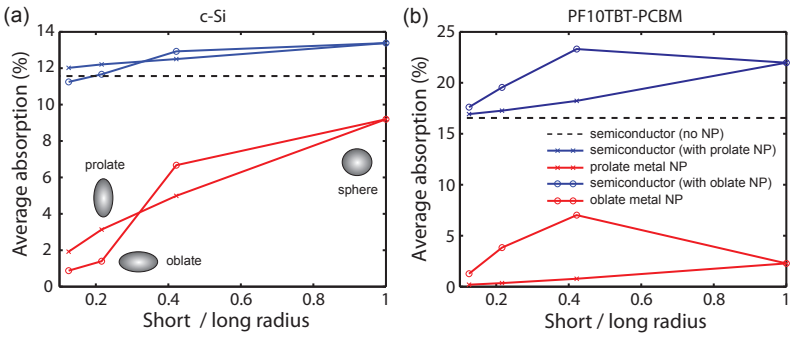

Figure 5.5: AM1.5 averaged absorption in c-Si **(a)** and PF10TBT:PCBM **(b)** for oblate (circles) and prolate (crosses) embedded Ag nanoparticles. Absorption in the semiconductor (blue) and in the metal NP (red) is shown as a function of the ratio of the short radius over the long radius of the spheroid. The absorption of a bare semiconductor volume is shown for reference (dashed black line). The graph shows that an increase in the absorption in the semiconductor due to the presence of the NP is always associated with strong Ohmic losses in the metal NP.

For the case of c-Si (Fig. 5.5(a)), changing the particle shape from spherical to spheroidal leads to a reduction of the absorption in c-Si for all aspect ratios. This is due to a reduced near-field intensity for prolate spheroids, and the red-shift of the plasmonic resonance in the case of oblate spheroids. For the case of PF10TBT:PCBM (5(b)), the absorption in the polymer for an oblate spheroid with a ratio of short over long radius of about 0.4 (23.7%) is slightly larger than the case of a spherical particle (22%). However, this increase is accompanied by an even higher increase of Ohmic losses in the metal NP (from 2% in a sphere to 7% in an oblate spheroid). For prolate NPs a reduction of the absorption in the polymer semiconductor is observed for all aspect ratios, compared to spherical NPs. Overall, Fig. 5.5 shows that also for spheroidal particles absorption enhancement in the semiconductor can only be achieved at the expenses of strong Ohmic losses in the

metal.

So far only the absorption of the local field around a single NP in a single 100-nm-box has been considered. In order to extend our study to a realistic planar device geometry, we consider square arrays of Ag NPs embedded in a 100-nm-thick semiconductor layer, infinitely extended in the two in-plane directions by using Periodic Boundary Conditions (PBCs). Figure 5.6 shows the average absorption, weighed over the AM1.5 solar spectrum, for arrays of silver NPs embedded in a c-Si (a) and PF10TBT:PCBM (b) layer. In each panel, the absorption in the hosting material (blue lines) and in the metal NPs (red lines) is shown as a function of the ratio of the array pitch over the particle diameter, for particles with 5 nm (dash-dotted lines) or 40 nm (dashed lines) diameter. The absorption in a substrate without NPs is shown for reference (black solid line).

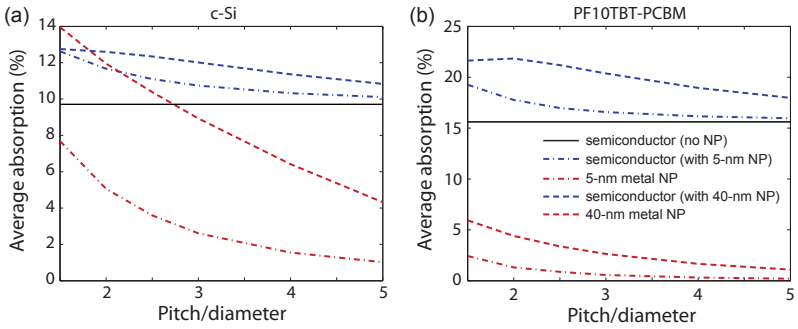

Figure 5.6: Average absorption for arrays of silver NPs embedded in a c-Si **(a)** and PF10TBT:PCBM **(b)** substrate. Data are plotted for particles with 5 nm (dash-dotted lines) and 40 nm (dashed lines) diameter, as a function of the ratio of the array pitch over the particle diameter. Absorption in the hosting material is shown in blue, absorption in the metal NPs is shown in red. The absorption in a substrate without NPs is shown for reference (black solid line). For both c-Si and PF10TBT:PCBM, the highest absorption in the semiconductor is achieved for NP arrays with short inter-particle distance compared to the NP size. In the case of c-Si **(a)**, the increase in absorption in the c-Si layer comes at the expense of a significant increase in the Ohmic losses in the metal NPs.

Figure 5.6(a) shows that for c-Si the highest absorption (13%) can be achieved for the smallest array pitch (i.e. equal to 1.5 times the NP diameter), a result that is in agreement with the previous work by Vedraine *et al.* [70, 110]. This can be explained by a stronger overall interaction of the NPs with the incident light when they are packed closer together. Despite the absorption increases with respect to a layer without nanoparticles (black line, 9.6%), it must be noted that for such configurations the absorption in the metal NP due to Ohmic losses is also significantly increased, up to a value of 14% (i.e. higher than the absorption in the c-Si). The large Ohmic losses are a direct consequence of the higher density of metal NPs in the layer. Once again, we must conclude that c-Si cannot be efficiently sensitized by Ag NPs.

Figure 5.6(b) shows a similar graph for a PF10TBT:PCBM layer. In this case, the largest absorption is obtained for arrays with a pitch equal to 1.5 and 2 times the NP diameter, for 5-nm- and 40-nm-diameter particles, respectively. The absorption of a layer without NPs (16%) is increased to 22% for an array of 40-nm-diameter NPs with 80 nm pitch. Similarly to the case of c-Si, the increase in absorption in the polymer layer always comes at the expense of increased Ohmic losses in the metal.

Finally, we study the dependence of absorption in a semiconductor with embedded Ag NPs on the thickness of the semiconductor layer. We consider a square array of 40-nm-diameter Ag NPs, spaced by 100 nm, and placed 40 nm below the semiconductor surface. A sketch of the simulation geometry is shown in Fig. 5.7(a). The NP array is placed 40 nm below the surface of the semiconductor.

As a first step, we calculate the absorption profiles as a function of depth. Figure 5.7(b) shows the absorptance per unit length (top axis) as a function of depth (right axis) for a bare c-Si substrate (black), in a c-Si substrate with embedded Ag NPs (blue) and in the Ag NP array (red). The graph shows that, in the proximity of the NPs (i.e. for depths smaller than 80 nm), the absorption in the c-Si is enhanced by the presence of the NP due to the strong plasmonic near field (see also Fig. 5.1(a)). Similarly to Fig. 5.1(a), the absorption in the c-Si with the NP is limited by the large absorption in the metal (red line). Absorption in the Ag particles is 2 to 3 times stronger than in the c-Si. In the region beyond the NPs (i.e. for depths larger than 80 nm), the absorption of the c-Si with the NPs is slightly lower than that of the bare c-Si substrate, due to the fact that more light is absorbed in the top layer (either in the semiconductor or in the metal). A similar qualitative behavior is observed for Ag NPs embedded in a PF10TBT:PCBM layer (Fig. 5.7(c)). In this case however, a significant absorption enhancement is observed for the polymer containing the NP array (blue) with respect to the bare polymer (black), in the proximity of the NP array. The absorption in the NPs (red) is less than one third of the absorption in the polymer, similarly to what was shown in Fig. 5.1(b). In the region beyond the NP array, the absorption in the bare polymer substrate is higher than that of the polymer containing the NP array, due to the stronger absorption in the near-field region.

The data shown in 7(b) and 7(c) can be used to calculate the absorptance for layers of different thicknesses, by integrating the absorptance per unit length over the depth, according to: $A(t) = \int_0^t a(x)dx$, where a is the absorptance per unit length at the depth x, t is the thickness and A is the absorptance. Figure 5.7(d) shows the absorptance as a function of layer thickness for a bare c-Si substrate (black) and a c-Si substrate containing the NP array (blue). For layers thinner than 1 micron, the absorptance is enhanced by the presence of the NP array. This is due to the fact that the bare layer is poorly absorbing and the absorptance is enhanced by the strong near field of the particle. For a layer of 1 micron, however, the absorption of the bare layer is equal to the absorption in the layer containing the NP. In fact, in the limit of very thick layers (not shown here), the bare c-Si fully absorbs the light transmitted in the layer, but the absorption in the layer with the NPs is limited by the metal losses. Thus the two curves cross at a thickness of about 1 micron.

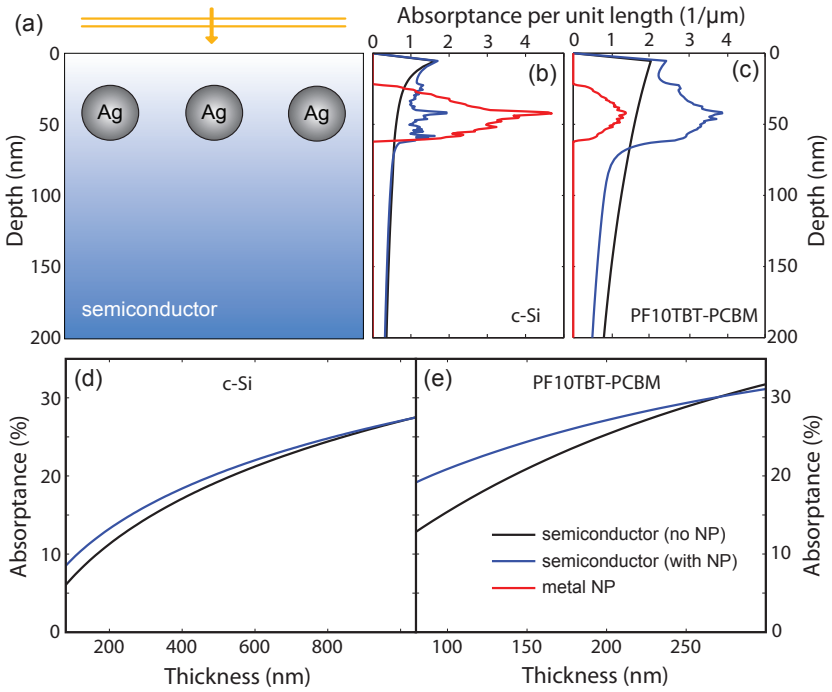

Figure 5.7: **(a)** Sketch of the simulation geometry. A square array of 40-nm-diameter Ag NPs, spaced by 100 nm, is placed 40 nm below the surface of a semi-infinite semiconductor layer. **(b, c)**) Absorptance per unit length (top axis) as a function of depth (right axis) for a bare substrate (black), in a substrate with embedded Ag NPs (blue) and in the Ag NP array (red), for c-Si **(b)** and PF10TBT:PCBM **(c)**. Absorption in the active layer is enhanced by the presence of the NP in the proximity of the NP due to the strong plasmonic near field. **(d, e)** Absorptance in a bare substrate (black) and in a substrate containing a Ag NP array (blue), for a c-Si **(d)** and PF10TBT:PCBM **(e)** substrates, as a function of layer thickness. For thinner layers, absorption is enhanced by the LSPR near field of the NP. For thicker layers, the bare substrate shows larger absorption than a substrate with NPs, as a result of the metal losses in the latter.

The same behavior is observed for PF10TBT:PCBM (Fig. 5.7(e)). In this case, a significant absorption enhancement is observed for layer thicknesses below 200 nm. For example, the absorptance of a 100 nm thick layer increases from 15% to 21% due to the presence of the NP array. We note that the same absorptance is achieveble with a 170 nm layer of bare polymer, and thus the NP array allows reducing the layer thickness by 40% for the same absorption. This is advantageous given the very low carrier diffusion length in the polymer (order of 10 nm), which limits the thickness of a photovoltaic device to less than 100 nm.

5.3 Discussion and conclusion

Metal NPs embedded in a semiconductor material enhance light absorption in the semiconductor, due to the plasmonic near-field enhancement. The absorption enhancement occurs at wavelengths close to the LSPR of the metal NP, which depends on particle size, shape, inter-particle spacing and on the refractive index and thickness of the embedding layer. In all studied geometries and semiconductor materials, strong unwanted absorption occurs by Ohmic dissipation in the metal NPs. For a poorly absorbing semiconductor such as c-Si, Ohmic dissipation in the metal is the dominant loss mechanism. In fact, in c-Si only a small (20%) absorption enhancement is observed at the expense of large absorption losses in the metal. We conclude it is not practical to sensitize c-Si with Ag NPs. For a 100-nm thick PF10TBT:PCBM layer, the total absorbance, integrated over the solar spectrum from 300-1100 nm, is enhanced from 17% to 34%. For thicker layers or higher NP concentrations, the ultimate absorbance that can be achieved is limited by the Ohmic dissipation in the metal (10%, see Fig. 5.3(b)), which constitutes about one quarter of the total absorbance for large NPs (44%, metal + semiconductor). Similarly, an absorption enhancement up to only 24% is found for Fe_2O_3 layers. Here too, about one third of the total absorbance (57%, metal + semiconductor) in the NP-doped layer is due to Ohmic losses in the metal (20%). No absorption enhancement was found for a particle embedded in a-Si, due to the fact that the LSPR wavelength is larger than the bandgap wavelength of a-Si. We found that the use of core-shell particles, in order to shift the LSPR resonance in a spectral range where absorption is larger, is ineffective, due to the reduced overlap of the near-field with the active material. Similarly, the use of spheroidal particle is ineffective due to the reduced near-field intensity for spheroids with respect to spheres.

The strong near-field absorption enhancement can be used to reduce the thickness of a thin-film solar cell without a reduction of optical absorption. This is particularly useful for photovoltaic material, such as the polymer considered in this work, where the short carrier diffusion length limits the thickness of the cell. We have shown that the layer thickness of a polymer solar cell can be reduced from 170 to 100 nm by adding Ag NPs. Nonetheless, it must be stressed that none of the NP-sensitized geometries enable to achieve full absorbance in the semiconductor.

Finally, we note that in this work the effect of light scattering have been only marginally considered. Further studies are required to investigate the possible benefits of scattering on light absorption in the active layer.

6

Broadband omnidirectional antireflection coating based on subwavelength surface Mie resonators

We present an entirely new concept that allows suppressing the reflection of light from a silicon surface over a broad spectral range. A two-dimensional periodic array of sub-wavelength silicon nanocylinders designed to possess strongly substrate-coupled Mie resonances yields almost zero total reflectance over the entire spectral range from the ultraviolet to the near-infrared. This new antireflection concept relies on the strong forward scattering that occurs when a scattering structure is placed in close proximity to a high-index substrate with a high optical density of states.

6.1 Introduction

Reflection is a natural phenomenon that occurs when light passes the interface between materials with different refractive index. In many applications, such as solar cells or photodetectors, reflection is an unwanted loss process. Many different ideas have been developed over the years in order to reduce reflection in optical and optoelectronic devices [111, 112]. A single transparent dielectric layer is commonly used as an anti-reflection (AR) coating. Based on destructive interference between the incident and reflected light, perfect optical impedance matching can

be achieved for one specific wavelength [113]. Micron-sized pyramidal surface texturing is also widely used in e.g. crystalline silicon solar cells [114, 115]. The angular randomization of the scattered light at the surface can increase light absorption in an optical medium up to a factor of $4n^2$ [41, 116]. Surface structures composed of periodic or random arrays of semiconductor nanowires and nano-pyramids have also proven to reduce reflection over a broad range of wavelengths and angles of incidence [117–124]. The reduced reflection is due to multiple scattering of light as well as adiabatic coupling due to a gradually increasing refractive index towards the substrate surface [125–130]. Recently, we have shown that optimized arrays of metal nanoparticles reduce reflection of Si in the range of wavelengths relevant for solar applications [40, 53]. The preferential forward scattering by the plasmonic point scatterers [51] strongly reduces the reflection, thus allowing almost perfect impedance matching of sunlight into a Si wafer.

Here, we present an entirely new concept to eliminate reflection from a silicon wafer that makes use of much simpler nanostructures than the ones reported before, does not involve metals, and can be applied to any high-index material. It is based on the fact that dielectric nanoscatterers possess geometrical Mie resonances with scattering cross sections larger than the geometrical ones [48, 83]. A recent paper by Cao et al. has shown [131] that Mie resonances provide a very efficient mechanism for light absorption in Si nanowire based solar cells. In that work, however, Si nanowires were on a glass substrate and only absorption in the nanowires was considered. In this Chapter, we demonstrate that light that is stored in Mie resonances can be also very efficiently coupled to a Si substrate. From a fundamental point of view this light coupling mechanism based on weak (lossy) Mie resonances is entirely different than all other methods commonly known in the field of anti-reflection coatings. We demonstrate experimentally that an array of low aspect-ratio Si nanocylinders etched into a Si wafer shows an average reflectivity as low as 1.3% in the 450-900 nm spectral range. The strongly reduced reflectivity is observed for angles of incidence up to 60 degrees. The monolithic nature of the nanostructures makes this novel anti-reflection concept to be easily applicable to a wide range of devices, including (ultra-thin) solar cells based on any high-index semiconductor [55].

6.2 Mie scattering on a Si substrate

Figure 6.1(a) shows the calculated scattering cross section spectra, normalized to the geometrical cross section, for a Si sphere in air (blue) and a Si sphere (green) and cylinder (red) on top of a Si substrate. The scattering spectrum for the sphere in air shows two distinct resonances corresponding to the first- and second-order Mie modes. These geometrical resonances reflect the fact that the particle acts as a nano-cavity for light. The scattering cross section at resonance is more than 8 times larger than the geometrical cross section, and the cavity quality factor (Q = 10) is mostly determined by radiation losses from the cavity mode. The two

scattering resonances are clearly visible when a Si substrate is introduced below the spherical particle (green line), indicating only weak coupling of the well-confined Mie modes to the substrate. However, when a cylindrical nanoparticle is placed on the Si substrate, the resonances broaden and merge into a broadband feature (red line). This behaviour is due to the introduction of a leaky channel into the substrate for the light that is resonantly confined in the particle.

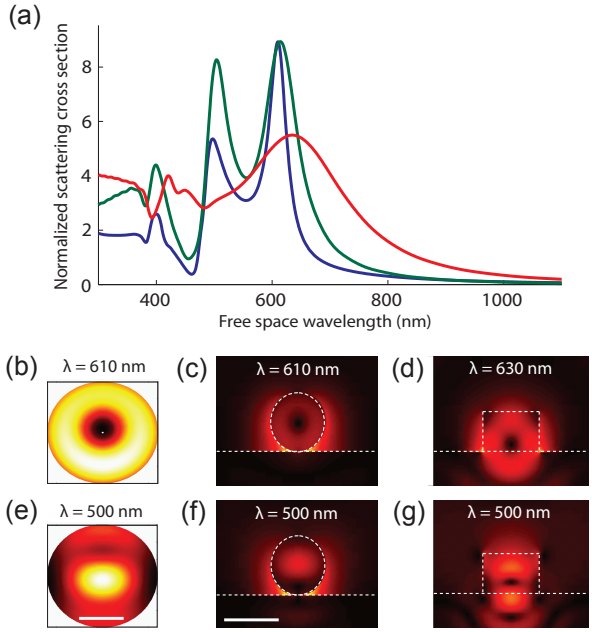

Figure 6.1: Mie scattering on a Si wafer. **(a)** Scattering cross sections, normalized to the geometrical cross section, for a Si sphere in air (blue), a Si sphere on a Si substrate (green) and a Si cylinder on a Si substrate (red). The spheres have diameter d = 150 nm, the cylinder an in-plane diameter of 150 nm and height of 100 nm. Mie resonances of first (n = 1) and second (n = 2) order are indicated in the figure. **(b-g)** Electric field intensity (color scale) in a cross section of the particle for a sphere in air **(b, e)**, a sphere on substrate **(c, f)** and a cylinder on substrate **(d, g)**, for Mie modes of first **(b-d)** and second **(e-g)** order. The wavelengths considered for these calculations are indicated in each panel. The field distribution for the cylinder at resonance overlaps with the substrate, thus introducing a loss channel for the light confined in the particle that broadens the resonances. Plots for a sphere in air are calculated with Mie theory; plots for particles on a substrate are simulated. The scale bar in **(e)** represents 50 nm, and refers to **(b)** and **(e)**. The scale bar in **(f)** represents 150 nm and refers to **(c)**, **(d)**, **(f)** and **(g)**.

To understand this mechanism, Figs. 6.1(b)-(g) show the calculated distribution of light (electric field intensity, color scale) inside a Si sphere in air (b, e), a Si sphere on a Si substrate (c, f) and a Si cylinder on a Si substrate (d, g), for Mie modes of

first (b-d) and second (e-g) order. Comparison of the field distributions shows that the geometrical modes inside a spherical Si particle are nearly unaffected by the presence of the substrate and light is in both cases well confined inside the particle. However, for a cylindrical particle the field distribution of the Mie resonances has a clear overlap with the Si substrate. Both direct near-field absorption in the substrate and radiative emission into the substrate introduce a loss channel for the light confined in the particle, thus yielding broadening of the resonances in the scattering cross section spectrum (Q~5, see also supplementary Fig. 6.6). The field distributions in Figs. 6.1(b)-(g) suggest that a cylindrical Si nanoparticle can effectively couple light into a Si substrate.

To study this further we perform simulations of the reflectance spectra of cylindrical nanopillar (NP) arrays with different NP dimensions. Figure 6.2(a) shows the simulated total reflectance spectra from a square array of Si NPs spaced by 500 nm, for cylinder diameters of 75, 100 and 125 nm. The reflectance from a bare flat Si surface (35-60%) is also shown for comparison (black line).

The data in Fig. 6.2(a) show that the dielectric particle array reduces the reflectance of a Si surface over the entire spectral range shown. The key role of the Mie resonances in the reduced reflection is clear from the fact that broad reflection dips are observed on resonance, at wavelengths (700, 830, 1000 nm) that increase with nanopillar diameter (150, 200, 250 nm). This redshift for increasing diameter is similar to that observed for Mie resonances for isolated particles with increasing diameter (see supplementary Fig. 6.6). The sharp decrease in reflectivity at the wavelength of 500 nm, i.e. equal to the array pitch, is explained by a Rayleigh anomaly [132] from the grating formed by the regular array of nanoparticles (see supplementary Fig. 6.7). The strong coupling of light on resonance is explained by the strong forward scattering of light into the substrate from the resonant Mie scatterers, due to the high optical mode density of the high-index Si substrate [99]. The resonant nature of this effect leads to a large cross section, so that even an array of scatterers covering only 30% of the surface area leads to nearly complete interaction with the incoming plane wave.

Figure 6.2(b) shows the simulated reflectivity spectra for a bare flat Si substrate (black), a flat Si substrate coated with a standard 80 nm Si_3N_4 anti-reflection coating (blue), a Si surface with bare Si NP on top (green), and a Si surface with Si NP on top coated with a 50 nm Si_3N_4 layer (red). Given its index (n = 2.0), Si_3N_4 is the optimum antireflection coating for a Si wafer (n = 3.5-4.0 in the visible-to-near-infrared spectral range). As can be seen in the figure, it only leads to vanishing reflectivity for a specific wavelength (650 nm in Fig. 6.2(b)), determined by the Si_3N_4 layer thickness. The bare array of Si NPs shows a broadband reduced reflectivity spectrum that is lower than that for the standard AR coating above 850 nm and below 550 nm, and higher in the range 550-850 nm. Both spectra show a large increase in reflectivity for wavelengths below 500 nm. A Si_3N_4 layer with properly chosen thickness can be used as a coating, conformal to the nanostructures, in order to compensate for the losses in this spectral region. The reflectance spectrum from a coated array of NPs (Fig. 6.2(b), red) shows that reflectivity can be

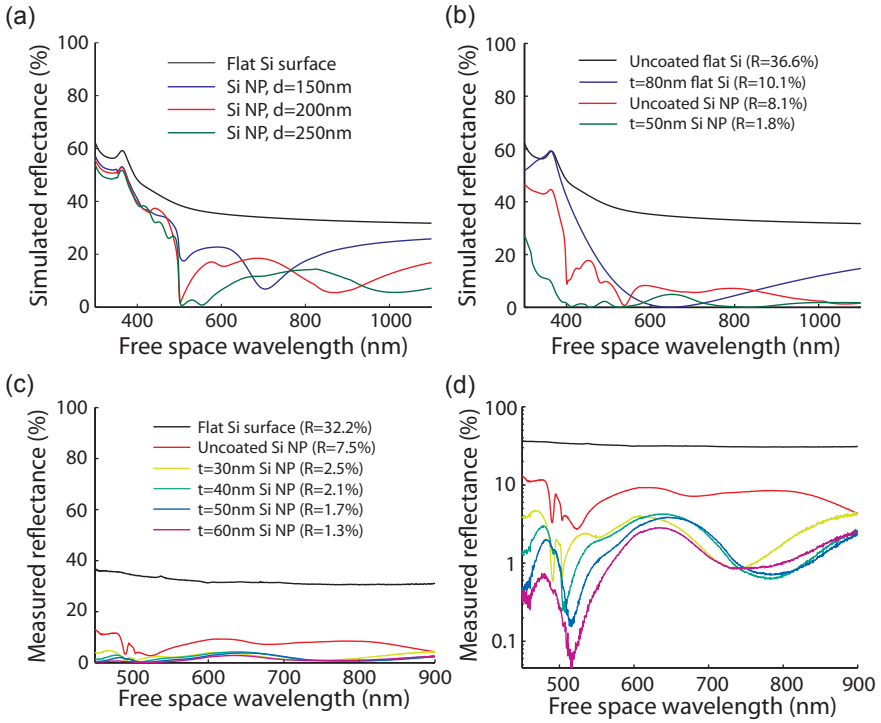

Figure 6.2: Ultra-low reflectivities. **(a)** Simulated reflection spectra from a regular square array of Si NPs spaced by 500 nm, for cylinder diameters of 150 (blue), 200 (red) and 250 nm (green) with a height of 150 nm. Reflectance from a flat Si surface is also shown for comparison (black). The Si NP arrays reduce the reflectivity over the entire spectrum. The broad dip in reflectivity that redshifts for increasing particle diameter is due to enhanced forward scattering from the Mie resonances in the particle. **(b)** Simulated reflection spectra for a bare flat Si substrate (black), a flat Si substrate coated with a standard Si_3N_4 anti-reflection coating (blue, thickness t = 80 nm), a Si surface with bare Si nanostructures on top (green), and a Si surface with Si nanostructures on top coated with an optimized Si_3N_4 layer (red, t = 50 nm). For each configuration the average reflectivity, weighted with the AM1.5 solar spectrum in the 300-1100 nm spectral range, is indicated (R). **(c)** Measured total reflectivity of a bare Si wafer (black), an uncoated Si NP array (red) and four Si NP array coated with Si_3N_4 layers of different thicknesses t (colors). The Si NPs have a diameter of 125 nm, height of 150 nm and are spaced by 450 nm. For each configuration the average reflectivity, weighted with the AM1.5 solar spectrum in the 450-900 nm spectral range, is indicated (R). Reflectance is reduced over the entire spectral range, due to coupling of the Mie resonant scattering to the Si substrate. **(d)** Same reflectivity data plotted in logarithmic scale. Individual curves are described by legend of Fig. 6.3c. The effect of the Mie resonance is visible in the broad dip in reflectivity observed in the 700-800 nm range.

reduced down to less than 2% over the entire spectral range from 400-1100 nm, with the exception of a small peak around 650 nm. The low reflectivity stems from the combined effect of the strongly coupled Mie resonances in the red and near-IR part of the spectrum and the interference anti-reflection effect from the Si_3N_4 layer, tuned for the blue part of the spectrum. Figure 6.2(b) also shows the average reflectivities for each configuration, obtained by weighting over the AM1.5 solar spectrum in the 300-1100 nm spectral range. As can be seen, both coated (1.8%) and uncoated nanopillar arrays (8.1%) show lower reflectivity than the standard 80 nm Si_3N_4 coating (10.3%).

6.3 Black silicon

The antireflection properties of Si NP arrays have been studied experimentally using Si(100) wafers on which square arrays of Si nanocylinders (250 nm diameter, 150 nm height, 450 nm pitch) were fabricated using substrate conformal soft-imprint lithography in combination with reactive ion etching. The total hemispherical reflectivity was measured using an integrating sphere, with an angle of incidence (AOI) of 8° off the surface normal. Figure 6.2(c) shows the measured total reflectivity spectrum of a bare Si wafer (black), of a bare Si NP array (red) and four Si NP arrays coated with different Si_3N_4 layer thicknesses (green to purple color lines). All geometries show reduced reflectivity with respect to the bare Si wafer, over the entire spectral range. The array coated with a 60 nm thick Si_3N_4 layer (purple line) shows a reflectivity of less than 3% over the entire spectral range 450-900 nm. The AM1.5-averaged reflectance from a bare Si substrate (32.2%, black) is reduced to 7.5% by patterning the Si surface with an optimized Si nanopillar array (red). Combining Si NPs and a Si_3N_4 coating leads to an average reflectivity as low as 1.3% (blue). This value is in excellent agreement with the calculated data in Fig. 6.2(b), taking into account the different spectral range over which the average reflectivity is calculated (see supplementary Fig. 6.10). An average reflectivity of 1.3% is lower than that of standard antireflection schemes used for commercial crystalline Si solar cells (see supplementary Fig. 6.9). Figure 6.2(d) shows the same reflectivity spectra plotted on a logarithmic scale. The broad dip in the reflectivity spectra at wavelengths between 650-850 nm, is attributed to the first-order coupled Mie resonances. The sharp dips at a wavelength of about 510 nm are consistent with a Rayleigh anomaly for light incident with an AOI of 8° (see supplementary Fig. 6.11).

With the reflection of light effectively vanished, light is then either transmitted into the Si substrate or absorbed in the NPs. For example, for silicon in the 800-1000 nm spectral range the linear absorption over the thickness of the nanocylinders is less than 1%; it is enhanced in the cavity by the quality factor Q~3. Indeed, simulations (see supplementary Fig. 6.8) show that in this spectral range absorption in the NPs is negligible and the NPs behave as almost pure scatterers (i.e. the albedo is almost 1). For the UV/blue spectral range, Si is strongly absorbing and light is absorbed inside the Si nanocylinders. Indeed, an optimized solar cell design based

on substrate coupled Mie resonators will have the p-n junction integrated inside the nanoparticles, which can easily be done using gas-phase doping.

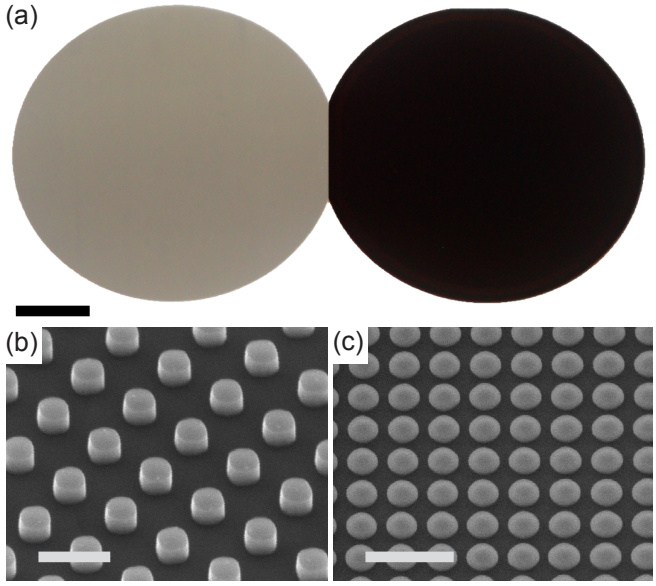

Figure 6.3: Black silicon. **(a)** Photograph of a bare flat 4-inch Si wafer (left) and a 4-inch Si wafer fully imprinted with an optimized (250 nm diameter, 150 nm height, 450 nm pitch) Si NP array and over-coated with a 60 nm thick Si_3N_4 layer (right). Scale bar represents 1 inch. **(b)** SEM image taken under an angle of 40° of a bare Si NP array (scale bar represents 500 nm) and **(c)** a Si NP array coated with a 60 nm thick Si_3N_4 layer (scale bar represents 1 μm).

Figure 6.3(a) shows a photograph of a bare flat 4-inch Si wafer (left) compared to a 4-inch Si wafer that has been patterned over the entire wafer area with an optimized Si NP array and over-coated with a 60 nm thick Si_3N_4 layer (right). The photograph shows a clear visual effect of the reduced reflectivity due to the patterning of the Si wafer surface with resonant Mie scatterers. Figure 6.3 also shows a SEM image of a bare (b) and a 60 nm Si_3N_4 coated (c) NP array. The sample shown in Fig. 6.3 was fabricated using interference lithography and soft-imprint lithography, demonstrating this new AR coating design can be applied at large-area using standard inexpensive processes.

6.4 Angle resolved reflectivity

In order to be relevant for e.g. photovoltaic applications, an AR coating must show low reflectivity over a wide range of angles of incidence and for both polarizations of light. Figure 6.4 shows the specular reflectivity measured as a function of AOI, for

wavelengths of 514 nm (a, d), 632 nm (b, e) and 405 nm (c, f). Figures 6.4(a)-(c) show reflectance for s- (solid symbols) and p-polarized (open symbols) incident beams, whereas Figs. 6.4(d)-(f) show the average reflectivity for s- and p- polarizations, plotted on a logarithmic scale. In each graph, reflectivities from a bare Si wafer (black lines), a flat Si wafer with a 60 nm standard Si_3N_4 coating (red) and a 60 nm thick Si_3N_4 coated NP array (blue) are shown.

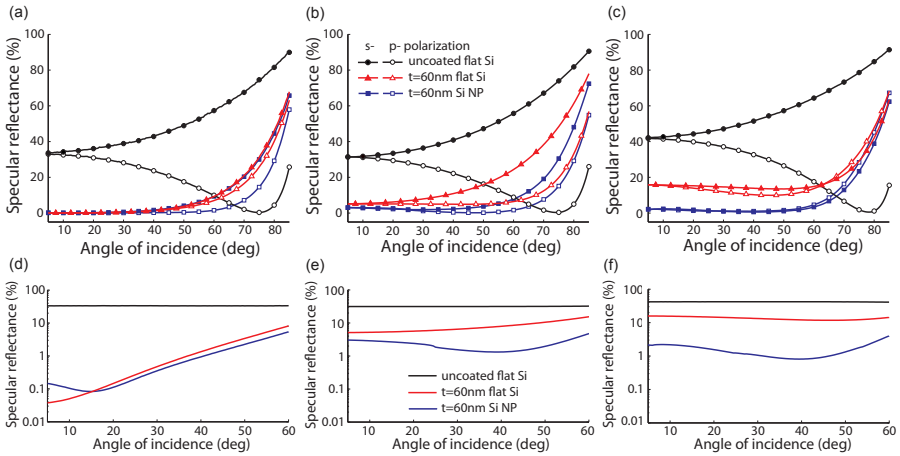

Figure 6.4: Angle resolved reflectivity. Specular reflectivity measured as a function of AOI, for wavelengths of 514 nm **(a, d)**, 632 nm **(b, e)** and 405 nm **(c, f)**. Panels in the top row show results for s- (solid symbols) and p-polarized (open symbols) incident beam, whereas the bottom row show an average of s- and p- polarizations, plotted on a logarithmic scale. In each graph, reflectivities from a bare Si wafer (black lines), a 60 nm standard Si_3N_4 coating (red) and a coated NP array (blue) are shown. The excellent AR properties of Si NP arrays are maintained over the entire range of AOI from -60 to +60 degrees.

At a wavelength of 514 nm, the 60 nm standard coating and the coated NP array show a total reflectivity for near-normal incidence of 0.1% and 0.05% respectively (Fig. 6.9(a)). Figure 6.4(a) shows that for both samples and polarizations the reflectivity remains below 1% in a wide range of AOI. While no difference between the standard coating and the Si NP array is seen for the s-polarization, the Si NP array shows lower reflection of p-polarized light at large angles. Averaging the two polarizations (Fig. 6.4(d)) yields similar results for the standard and the Si NP coatings, with better AR properties from the latter for angles above 14°. At wavelengths of 632 nm and 405 nm (Figs. 6.4(b) and (c), respectively), the Si NP array shows lower reflectivity than the standard Si_3N_4 coating, for both polarizations and over the entire range of AOI. As Figs. 6.4(e) and 6.4(f) show, the low reflectivity from the coated Si NP array is maintained over the entire angular range up to 60 degrees.

6.5 Random and periodic arrays of Si Mie scatterers

The configuration of Si Mie scatterers studied so far is periodic square array. However, this configuration yields extra grating effects that affect the reflectivity, as already shown in Fig. 6.2 and in the supplementary Fig. 6.7. In order to decouple the collective scattering by the grating from the scattering of single Mie resonators, we study the case of a random array of Si NPs, by means of numerical simulations. The random array is generated by defining a random position for each Si NP in a 10×10 μm^2 box, with the boundary condition that the NPs cannot overlap. Figure 6.5(a) shows an example of random configuration of nanoparticles in a 10×10 μm^2 simulation box.

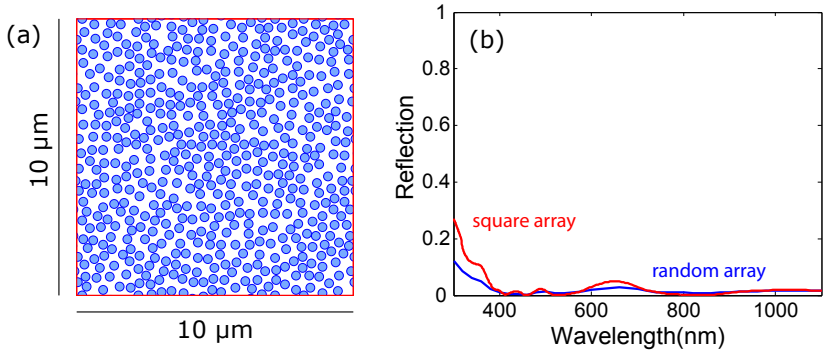

Figure 6.5: (a) Random configuration of NPs (blue dots) in a 10×10 μm^2 simulation box (red square). **(b)** Simulated reflection spectra for a periodic (red) and random (blue) array of Si NPs on a Si wafer. The two spectra overlap for large part of the spectral range considered here, suggesting that the individual scattering of the Mie resonators is dominant over the collective scattering from the grating.

Figure 6.5(b) shows the simulated reflectivity spectra for a periodic square array (red) and a random array (blue) of Si NPs with diameter 250 nm and height 150 nm. The total NP surface coverage is the same for the periodic and random geometries. The reflectivity spectrum of the periodic array is the same shown in Fig. 6.2(b). As can be seen in Fig. 6.5(b), the two reflectivity spectra overlap for large part of the spectral range 300-1100 nm. Both reflectivity spectra show the broad dips at wavelengths of 530 nm and 800 nm due to scattering of light through Mie resonances in the Si NPs. Overall, the reflectivity of a random array is slightly lower than that of the periodic array. This result suggests that the collective scattering from the grating formed by the Si NPs plays a very minor role in reducing the reflectivity of a bare Si substrate. The single particle Mie scattering mechanism dominates the scattering of light by the array of Si NPs.

6.6 Conclusion

Sub-wavelength resonant Mie scatterers at the surface of a Si wafer cause the reflection of light from the wafer to vanish. The resonant Mie modes have large scattering cross section, leading to strong interaction with the incident light. Coupling of these modes to the substrate leads to strong preferential forward scattering due to the high mode density in the high-index substrate. Full-wafer Si nanocylinder arrays were fabricated using a soft-imprint technique capable of large scale, high-fidelity surface patterning. Total reflectance spectroscopy shows an average reflectivity of only 1.3% over the 450-900 nm spectral range. The strongly reduced reflectivity is observed for a broad range of angles of incidence up to ±60°. Due to the monolithic nature of the Mie scatterers this novel anti-reflection concept is easily applicable to any high-index material. It can readily find application in solar cells, including thin-film designs on which the standard texturing cannot be applied.

Methods

Numerical calculations

The scattering cross section spectra and field distributions shown in Fig. 6.1 were calculated using Mie theory [83] (blue line in Fig. 6.1(a) and Figs. 6.1(b) and (e)) and finite-difference time-domain (FDTD) calculations (green and red lines in Fig. 6.1(a), and Figs. 6.1(c), (d), (f) and (g)). For a definition of scattering cross section please refer to Ref. [48], chapter 2. A commercial software package was used to perform FDTD calculations [90]. A simulation box size of 1×1×0.8 μm with perfectly matched layer (PML) conditions on every boundary was used. The light source was a broadband (300-1100 nm) plane wave, with normal incidence to the substrate. The mesh grid was set to 5 nm over the entire simulation volume, with a refinement (1 nm) over the volume occupied by the particle. A total-field scattered-field (TFSF) method was used to directly calculate the scattered power by means of frequency-domain transmission monitors positioned in the scattered field region. A two-dimensional frequency domain field monitor cross-cutting the particle in its center was used to calculate the electric field intensity distribution (as shown in Fig. 6.1(b)). FDTD simulations were also used to study the antireflection properties of Si NP arrays on a Si substrate (Fig. 6.2(a) and (b)). In this case, the box size was equal to p×p×0.6 μm, where p is the array pitch, and periodic boundary conditions (PBC) were used in the in-plane directions. The reflectivity spectra were directly calculated with a frequency-domain transmission monitor placed above the plane-wave source. Optical constants of Si and Si_3N_4 were taken from the literature [92].

Fabrication of Si nanopillar arrays

Substrate Conformal Imprint Lithography (SCIL) was used to fabricate large area Si NP arrays. This soft-imprint fabrication technique is capable of large scale, high-fidelity surface patterning and is fully compatible with standard techniques used in e.g. solar cell manufacturing. It uses a rubber (PDMS) stamp in which a pattern is molded from a master Si wafer that is patterned using optical interference lithography or electron beam lithography. The rubber stamp is used to replicate the patterns in a sol-gel layer spin-coated on the Si wafer. The patterned sol-gel layer is then used as a mask for a reactive ion etching process that results in the formation of Si nanocylinders in the Si wafer. For this work master template containing a 4×4 mm^2 array of 250 nm wide, 150 nm high Si nanopillars with array pitch of 450 nm was fabricated on a 4-inch Si(100) wafer using electron beam lithography and etching. The pattern in the sol-gel was transferred to the Si wafer with two-step reactive ion etching (RIE): a N_2 and CF_4 gas mixture was used to etch through the sol-gel layer and N_2 and Cl_2 gases were used to etch the Si wafer. The sol-gel etch mask was removed with diluted HF after which the samples were coated with Si_3N_4 layers of different thicknesses using low-pressure chemical vapor deposition (LPCVD) at 850°C. The 4-inch wafer shown in the photograph of Fig. 6.3 was fabricated with a similar process, where the master pillar pattern was made using optical interference lithography with a 266 nm wavelength laser.

Optical measurements

The total reflectivity spectra in Fig. 6.2(c,d) were measured in a Labsphere 4-inch integrating sphere, using a supercontinuum broadband light source (Fianium SC450-A, spectral range 0.45-2 μm). The beam spot on the sample was 1 mm in diameter. Light from the integrating spheres was collected with a multimode optical fiber and sent to a spectrometer, comprising a spectrograph (Acton, SpectraPro 300i) and a Si CCD array (Princeton Instruments). The data were confirmed by measurements in a PerkinElmer Lambda950 spectrophotometer, using a tungsten-halogen lamp and deuterium lamp as sources, a PM R6872 detector for the UV-VIS spectral range and a Peltier-cooled PbS detector for NIR range. Specular reflectivity for varying AOI (Fig. 6.4 and supplementary Fig. 6.11) was measured in a double rotation stage (Huber), where the sample was mounted in the inner stage and a power meter (Thorlabs, PM300) on the outer one. For the measurements at the 632 nm wavelength, a Helium-Neon laser source and a Thorlabs LPVIS 100 broadband linear polarizer were used (incident power on the sample: 4mW); an Argon-Kripton laser source and a ColorPol VIS500 linear polarizer (10mW on the sample) were used for the 514 nm wavelength; a diode laser source and a Thorlabs LPUV 050 polarizer (3mW on the sample) for the 405 nm wavelength. In all cases, the beam spot size on the sample was 1 mm in diameter.

Supplementary figures

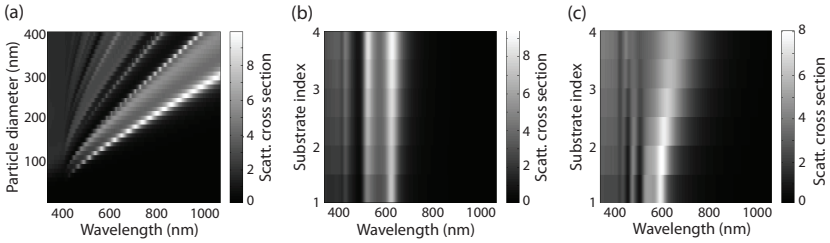

Figure 6.6: **(a)** Normalized scattering cross section (grey scale) as a function of wavelength (horizontal axis) and particle diameter (vertical axis) for a spherical particle in air. A redshift of all the Mie modes is observed as the particle size increases, as expected for a geometrical resonance in a cavity. **(b, c)** Normalized scattering cross section (gray scale) of a single Si nano-sphere **(b)** and nano-cylinder **(c)** on a substrate, as a function of wavelength (horizontal axis) and substrate refractive index (vertical axis). The Mie modes of a sphere do not shift or broaden as the substrate index is increased, due to the fact that light at resonance is confined inside the nano-sphere. For a cylindrical particle on a substrate a broadening of the resonance is observed as the substrate index is increased. This happens because the substrate introduces a loss channel for the light resonantly stored in the nanoparticle, both by radiative losses and near-field absorption. For the case of Si (n=3.5), the resonance is broadened over the entire range 500-800 nm.

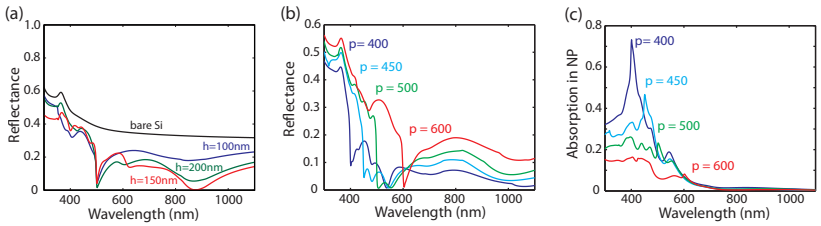

Figure 6.7: **(a)** Simulated reflectance spectra of a bare Si wafer (black), and Si NP arrays with 500 nm pitch, for cylinder heights of 100, 150 and 200 nm. Broad reflection dips are observed for wavelengths at which Mie resonances occur. The lowest reflectivity is found for a height of 150 nm. **(b)** Reflectance spectra of 250 nm wide, 150 nm high Si NP arrays for different array pitch. All reflectivity spectra show a sharp decrease in reflectivity at a wavelength equal to the array pitch, due to a Rayleigh anomaly from the grating formed by the regular array of nanoparticles. **(c)** Absorption spectra of Si NP arrays for different array pitch. Here, absorption is monitored that takes place in the Si NPs only. Clear peaks are observed at wavelengths equal to the pitch, due to the fact that the scattered light travels with an in-plane momentum (Rayleigh anomaly) and is thus more strongly absorbed in the Si NPs.

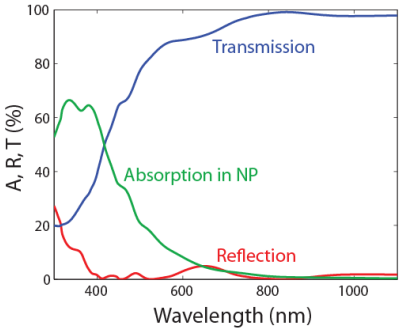

Figure 6.8: Transmission (blue), absorption in the NPs (green) and reflection (red) spectra for the optimized Si NP array (250 nm diameter, 150 nm height, 450 nm pitch). The first order Mie resonance of the NPs is at 850 nm. Interestingly, in the spectral range 700-1000 nm almost 100% transmission is observed and absorption is very low. This is due to the fact that NPs of such size have high albedo, i.e. they behave as pure scatterers.

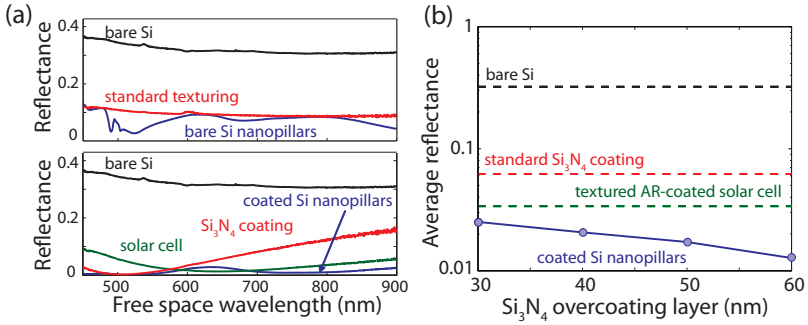

Figure 6.9: Comparison with standard antireflection coatings. **(a)** Top panel: reflectivity spectrum of a Si wafer with surface texture optimized for a solar cell (red) and that of an un-coated Si NP array (blue). The reflectivity from a bare Si wafer is also shown for reference (black). Patterning the surface of a Si wafer with Mie resonators yields a better AR effect than that of a standard surface texturing, over the entire 450-900 nm spectral range. The Mie scattering scheme can be applied to any (even thin film) substrates, whereas textures can only be applied in limited cases. Bottom panel: measured reflectivity spectra of a bare Si wafer (black), a Si wafer coated with a 60 nm thick standard Si_3N_4 AR coating (red), an optimized textured and Si_3N_4-coated solar cell (green) and an optimized coated Si NP array (blue). The coated Si NP array AR coating outperforms both the 60 nm Si_3N_4 AR coating and the solar cell. **(b)** Average reflectivity, weighted with the AM1.5 solar spectrum in the 450-900 nm range, for a bare Si substrate (black, 32%), a standard Si_3N_4 coating (red, 6.25%), a textured and AR-coated solar cell (green, 3.38%) and a Si NP array coated with a Si_3N_4 layer with variable thickness (blue). The average reflectivity of the optimal configuration is 1.3%.

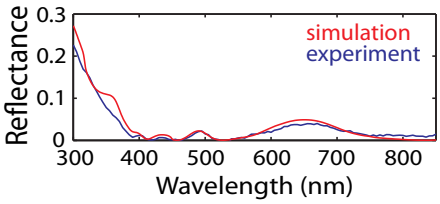

Figure 6.10: Measured reflectivity for the optimized Si_3N_4 coated Si NP array (red), extending well into the UV, compared with the simulated reflectivity (blue). Excellent agreement between the measurement and the simulation is observed.

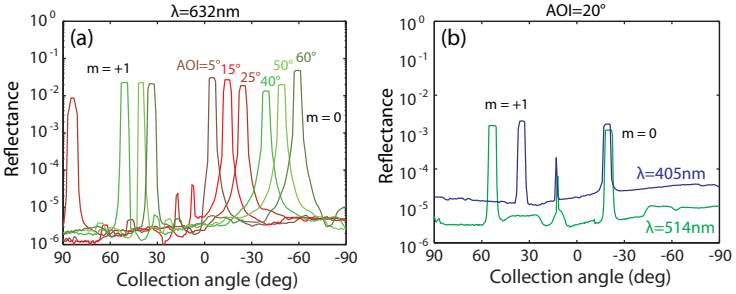

Figure 6.11: Diffraction effects. **(a)** Measured reflectance as a function of collection angle for for angles of incidence of 5°, 15°, 25°, 40°, 50° and 60° and wavelength of 632 nm. As can be seen, for AOI below 25° only the m = 0 order (specular reflectivity) appears in the collection plane. For incident angles larger than 25° a contribution from m = +1 order is also present with intensity comparable of the m = 0 order. For all AOI, the collection angles at which the m = +1 order appears fulfill the grating relation: $\sin(\theta_i) + \sin(\theta_c) = \frac{m\lambda}{p}$, where θ_i is the AOI, θ_c is the collection angle, m the grating order, λ the wavelength and p the grating pitch. The reflectivity of the diffraction peaks varies between 1 and 5%. **(b)** Reflectivity as a function of collection angle for wavelengths of 405 nm (blue) and 514 nm (green), for a fixed AOI of 20°. Here, the m=0 and m = +1 diffraction peaks have intensities in the range 0.01-0.3%. The reflectance due to diffraction from the grating formed by the SiNPs is small and it thus not significantly affect the AR properties of the SiNP arrays. Diffraction losses can be avoided by using a random configuration of Si NPs.

7

Modeling of light trapping in thin crystalline Si solar cells using surface Mie scatterers

We systematically study with numerical simulations the absorption of light into thin (1-100 μm) crystalline Si solar cells patterned with Si nanocylinder arrays on top of the cell. We then use an analytical model to calculate the solar cell efficiency, based on the simulated absorption spectra. Using realistic values for bulk and surface recombination rates we find that a 20-μm-thick Si solar cell with 21.5% efficiency can be made, by using the Si nanocylinder Mie coating.

7.1 Introduction

Crystalline Si (c-Si) is currently the most widely used semiconductor for photovoltaic applications. Despite continued technological developments that bring down the production costs of c-Si solar cells, the intrinsic Si material costs in these cells still remains high. For this reason, making thinner c-Si solar cells in order to use less of this expensive material continues to be a main driving force for the photovoltaic research community. Recent technological advances have lead to the fabrication of thin-film c-Si solar cells on glass substrates by laser crystallization [133], liquid phase crystallization [134], and layer transfer [135, 136]. However, thinner c-Si solar cells do not fully absorb the incoming light, especially in the near-bandgap spectral range where the absorption length of Si exceeds the

thickness of the cell. Light trapping is thus needed in order to achieve complete absorption of light in the cell.

Standard c-Si solar cells usually have a thickness of around 180 μm. At the front side they are covered with a pyramidal light trapping texture coated with a 80-nm-thick Si_3N_4 anti-reflection layer [2]. The typical feature size of the texturing is in the range 5-10 μm [115]. Therefore, it is impossible to apply this light trapping texture to thinner cells with thicknesses in the micron range. Recently, metal and dielectric nanostructures have been considered as light-trapping coatings for ultrathin solar cells [40, 51, 53–55, 85, 98]. We have shown that an array of dielectric nanoparticles placed on top of a Si wafer acts as an efficient anti-reflection coating [137]. This is due to the preferential scattering of light towards the high index substrate from leaky Mie resonances that are excited in the nanoparticles [83, 138]. In particular, we have shown that an optimized array of Si nanocylinders (NCs) yields broadband and omnidirectional ultra-low reflectivity, reducing the reflection of a Si wafer to an average value as small as 1.3% [137].

In this Chapter, we investigate the potential of these Mie resonator coatings for light-trapping in thin (1-100 μm) Si solar cells. Using numerical methods, we systematically study light absorption into thin Si slabs patterned with dielectric nanoparticle arrays with different geometries on top of the slab. We use Finite Difference Time Domain (FDTD) simulations (employing periodic boundary conditions) to calculate light absorption of the c-Si slabs and compare it to that of a flat Si slab with a standard Si_3N_4 antireflection coating. An analytical model is then used to calculate, based on the simulated absorption spectra, the photocurrent, open circuit voltage and efficiency of a c-Si solar cell with a Mie scattering surface coating and a metallic backcontact. The model includes Shockley-Read-Hall bulk carrier recombination, surface recombination, as well as radiative and Auger recombination. Using realistic values for the recombination rates and a perfectly reflecting back contact we find that an efficiency as high as 21.5% can be achieved for a 20-μm-thick cell with a Si NC Mie coating. This is a significant improvement compared to the efficiency that we find for a planar c-Si cell with a standard Si_3N_4 anti-reflection coating of the same thickness (17.5%). We also investigate the effect of an absorbing Ag back contact on the efficiency.

7.2 Simulation results

We use FDTD simulations [90] to calculate the absorption of light in thin Si slabs covered with square arrays of Si NC Mie scatterers, for wavelengths in the range 300-1150 nm. The Si NC coating is comprised of 250 nm wide, 150 nm high Si cylinders in an array with 450 nm pitch, conformally coated with a 50-nm-thick Si_3N_4 layer. These parameters are optimized for minimizing the reflection of a bulk Si wafer with a Si NC coating [137]. A perfect reflector is applied at the back of the Si slab and periodic boundary conditions are used. The absorption in both the Si slab and the Si NCs is calculated, as well as the reflection. Figure 7.1 shows the absorption per

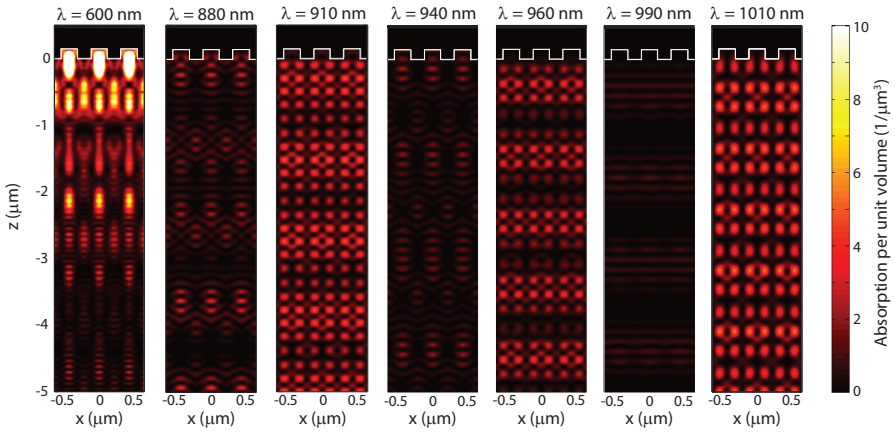

Figure 7.1: Numerically calculated absorption per unit volume (color scale) in a vertical cross section of a 5-μm-thick Si slab with the Si NC Mie coating. Each panel represents a different wavelength and shows 3 horizontal unit cells. The absorption of light takes place according to complicated patterns determined by interference of the light scattered by the NCs.

unit volume (color scale) in a vertical cross section of a 5-μm-thick Si slab coated with the Si NC Mie coating. Each panel shows the absorption profile for a different wavelength, in the range λ = 600-1010 nm. The white contours in the top part of each plot indicate the position of the Si nano-cylinders; 3 horizontal unit cells are shown in each panel. As can be seen, the absorption profiles inside the thin Si slab have complex patterns which vary for different wavelengths. The patterns result from interference of light scattered by the NC array in combination with reflection from the back surface. Fig. 7.1(a) shows that in the visible spectral range (e.g., λ = 600 nm) the absorption of light occurs mostly inside the Si NC and in the top part of the Si slab. The absorption patterns in the near-infrared spectral range are strongly dependent on the wavelength. For wavelengths of 880 nm, 940 nm and 990 nm (Fig. 7.1(b), (d) and (f)) the absorption is rather weak, whereas for wavelengths of 910 nm, 960 nm and 1010 nm (Fig. 7.1(c), (e) and (g)) the absorption profiles show bright absorption spots with a double periodicity with respect to array pitch. We attribute these absorption profiles to the complex interplay of light coupled to Fabry-Perot and waveguide modes in the thin slab [139]. The plots in Fig. 7.1 can be used to calculate the total absorption in the Si slab and in the Si NCs, by integrating the absorption per unit volume over the volume of the slab and the NCs, respectively.

Figure 7.2 shows the combined absorption in Si slab and Si NCs as a function of wavelength for the patterned slab (red), compared to that for a flat Si slab with a standard 80 nm Si_3N_4 coating (blue). Data are shown for 5-μm-thick (a) and 20-μm-thick (b) Si slabs. The graphs show that absorption is enhanced over the entire

300-1100 nm spectral range by the presence of the Mie nano-scatterers on the front surface. This can be explained by two main mechanisms. First, the Mie scatterers provide an antireflection effect, due to the preferential forward scattering towards the Si slab, as we demonstrated earlier for thick Si wafers [137]. This effect improves the absorption over a broad spectral range from the ultraviolet to the near-infrared. Second, the array of Mie scatterers couples the incoming light to waveguide modes in the thin Si slab. This effect is responsible for the absorption enhancement in the near-infrared spectral range. The main sharp peaks at 910, 960 and 1100 nm for the 5-μm-thick slab with the Mie coating (red, see also absorption profiles in Fig. 7.1) are ascribed to coupling to Fabry-Perot and waveguide modes by the Mie resonances in the Si NC [139]. These main peaks are not observed for the flat reference. The smaller oscillations in the absorption spectrum of both the Mie-coated sample and the flat slab (blue) are due to Fabry-Perot interferences in the Si/Si_3N_4 layer stack. For the 20-μm-thick slab a broad enhancement is observed above λ=900 nm, on top of the Fabry-Perot resonances, which we ascribe to coupling to a broad continuum of waveguide modes; for this large thickness individual waveguide-coupling peaks cannot be spectrally separated due to the high density of modes in the waveguide.

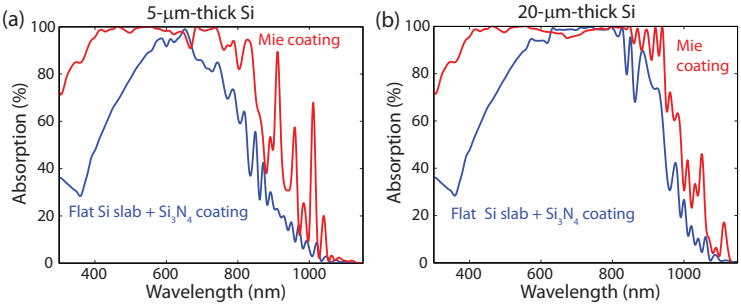

Figure 7.2: Simulated absorption spectra for a 5-μm-thick **(a)** and a 20-μm-thick **(b)** Si slab with (red) and without (blue) a surface coating of Si nanocylinders. Absorption in the particles and in the Si slab are both taken into account. The flat and patterned geometries are coated with 80 nm and 50 nm thick Si_3N_4 coatings, respectively. The absorption of the slab with the Mie coating is larger than that of a standard coating over the entire spectral range. This is due to an improved anti-reflection effect and to light coupling to waveguide modes of the thin slab.

7.3 Solar cell modeling

The absorption data shown in Fig. 7.2 can be used to calculate the total photocurrent generated in the thin Si cell. First, a uniform photocarrier generation rate is assumed throughout the thickness of the Si slab. In practice, this means that the absorption profiles shown in Fig. 7.1 are averaged out over the volume of the slab.

This is a valid assumption for crystalline Si, for which the carrier diffusion length is larger than the thickness of the solar cell considered in this work. The generation rate G per unit volume can be calculated by:

$$G = \frac{1}{t}\int_{\lambda} \frac{\lambda}{hc} I(\lambda) A(\lambda) d\lambda \tag{7.1}$$

where t is the Si slab thickness, $I(\lambda)$ is the AM1.5 solar power spectrum, $A(\lambda)$ is the simulated absorption spectrum, h is Planck's constant and c the speed of light. Assuming the slab is made of n-type Si, the generation rate G is then used in the diffusion equation for holes in the quasi-neutral region [2]:

$$D_h \frac{d^2\Delta p}{dx^2} = \frac{\Delta p}{\tau_b} - G \tag{7.2}$$

where D_h is the minority carrier diffusion constant, Δp is the excess hole concentration, τ_b is the bulk lifetime for holes and x the position across the thickness of the cell. Equation 7.2 can be solved assuming the boundary conditions:

$$\Delta p|_{x=0} = \frac{n_i^2}{N_D}\left(e^{\frac{qV}{kT}} - 1\right) \tag{7.3}$$

and

$$\frac{d\Delta p}{dx}|_{x=t} = -\frac{S}{D_h}\Delta p(t) \tag{7.4}$$

where N_D is the doping level, V the voltage across the cell, n_i is the intrinsic carrier concentration, and S the back surface recombination rate. An infinitely thin p-n junction is assumed at the front surface (x=0). Realistic devices that come close to this approximation are, e.g., heterojunction a-Si/c-Si solar cells, where the a-Si emitter is only a few nanometers thick [140]. Solving equation 7.2 for Δp and calculating the current density as $J = -qD_h\frac{d\Delta p}{dx}$ yields the solution for $J(V)$ below:

$$J = j_0\left(e^{\frac{qV}{kT}} - 1\right) - qLG\left(\frac{L}{L_{j0}} - \frac{LS}{F}\right) \tag{7.5}$$

with:

$$L = \sqrt{\tau_b D_h}$$
$$L_{j0} = L\frac{D_h\cosh(x) + SL\sinh(x)}{SL\cosh(x) + D_h\sinh(x)}$$
$$j_0 = \frac{qD_h n_i^2}{L_{j0}N_D}$$
$$F = D_h\cosh(x) + SL\sinh(x)$$

which is in agreement with Ref. [141], for the case of uniform carrier generation rate. Equation 7.5 represents the J-V characteristic of the solar cell based on the

assumptions above. The short-circuit current density J_{SC}, the open-circuit voltage V_{OC}, the fill factor and efficiency η are easily calculated from this relation. The free parameters in the model are the bulk lifetime τ_b, the surface recombination velocity S and doping level N_D. The bulk lifetime τ_b can be written as:

$$\frac{1}{\tau_b} = \frac{1}{\tau_{SRH}} + \frac{1}{\tau_{Auger}} + \frac{1}{\tau_{rad}} \tag{7.6}$$

where τ_{SRH} lifetime representing Shockley-Read-Hall bulk recombination, τ_{Auger} is the lifetime representing Auger recombination and τ_{rad} is the radiative recombination lifetime. For n-type Si, a semi-empirical expression for equation 7.6 is [142]:

$$\frac{1}{\tau_b} = \frac{1}{\tau_{SRH}} + (N_D + \Delta n)\left(1.8 \times 10^{-24} N_D + 3 \times 10^{-27} \Delta n + 9.5 \times 10^{-15}\right) \tag{7.7}$$

where N_D is expressed in units of cm^{-3}, and Δn is the injected carrier concentration in units of cm^{-3}, which is directly related to the open circuit voltage V_{OC}, as shown in Ref. [143]. The set of equations (7.5-7.7) can be solved recursively. In the following, we assume a fixed $N_D = 10^{16}$ cm^{-3}, and τ_{SRH} and S are varied.

Figure 7.3 shows calculations of J_{SC} (panels a, d, g), V_{OC} (b, e, h) and efficiency (c, f, i) as a function of Si slab thickness. The top row assumes τ_{SRH} = 1 ms and S = 10 cm/s (good bulk material quality and surface passivation), the middle row τ_{SRH} = 1 ms and S = 100 cm/s (good material quality and poor surface passivation) and the bottom row τ_{SRH} = 0.1 ms and S = 10 cm/s (poor material quality and good surface passivation). Each panel shows data for a Si slab with a standard 80 nm Si_3N_4 coating (blue) and for a Si slab with a Mie coating (red, same Si NC geometry as in Fig. 7.2). The latter is calculated considering absorption spectra that include both the absorption in the Si slab and absorption in the Si NCs at the surface. For reference, Fig. 7.3 also shows data for a Si slab with perfect anti-reflection coating and a perfect Lambertian light trapping surface where the (geometrical) path length enhancement at long wavelengths equals $4n^2$, with n the refractive index of Si (black dashed lines) [42, 116].

Figure 7.3(a) shows that the photocurrent is strongly enhanced for all thicknesses due to the surface Mie scatterers. The photocurrent enhancement is more significant for thicknesses below 20 μm where the Mie scatterers provide both an antireflection effect and strong light trapping due to coupling to waveguide modes in the thin Si slab. For a 1-μm-thick cell the photocurrent is enhanced by as much as 75% due to the Si Mie coating, for a large part due to light trapping. For a 20-μm-thick cell, a photocurrent enhancement of 20% is observed. For thicknesses above 20 μm, the photocurrent enhancement converges to the same value for all cell thickness, as the light trapping effect becomes less relevant with respect to the anti-reflection effect. The dash-dotted lines in Fig. 7.3(a) represent the photocurrents achieved in the case of an infinitely long carrier diffusion length (i.e., when all the photogenerated carriers are extracted from the cell). As can be noticed, these photocurrents diverge from the actual photocurrents (solid lines) only for cell thicknesses above 50 μm, i.e. for thicknesses comparable with the minority

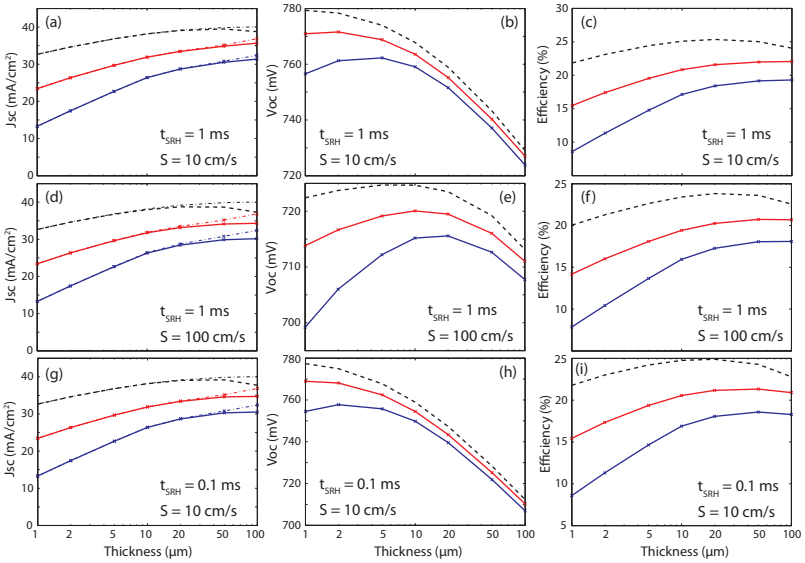

Figure 7.3: Simulated short-circuit current density **(a, d, g)**, open circuit voltage **(b, e, h)** and efficiency **(c, f, i)** as a function of Si layer thickness. Top panels assume τ_{SRH} = 1 ms and S = 10 cm/s, center panels τ_{SRH} = 1 ms and S = 100 cm/s and bottom panels τ_{SRH} = 0.1 ms and S = 10 cm/s. In each panel, data for a slab with Mie scatterers (red) and a flat Si slab with standard Si_3N_4 coating (blue) are shown. The data for an ideal cell without reflection and with light trapping according to the geometrical $4n^2$ limit is shown for reference (black dashed lines).

carrier diffusion length. The graph of Fig. 7.3(a) also shows that the photocurrents achieved with a Mie coating are roughly halfway between those achieved with a standard flat coating, and those achieved in the $4n^2$ light trapping limit. Similar results are observed in case of high surface recombination velocity S (Fig. 7.3(d)) and short bulk lifetime (Fig. 7.3(g)). In both these cases, the photocurrent for cells thicker than 20 μm is reduced compared to the case in Fig. 7.3(a), due to reduced carrier collection for large cell thickness. Figures 7.3(b,e,h) show that for cells with Mie coating V_{OC} is always higher than for a flat cell with a standard Si_3N_4 coating. This is a direct consequence of the higher photocurrent for the Mie-coated cell, as seen in Figs. 7.3(a,d,g). For the Mie-coated cell with low surface and bulk recombination rates (Fig. 7.3(b)) V_{OC} increases for decreasing cell thickness. This is due to the reduced effect of bulk recombination as the cell thickness. For larger surface recombination velocities (Fig. 7.3(e)), V_{OC} decreases with decreasing thickness, as surface recombination then dominates over bulk recombination. In this case an optimum V_{OC} is found for a thickness of 10 μm for the cell with Mie coating, and 20 μm for the cell with standard Si_3N_4 coating. For cells with strong bulk recombination (Fig. 7.3(h)), a lower V_{OC} is observed for all thicknesses. However, in this case the effect is stronger for thicker cells, where the bulk material quality plays a more

important role due to the larger bulk volume.

Finally, Figs. 7.3(c,f,i) show a strong efficiency enhancement for Mie-coated cells. This is a direct consequence of the photocurrent enhancement due to the antireflection and light trapping effects provided by the Mie scatterers and the enhanced voltage. In particular, for a 20-μm-thick cell with low bulk and surface recombination rates an efficiency as high as 21.5% can be achieved, compared to an efficiency of 17.5% for a flat cell. For reference, a cell operating in the $4n^2$ light trapping limit would yield an efficiency of 25.3%. The importance of the result for the Mie light-trapping coating relies in the fact that standard random textures commonly used for wafer-based c-Si solar cells cannot be applied to 20-μm-thick cells, as the feature size is comparable to the thickness of the cell. Interestingly, the graph shows that a 5-μm-thick cell with Mie scatterers yields the same efficiency as a flat 100-μm-thick cell with standard Si_3N_4 coating. The Mie scatterers thus allow reducing the cell thickness by a factor of 20, maintaining the same power conversion efficiency. Similar results are observed for high surface recombination velocities S (Fig. 7.3(f)) and bulk lifetimes (Fig. 7.3(i)). In both cases, lower efficiencies are observed than for the cells with lower recombination rates, due the lower photocurrents and voltages.

To further investigate the crucial role of the Shockley-Read-Hall lifetime τ_{SRH} and of the surface recombination velocities S, Fig. 7.4 shows the calculated solar cell efficiency (color lines) as a function of τ_{SRH} (vertical axis) and S (horizontal axis), for a 5-μm-thick cell (a) and a 20-μm-thick cell (b) with a Si NC Mie coating. For a 5-μm-thick cell (a), efficiencies range from 19.5% for τ_{SRH} = 1 ms and S =

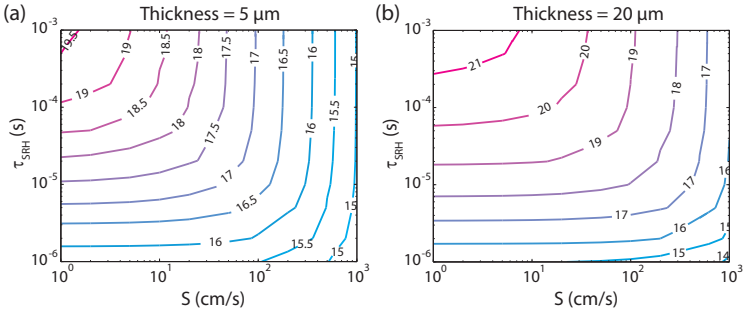

Figure 7.4: Efficiency (colors) as a function of the Shockley-Read-Hall lifetime τ_{SRH} (vertical axis) and the surface recombination velocity S, for a 5-μm-thick cell (a) and a 20-μm-thick cell (b) with Mie coating. The efficiency of a 5-μm-thick cell is more sensitive to variations in S, whereas the 20-μm-thick cell is more sensitive to variations in τ_{SRH}. For thin cells, efficiencies range from 19.5% to 15%; for the thick cell from 21.5% to 14%.

1 cm/s, down to 15% for τ_{SRH} = 1 μs and S = 1000 cm/s. Similarly, for a 20-μm-thick cell (a), efficiencies range from 21.5% to 14%. A comparison of the two graphs shows that a 20-μm-thick cell is more sensitive to variations of τ_{SRH} than a 5-μm-thick cell, due to the larger volume. Similarly, a 5-μm-thick cell is more sensitive to

variations of S than a 20-μm-thick cell, due to the larger surface-to-volume ratio.

In the analysis conducted so far, a perfect back reflector was considered. Simulations were also used for Si slabs with a back reflector with 97% reflectivity. Figure 7.5 shows the calculated efficiency as a function of thickness, for a Si slab with perfect back reflector (solid), and with a back reflector with 97% reflectivity (dashed). Data are shown for a Si slab with flat Si_3N_4 coating (blue lines) and for a Si slab with Mie coating (red). Similarly to Fig. 7.3(c), we assume τ_{SRH} = 1 ms and S = 10 cm/s. The graph shows a drop in efficiency of about 0.5% (absolute) for a

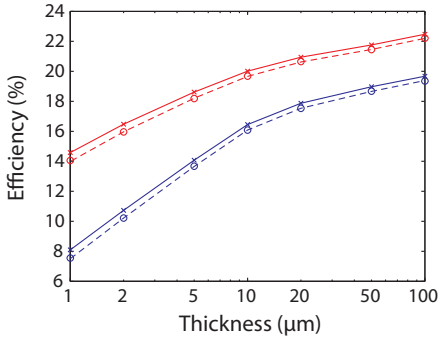

Figure 7.5: Efficiency as function of solar cell thickness, for a Si slab with the Mie coating (red) and with a standard Si_3N_4 coating (blue). Solid lines represent the case of a perfect back reflector and dashed lines are for a back reflector with 97% reflectivity. The efficiency of a 20-μm-thick cell is reduced by 0.5% (absolute) due to the absorption in the back reflector.

20-μm-thick cell with Mie coating, when a realistic back contact is used instead of an ideal back reflector; the efficiency of the 20-μm-thick Mie-coated cell then drops to 21%. Similar losses are observed for cells with a standard Si_3N_4 coating.

7.4 Light trapping with TiO_2 Mie scatterers

The analysis conducted so far shows that Si NC Mie scatterers serve as excellent light trapping coatings for thin c-Si solar cells. From an optical point of view, Si is the best material for the Mie coating, as its refractive index is large (n~3.5) and matched to that of the Si substrate. Furthermore, Si Mie coatings can be easily integrated on top of a c-Si wafer by reactive ion etching, as shown in Chapters 2 and 6. However, a Si Mie coating increases the surface area of the cell and may be difficult to passivate, causing enhanced recombination of electrical carriers. As will be shown in Chapter 9, an interesting alternative to the Si-based Mie coating is a TiO_2-based Mie coating [45]. In fact, TiO_2 has a relatively high index (n~2.2-2.5) and low absorption. The antireflection and surface passivation properties of the TiO_2 Mie coating are studied in detail in Chapter 9. Here, we present the same

analysis done in the present Chapter for a Si NC array, for an array of TiO_2 Mie scatters. As before, we assume τ_{SRH} = 1 ms and S = 10 cm/s.

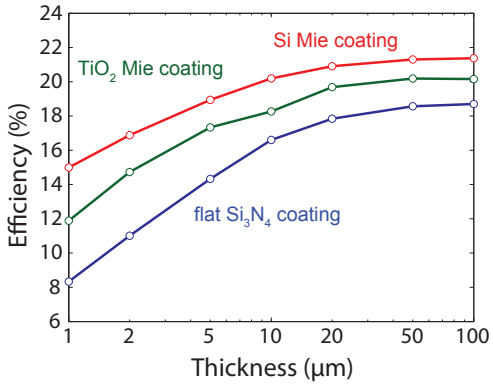

Figure 7.6: Efficiency of a Si slab with a standard 80 nm Si_3N_4 coating (blue), with a Si Mie coating (red) and with a TiO_2 Mie coating (green), as a function of the slab thickness.

Figure 7.6 shows the calculated efficiency as a function of thickness for a Si slab with a standard 80 nm Si_3N_4 coating (blue), with a Si Mie coating (red) and with a TiO_2 Mie coating (green). The efficiency of the Si slab with the Si Mie coating was calculated considering absorption spectra that include both the absorption in the Si slab and absorption in the Si NCs at the surface. The efficiency of the Si slab with the TiO_2 Mie coating was calculated taking into account absorption in the Si slab. As can be seen, the TiO_2 Mie coating yields a higher efficiency than the flat Si_3N_4 coating, but lower than the Si Mie coating. This is due to two main reasons: parasitic absorption in the TiO_2 NCs (see Chapter 9) and less efficient scattering through Mie resonances due to the lower index of TiO_2 with respect to Si. The TiO_2 Mie coating allows designing 20-μm-thick Si solar cells with 19.8% efficiency, compared with 21.5% for a Si Mie coating. Despite the lower performance, a TiO_2 Mie coating has the advantage that it can be easily integrated with a thin passivation layer, yielding very low surface recombination velocity, as will be shown in Chapter 9.

7.5 Light trapping with random and periodic arrays of Mie scatterers

Finally, we compare the light trapping properties of random and periodic arrays of Si Mie scatterers. In Chapter 6 we have shown that random and periodic Si NC arrays on a thick Si wafer yield similar antireflection properties. This is due to the fact that for a thick substrate, the individual scattering of single Si NCs dominates over the collective scattering of the grating. For thinner cells however, the scattering

from grating orders of the NC array is important for coupling to waveguide modes of the thin slab [65, 139, 144]. Usually, only a limited number of modes in the slab can be populated by scattering from grating orders, i.e. those modes whose parallel momentum matches the spatial frequencies of the grating [145]. By randomizing the NC array, we broaden the spectral spatial frequencies of the array, and thus we can couple to a larger number of modes in the slab.

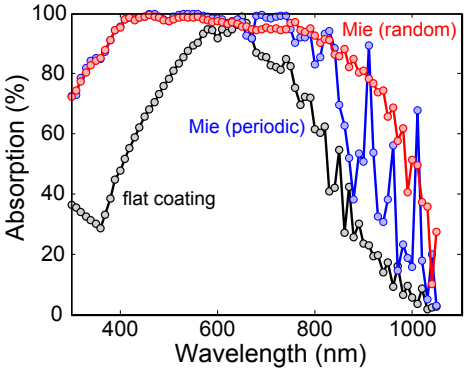

Figure 7.7: Simulated absorption spectra for a 5-μm-thick Si slab coated with a flat Si_3N_4 coating (black), with a periodic array of Si Mie scatterers (blue) and with a random array of Si Mie scatterers (red).

Figure 7.7 shows the simulated absorption spectra for a 5-μm-thick Si slab coated with a flat Si_3N_4 coating (black), with a periodic array of Si Mie scatterers (blue) and with a random array of Si Mie scatterers (red). Both periodic and random configurations yield larger absorption for the entire spectral range 300-1050 nm than for a flat cell. The curves for the periodic and random arrays overlap for wavelengths shorter than 700 nm. In this spectral range, the absorption is enhanced mostly due to an antireflection effect (see Chapter 6). However, in the near-infrared spectral range, the periodic and random arrays show different behavior. The periodic array shows sharp peaks, which are ascribed to coupling to waveguide modes in the thin slab, as discussed above. The random array shows a broadband enhancement over the entire near-infrared spectrum. We attribute this to the fact that the random array couples light to a larger number of modes in the slab, due to its broader spectrum of spatial frequencies. Further studies are needed to obtain deeper understanding of the coupling of resonant Mie modes to waveguide modes. Overall, the AM1.5-weighed average absorption of the random array is 77% compared to 72% of the periodic array. In both cases, a significant absorption enhancement is observed with respect to the case of a flat Si_3N_4 coating (66%).

7.6 Conclusion

Using numerical simulations, we have shown that strongly reduced reflection and enhanced light trapping can be achieved in thin (1-100 μm) c-Si solar cells covered at the front surface with an array of Mie scattering Si nanocylinders, and coated with a Si_3N_4 anti-reflection layer. For thin Si slabs near-infrared light trapping due to preferential scattering of light by the Mie scatterers into guided modes of the Si slab is directly observed from spectral peaks in the photocurrent. A strong increase in photocurrent is observed due to the Mie scatterers for all thicknesses in the range 1-100 μm. For thin cells, a strong increase in open circuit voltage is observed. For cells with low bulk and surface recombination (τ_{SRH} = 1 ms and S = 10 cm/s) a cell efficiency of 21.5% can be achieved for a 20-μm-thick Mie coated cell, compared to 17.5% for a flat cell. Silicon Mie scatterers are thus good candidates to substitute standard light trapping techniques, such as pyramidal textures, that cannot be applied on thin solar cells. Our study opens new perspectives for designing high-efficiency thin-film c-Si solar cells.

8

Experimental demonstration of light trapping beyond the $4n^2$ limit in thin Si slabs using resonant surface Si Mie scatterers

We experimentally demonstrate light trapping in thin Si slabs, by using resonant surface Si Mie nanocylinders. Thin (1-4 μm) Si slabs were grown by chemical vapor deposition (CVD) on glass substrates. The Si Mie coating was fabricated by substrate conformal imprint lithography (SCIL) and reactive ion etching (RIE). We measure the absorption spectra of the thin Si slabs by using total reflection and transmission spectroscopy. Strong absorption enhancement is observed over the entire 420-970 nm spectral range, due to light trapping by the Mie scattering coating. For a 1-μm-thick slab, we demonstrate optical path length enhancement near the Si bandgap up to a factor of 65, well beyond the geometrical Lambertian $4n^2$ limit.

8.1 Introduction

Thin-film crystalline Si cells have a high potential to reduce the cost of photovoltaic energy, due to the reduction of material costs compared to bulk wafers. In addition, thinner cells allow achieving higher open circuit voltages, due to reduced bulk recombination. However, efficient light trapping schemes are needed to absorb the full solar spectrum in a thin-film cell [40]. As shown in Chapter 7, using an array

of Si Mie scatterers at the surface provides a very good light-trapping scheme for Si solar cells with thickness in the range 1-100 μm. As we have shown using numerical simulations of the optical absorption in thin Si cells coated with Mie scatterers, efficiencies above 20% can be achieved for Si layers of 10 μm.

In this Chapter we experimentally study light trapping in thin crystalline Si slabs grown by chemical vapor deposition (CVD) on glass substrates. We perform total reflection and transmission spectroscopy to measure the absorption spectra of the thin Si layers. The absorption spectra are used to estimate the light trapping effect by the Si Mie coating, which is then compared to the Lambertian $4n^2$ light trapping limit [41, 42]. We find that for a 1-μm-thick Si slab the Si Mie coating provides light trapping beyond the $4n^2$ limit for a spectral range close to the silicon bandgap.

8.2 Experimental results

We fabricate thin polycrystalline Si layers on top of a 2×1 cm^2 glass substrate by means of CVD. Three series of samples were fabricated, with thicknesses of 1 μm, 2 μm and 4 μm, respectively. The growth rate was ~2 nm/s, and the surface roughness of the deposited Si layers is 1.3 nm as measured using profilometry. Ellipsometry shows that the optical constants of the layers are very close to those of single-crystalline Si. Arrays of Si nanocylinders (NCs) were made at the surface using substrate conformal imprint lithography (SCIL) and reactive ion etching (RIE), in the same way as outlined in Chapter 2.

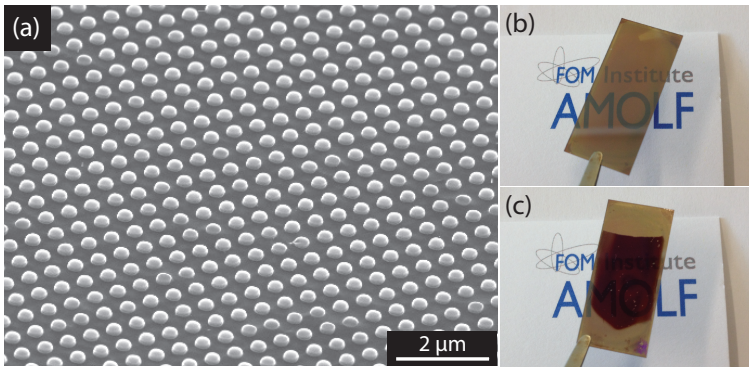

Figure 8.1: **(a)** SEM image of an array of Si NCs in a 1 μm thick layer on glass. **(b)** Photograph of a 1-μm-thick uncoated Si slab on a glass substrate and **(c)** of a 1-μm-thick Si slab on glass coated with the Si Mie NC array.

Figure 8.1(a) shows a scanning electron microscope (SEM) image of the Si NC array etched into a 1-μm-thick Si layer. The Si NCs have height of 150 nm, diameter of 250 nm and are placed in a square array with a pitch of 450 nm. Figures 1(b) and (c) show photographs of a 1-μm-thick Si layer on glass with and without the Si Mie

coating, respectively. As can be seen, the unpatterned Si layer (b) is semitransparent for light in the red part of the spectrum. In contrast, the Si slab coated with Si NCs appears opaque, due to increased light absorption.

The light trapping properties were studied by means of total reflection and total transmission spectroscopy in a Labsphere 4"-diameter integrating sphere, using a supercontinuum broadband light source (Fianium SC400-A, spectral range 0.40 - 2 μm). The diameter of the normal-incidence beam spot on the sample was ~1 mm. Light from the integrating sphere was collected with a multimode optical fiber and sent to a spectrometer (Acton, SpectraPro 300i), equipped with a Si CCD detector. Measurements were taken up to a wavelength of 970 nm, limited by the sensitivity of the detector.

Figure 8.2(a) shows the measured reflectivity spectra of a flat uncoated Si(100) wafer (black), a flat uncoated 1-μm-thick Si slab on glass (blue) and the same slab coated with Si NCs (red).

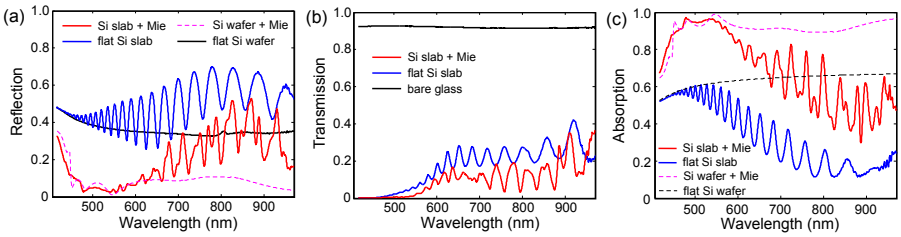

Figure 8.2: **(a)** Reflection, **(b)** transmission and **(c)** absorption spectra of a 1-μm-thick Si slab on glass for an uncoated slab (blue) and a slab coated with a Si NC array (red). Panel **(a)** also shows the measured reflection spectrum of a thick Si wafer (black) and the simulated reflection spectrum of a semi-infinite Si substrate with a Si Mie coating (dashed purple line). Panel **(b)** also shows the transmission spectrum of a bare glass slide (black) for reference. Panel **(c)** also shows the spectrum of light that is absorbed into a semi-infinite Si substrate covered with the Si Mie coating (dashed purple line) and in a flat uncoated semi-infinite Si substrate (dashed black).

The reflectivity of a flat Si slab shows clear oscillations due to Fabry-Perot interference in the slab. The overall reflection is larger than that of a thick Si wafer (black), due to the contribution of reflection from the Si-glass interface. As can be seen, the Si Mie coating reduces the reflectivity of a flat Si slab over the entire spectral range from 420 nm to 970 nm. Fabry-Perot oscillations are still visible in the reflectivity spectrum. In addition, features are observable that are spectrally narrower than the Fabry-Perot oscillations. We ascribe these features to coupling to waveguide modes in the thin slab (see also Chapter 7). Overall, the AM1.5-weighed average reflectivity of a 1-μm-thick Si slab is reduced from 48.4% to 17.7% by covering the slab surface with a Si NC array.

Figure 8.2(a) also shows the simulated reflectivity of a Si NC array on top of a semi-infinite Si substrate (dashed purple line). A very good spectral match is observed between this curve and the reflectivity of the flat slab in the range 420-600

nm. This means that the reduction in reflectivity in this spectral range is only due to the antireflection effect of the Si Mie coating (similar to what is shown in Chapter 6). No additional light trapping effect can be observed in this spectral range from the reflectivity spectrum, as nearly all light is absorbed by the 1-μm-thick Si slab in a single or double pass through it. For the spectral range 600-970 nm, light is not fully absorbed by the thin slab, and thus the measured reflectivity of the thin slab is larger than that of a semi-infinite substrate.

Figure 8.2(b) shows the transmission spectra of a glass substrate (black), a flat uncoated 1-μm-thick Si slab on glass (blue) and of the same slab coated with Si NCs (red). The transmission of a glass substrate amounts to ~92% over the entire spectral range, due to the ~4% reflectivity on the two glass-air interfaces. The transmission spectrum of a flat Si slab shows Fabry-Perot oscillations as in Fig. 8.2(a). The transmission is reduced over the entire spectral range by applying the Si Mie coating. This is due to the fact that light is scattered by the Mie NCs over a certain angular range, and thus the optical path length in the Si slab is enhanced. This yields higher absorption in the layer, and thus a lower transmission.

From the reflection (R) and transmission (T) spectra we can calculate the absorption as 1-R-T. The result is shown in Fig. 8.2(c), for a 1-μm-thick uncoated Si slab (blue) and for the same Si slab with the Si Mie coating (red). Note that as the Si NCs are etched into the 1 μm Si slab, the actual thickness of the slab with Si Mie coating is actually smaller than that of the flat slab (the effective thickness is 850 nm). Despite this thickness difference, the Si slab with Mie coating shows higher absorption of light over the entire 420 - 970 nm spectrum. The AM1.5-weighed average absorption of the 1-μm-thick Si slab with Mie coating is 73.4%, compared to 36.0% of a flat Si slab with same thickness. The Mie scatterers thus more than double the absorption in the Si wafer.

The absorption enhancement is due to both an antireflection effect (see Chapter 6) and light trapping (see Chapter 7). In this Chapter, we are interested in studying the latter. In order to do so, we define a normalized absorption as the absorption spectrum divided by the incoupling spectrum, i.e. the spectrum of light that is coupled into a semi-infinite Si substrate covered with the Si Mie coating. This allows eliminating the antireflection effect from the measured absorption spectra, and comparing the Si Mie light trapping scheme to the Lambertian $4n^2$ light trapping limit. The simulated Mie incoupling spectrum is shown in Fig. 8.2(c) by the dashed purple line. The graph also shows the absorption into a flat uncoated Si wafer (dashed black line), which is used to calculate the normalized absorption of the flat Si slab.

Figure 8.3 shows the normalized absorption, defined as above, of a flat uncoated Si slab (blue) and a Si slab with Mie coating (red), for slab thicknesses of 1 μm (a), 2 μm (b) and 4 μm (c), respectively. Each graph also shows the calculated absorption spectrum for a single pass of light through the Si layer (dashed black line), a double pass (dot-dashed black) and the $4n^2$ limit (solid black).

For the 1-μm-thick slab (a) we observe that the normalized absorption of the uncoated slab oscillates around the double-pass absorption. This is expected, as

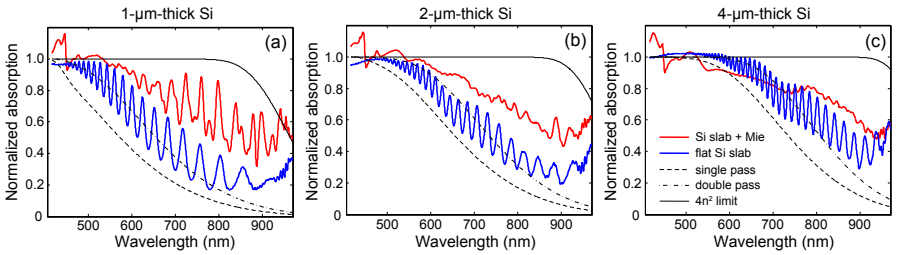

Figure 8.3: Normalized absorption spectra for a flat uncoated Si slab (blue) and a Si slab with Mie coating (red), for slab thicknesses of 1 μm **(a)**, 2 μm **(b)** and 4 μm **(c)**. Each graph also shows the absorption spectrum for a single pass of light through the Si layer (dashed black line), a double pass (dot-dashed black) and the $4n^2$ limit (solid black).

light is reflected by the Si-glass interface at the back. The slab with the Si Mie coating shows a normalized absorption larger than that of a flat slab over the entire spectral range. The normalized absorption is equal to ~1 for wavelengths up to 550 nm. In this spectral range all light that is coupled into the slab is absorbed (the values above 1 for wavelengths shorter than 450 nm are due to a sharp feature in the simulation spectrum used for the normalization procedure, see Fig. 8.2(c)). In the spectral range 550-950 nm, the normalized absorption oscillates between 0.4 and 0.9. Interestingly, we find that for wavelengths larger than 950 nm, the normalized absorption is larger than the absorption in the $4n^2$ limit. A similar behavior is observed for the 2 μm (Fig. 8.3(b)) and 4 μm (Fig. 8.3(c)) Si slabs. In this case however, the normalized absorption does not beat the $4n^2$ limit for any wavelength up to 970 nm.

Next, we convert the measured data to optical path enhancement. Based on the normalized absorption spectra shown in Fig. 8.3, we calculate the optical path length enhancement as: $l(\lambda) = -\frac{\log(1-NA(\lambda))}{\alpha(\lambda)t}$, where $l(\lambda)$ is the optical path length enhancement, $NA(\lambda)$ the normalized absorption, $\alpha(\lambda)$ the absorption coefficient of Si and t the slab thickness. Figure 8.4 shows the optical path length enhancement for the three thicknesses. Si slab with the Si Mie coating (red line), in the near-IR spectral range (700-970 nm). The results are compared with the $4n^2$ limit path length enhancement (black).

As can be seen, the Mie scattering coating on a 1-μm-thick slab leads to a strong optical the path length enhancement that increases from a factor of 5 for short wavelengths to a factor as high as 60 for larger wavelengths. The maximum observed path length enhancement is 65, at a wavelength of 955 nm. The $4n^2$ limit is exceeded for several wavelengths in the spectral range 940-970 nm. Path length enhancements are particularly important at these long wavelengths where Si shows poor absorption. For 2-μm-thick and 4-μm-thick Si slabs (Figs. 8.4(b) and 8.4(c)) the optical path length enhancement increases for larger wavelengths, as for the thinner slab. Maximum values of ~40 and ~18 are reached, respectively. In both

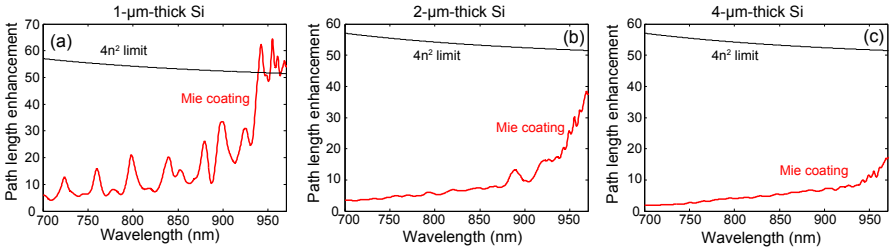

Figure 8.4: Optical path length enhancement for a 1 μm **(a)**, 2 μm **(b)** and 4 μm **(c)** Si slab with the Si Mie coating (red line), in the near-IR spectral range (700-970nm) derived from the experimental data. The results are compared with the Lambertian $4n^2$ path length enhancement limit (black).

cases, however, the $4n^2$ limit is not exceeded for any wavelength up to 970 nm because these slabs show stronger absorption due to their larger thickness.

Finally, note that in the present geometry the path length enhancement is limited by losses that result from outcoupling at the Si/glass back interface. The path length enhancement by using Mie scatterers can be further improved by using a metal back-reflector. Furthermore, it will be interesting to carry out measurements of the path length enhancement at a wavelength range extending beyond the limit of 970 nm studied here.

8.3 Conclusion

We have experimentally demonstrated strong light trapping in thin Si slabs, by using resonant surface Si Mie NCs. By using total reflection and transmission spectroscopy, we have measured the absorption spectra for slabs with thicknesses of 1 μm, 2 μm and 4 μm. In all cases, enhanced absorption is observed over the entire 420-970 nm spectral range for the slabs with the Si Mie coating with respect to a flat uncoated slab. This is due to both an antireflection effect and a light trapping effect. By normalizing the total absorption to an incoupling spectrum (accounting for the antireflection effect), we derive the absorption enhancement that is due to light trapping. For a 1-μm-thick slab, the Si Mie coating provides light trapping beyond the Lambertian $4n^2$ limit in the 940-970 nm spectral range. The optical path length enhancement depends on the wavelength and ranges between 5 and 65. For 2-μm-thick and 4-μm-thick Si slabs, strong light trapping by the Si Mie coating is observed as well but not beyond the $4n^2$ limit, in the spectral range considered. Finally, we note that the Mie scattering geometry used in these experiments was optimized for enhanced light incoupling (antireflection effect). Full optimization of particle size, shape and array pitch may lead to geometries with path length enhancement even higher than demonstrated here.

9

Al_2O_3/TiO_2 nano-pattern antireflection coating with ultralow surface recombination

We present a nano-patterned dielectric coating for crystalline Si solar cells that combines excellent anti-reflection and passivation properties. The nano-patterned coating is comprised of an array of TiO_2 nanocylinders placed on top of an ultra-thin Al_2O_3 layer on a flat Si(100) wafer. The antireflection effect stems from the preferential forward scattering of light through leaky Mie resonances in the TiO_2 nanocylinders. The Al_2O_3 layer provides excellent passivation of the Si surface. We experimentally demonstrate ultralow surface recombination with carrier lifetimes above 4 ms, combined with a reflectivity of 2.8% averaged over a broad spectral range.

9.1 Introduction

Antireflection (AR) coatings and passivation layers are essential components in solar cells. The former are used to reduce unwanted reflection of light from the surface of the solar cell, whereas the latter are used to reduce surface carrier recombination [2]. Standard AR approaches for crystalline Si (c-Si) based devices include transparent dielectric layers [146], micron-sized pyramidal surface texturing [115], and graded-index tapered nanostructures [122–124]. These techniques however present drawbacks such as limited spectral and angular range of operation, increase of surface area and thus increase of surface recombination, and unsuitability

for application to ultra-thin (less than 20 micron) wafers. Recently, we have shown that nano-sized dielectric (Mie) nano-scatterers can be used to achieve broadband omnidirectional low reflectivity for c-Si wafers [137]. An array of Si nano-cylinders (NCs) etched into the surface of a Si wafer reduces the reflectivity of the wafer down to 1.3% in the visible spectral range, and for angles of incidence up to 60 degrees. The mechanism behind the reduced reflectivity is the preferential forward scattering of the incident light through leaky Mie resonances in the dielectric nanoparticles [83, 138]. While this geometry leads to ultra-low reflectivity, a key question is how it affects surface recombination due to both the increased surface area and possible etch-induced damage during the Si NC fabrication.

To study this, we fabricate arrays of Si NCs on top of a double-side polished 270-μm-thick float-zone (FZ) Si wafer and deposit a 30-nm-thick Al_2O_3 passivation layer. Al_2O_3 is well known for its passivation properties [147], and has been used to passivate reactive-ion etched Si surfaces [148]. The Si NC array is fabricated using substrate-conformal imprint lithography (SCIL) and reactive ion etching (RIE), using the same process reported in Chapter 2. The Al_2O_3 passivation layer was deposited by plasma-assisted atomic layer deposition (ALD) at 200°C, followed by annealing at 400°C for 10 min in N_2 environment. Figure 9.1(a) shows a scanning electron microscope (SEM) image of the array of Si NCs after the Al_2O_3 deposition, imaged with a tilt angle of 45 degrees. The inset shows a focused ion beam (FIB) cross-section of two Si NCs, conformally coated with 30 nm Al_2O_3.

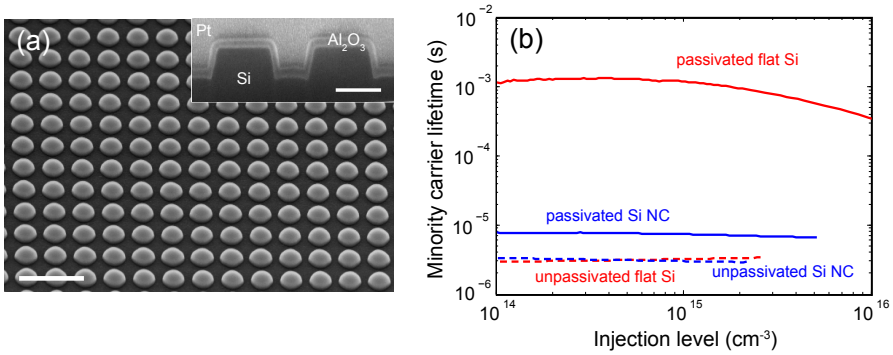

Figure 9.1: **(a)** SEM image of the Si NC array, coated with 30 nm Al_2O_3 (scale bar: 1 μm). The inset shows a FIB cross section of two Si NCs (scale bar: 200 nm). **(b)** Carrier lifetime as a function of injected carrier density, for an unpassivated (dashed red) and passivated (solid red) flat Si reference, and for an unpassivated (dashed blue) and passivated (solid blue) Si wafer coated with Si NCs.

Figure 9.1(b) shows the minority carrier lifetime as a function of the injected carrier density, measured in a Sinton WCT-100 lifetime tester. The graph shows data for an unpassivated (dashed red line) and passivated (solid red) flat Si wafer (reference samples), and for an unpassivated (dashed blue) and passivated (solid blue) Si wafer with the Si NC array, illuminated from the side of the Si NCs. The

reference measurements clearly show the beneficial effect of the Al_2O_3 layer on the surface passivation of a flat Si wafer. For injected carrier densities of 10^{15} cm^{-3}, the carrier lifetime is improved from 3 μs to 1 ms by applying the Al_2O_3 passivation layer. On the other hand, the sample with Si NCs shows only a small improvement in carrier lifetime upon passivation, from 3 μs to 8 μs.

Figure 9.1 shows that the deposition of a standard ALD alumina passivation layer on the surface of the Si Mie NC is not effective in reducing surface recombination. In this Chapter, we present an alternative dielectric nano-patterned Mie AR coating which is fully compatible with a standard Al_2O_3 passivation layer. This Mie coating is comprised of a TiO_2 NC array fabricated on top of a flat, Al_2O_3-passivated Si wafer. We demonstrate that this combined geometry yields ultralow surface recombination velocities and excellent AR properties. Carrier lifetimes up to 4 ms were measured, together with an average reflectivity weighed over the AM1.5 solar spectrum in the 420-980 nm spectral range of 2.8%.

9.2 Experimental results

Figure 9.2(a) shows a schematic of the AR coating and passivation geometry. A square array of TiO_2 nano-cylinders (500 nm pitch) is made on top of a flat 50-nm-thick TiO_2 spacer layer. The TiO_2 cylinders have a diameter of 350 nm and height of 100 nm. From numerical simulations it was found that this geometry yields the optimal anti-reflection properties. The TiO_2 Mie-coating is made on a Si substrate coated with a 5-nm-thick Al_2O_3 passivation layer. Numerical simulations show that, in order to achieve reflectivities below 3%, an Al_2O_3 layer with thickness below 10 nm must be used underneath the TiO_2 Mie coating. For such thin Al_2O_3 layers, plasma-assisted ALD is preferable to thermal ALD in order to achieve excellent surface passivation [147].

Double-side polished n-type float-zone (FZ) Si(100) wafers, with a thickness of 270 micron, and resistivity of 2.5 Ω cm were used for the experiments. The native oxide is removed by a 1 minute dip in a 1% dilute HF solution. The Al_2O_3 passivation layer is then deposited on both sides of the wafer using plasma-assisted ALD at 200 °C, followed by a rapid thermal anneal (RTA) treatment at 400 °C for 10 min in a N_2 environment. Spectroscopic ellipsometry was performed to determine the Al_2O_3 and interfacial SiO_2 layer thicknesses, which were found to be 5 nm and 2 nm, respectively. A 50-nm-thick TiO_2 layer is then deposited using electron beam evaporation from a TiO_2 source. Afterwards, the sample is coated with a PMMA/sol-gel resist, and SCIL is used to imprint a nano-pattern of holes in the sol-gel. A breakthrough RIE using an O_2/N_2 plasma is performed to transfer the hole pattern into the PMMA. The TiO_2 NCs are then fabricated by electron beam evaporation from a TiO_2 source followed by lift-off of the resist. Figure 9.2(b) shows a FIB cross section of the final sample. The left panel shows an overview of the FIB cross section, showing the Si substrate, the array of the TiO_2 NCs and a platinum top layer deposited to protect the array during the FIB milling. The

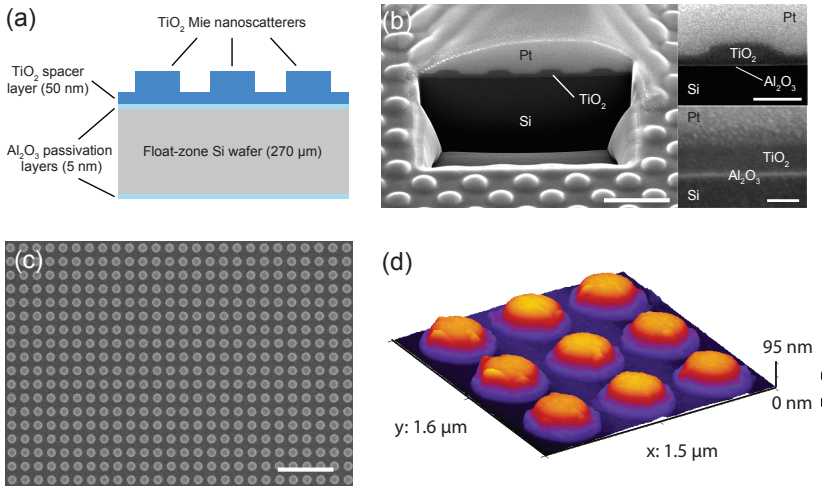

Figure 9.2: **(a)** Schematic of the TiO_2-based Mie coating. **(b)** FIB cross section of the experimental sample. Scale bars: 1 μm in the left panel, 300 nm in the top-right panel and 50 nm in the bottom-right panel. **(c)** SEM top-view of the TiO_2 NC array. Scale bar is 2 μm. **(d)** Surface morphology of the TiO_2 NC array as probed by AFM.

top-right panel shows the cross section of a single TiO_2 nanoparticle on top of the TiO_2 and Al_2O_3 layers. The bottom-right panel is a cross section showing the flat TiO_2 and Al_2O_3 layers, imaged in between two NCs. The thicknesses of these two layers derived from the image are 48 nm and 6 nm, respectively. Figure 9.2(c) is a SEM overview of the TiO_2 NC array, showing the uniformity of the SCIL-imprinted surface. Figure 9.2(d) shows the surface morphology as probed by AFM, which was used to characterize the TiO_2 nanoparticle size and shape. The figure shows that the nanoparticles have a tapered cylindrical shape, with a lower diameter of 380 nm, an upper diameter of 350 nm and height of 85 nm. The nanoparticles are surrounded by a 20-nm-thick "halo" ring at the bottom. This will be discussed further on.

Figure 9.3 shows the minority carrier lifetime as a function of injected carrier concentration for a flat unpassivated Si wafer (black), a flat Si wafer passivated with 5 nm Al_2O_3 (red), a Si wafer passivated with 5 nm Al_2O_3 and coated with TiO_2 NCs (dashed blue line), and the same wafer after applying a post-fabrication RTA treatment at 400 °C for 15 min in N_2 environment (solid blue). Similarly to Fig. 9.1(a), this graph shows that the poor lifetimes of an unpassivated reference Si wafer are drastically improved by the deposition of the Al_2O_3 passivation layer. For injected carrier densities of 10^{15} cm^{-3}, carrier lifetimes up to 5 ms (red line) are achieved by using an Al_2O_3 layer thickness of only 5 nm. After the fabrication of the TiO_2 NCs, a drastic reduction in carrier lifetime is observed (80 μs, dashed blue line). We attribute this mainly to defects in the Al_2O_3 passivation layer that are induced by the vacuum-UV radiation by the RIE plasma used to fabricate the

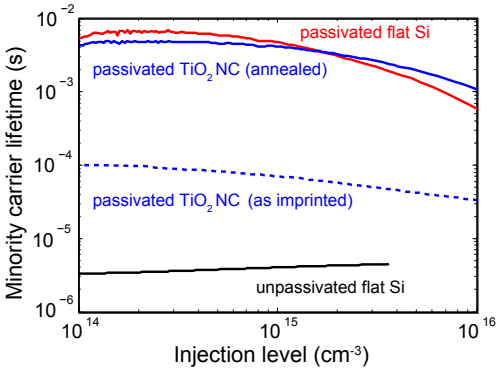

Figure 9.3: Carrier lifetime as a function of injected carrier density, for an unpassivated (black) and passivated (red) flat Si wafers, and for a passivated Si wafer with a TiO_2 Mie coating, before (dashed blue) and after (solid blue) rapid thermal annealing at 400 °C in N_2.

TiO_2 NCs [149]. Sub-surface ion damage in Si due to the RIE may also contribute to degrading the carrier lifetimes. However, very good lifetimes above 1 ms are observed after a post-fabrication RTA treatment at 400 °C is performed. An optimal post-anneal time of 15 min is found at this temperature, yielding lifetimes as high as 4.1 ms for injected carrier densities of 10^{15} cm^{-3}. This lifetime is so high that can only be measured on high-quality FZ-Si wafers. It corresponds to a maximum effective surface recombination velocity of only 3.3 cm/s.

The samples were characterized by total optical reflectivity measurements performed in an integrating sphere setup, with an angle of incidence of 5° off the surface normal. Figure 9.4(a) shows the measured total reflectivity spectrum for a flat uncoated Si wafer (black) and for an Al_2O_3-passivated Si wafer with the TiO_2 Mie coating (solid red line).

The experimental data show a broadband reduction of reflectivity over the entire 420-980 nm spectral range for the TiO_2 Mie coating with respect to the bare Si wafer. This is due to the strong forward scattering from Mie resonances of the TiO_2 nanoparticle [137]. From numerical simulations, we found that the TiO_2 nanoparticle scattering cross section spectrum shows a broad first-order Mie resonance in the spectral range 500-800 nm. It was also found that this resonance originates from a magnetic dipole-like mode, in agreement with [150]. The broadband behavior stems from the fact that the Mie resonance of a nanoparticle in proximity of a high index substrate is "leaky", i.e. only few optical cycles occur before light is fully scattered into the substrate. Overall, the AM1.5-averaged reflectivity of a bare Si wafer (32.2%) is reduced to 5.8% by employing the TiO_2 Mie coating. The dashed red line in Fig. 9.4(a) represents the reflectivity spectrum obtained from Finite Difference Time Domain (FDTD) simulations, using the AFM topography as an input for the particle shape. As can be seen, good agreement is observed between simulated

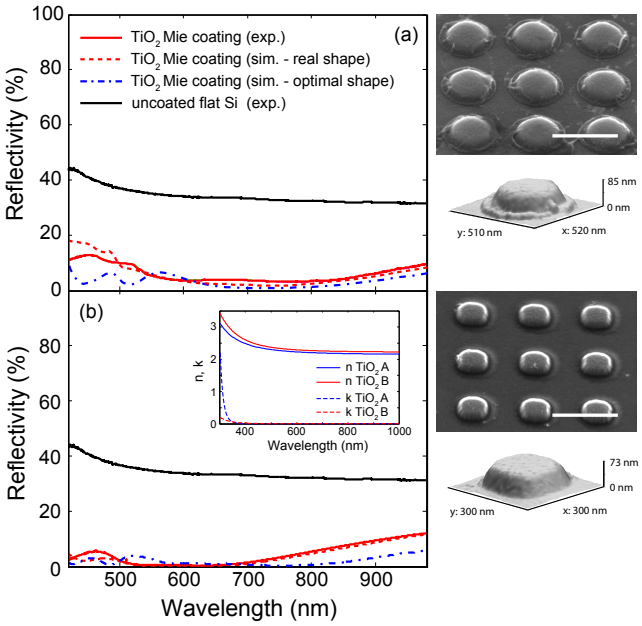

Figure 9.4: (a) Measured reflectivity spectra of a bare Si wafer (black) and a Al_2O_3-passivated Si wafer with a TiO_2 Mie coating (solid red). The TiO_2 is deposited by electron beam evaporation from a TiO_2 source. The dashed lines are the simulated reflectivity spectra of an array of TiO_2 nanoparticles, with particle shape given by the AFM data of the experimental sample (dashed red) and with an optimal particle shape (dashed blue). The optimal nanoparticle shape is a cylinder with diameter of 350 nm and height of 100 nm. The insets on the right show a SEM image of the TiO_2 nanoparticle array (top, scale bar is 500 nm) and the AFM image of a single nanoparticle (bottom). **(b)** Reflectivity spectra measured on a sample fabricated with a different nanoimprint stamp and TiO_2 evaporated using a Ti_3O_5 source. In this case, the optimal nanoparticle dimensions are 300 nm (diameter) and 100 nm (height). The inset shows the optical constants of the TiO_2 evaporated from a TiO_2 source (A), and the TiO_2 evaporated from a Ti_3O_5 source (B). n and k are the real and imaginary part of the refractive index, respectively. The insets on the right show a SEM (top, scale bar is 500 nm) and AFM image (bottom) of the nanoparticles.

and experimental data. The right panels in Fig. 9.4(a) show a SEM image of the nanoparticles (top) and the AFM data of a single nanoparticle (bottom). The actual nanoparticle shape is not ideal, due to the presence of a 20-nm-thick "halo" ring at the bottom. Using FDTD simulations, the case of an ideal cylindrical nanoparticle shape with optimal dimensions was also investigated. The results are shown by the dashed blue line in Fig. 9.4(a). In this case, the AM1.5-averaged reflectivity is found to be 2.8%. For comparison, a double-layer AR coating comprised of a porous (low n) TiO_2 film on top of a dense (high n) TiO_2 film yields an average reflectivity of 6.5% [151].

Figure 9.4(a) shows that a cylindrical particle shape with optimal dimensions is crucial in order to achieve the best AR properties. A second sample series was made using a different nanoimprint stamp and different conditions for the breakthrough etch of the PMMA/sol-gel resist (O_2 instead of O_2/N_2 plasma). Furthermore, in this case the TiO_2 was deposited with electron-beam evaporation using a Ti_3O_5 source, in combination with oxygen flow. The right panels in Fig. 9.4(b) show a SEM image (top) of the nanoparticles fabricated in this way, as well as AFM data of a single nanoparticle (bottom). In this case, a particle shape close to the ideal cylindrical shape was obtained. The nanoparticles have diameter of 250 nm and height of 73 nm, slightly smaller than the optimal dimensions of 300 nm diameter and 100 nm height found with FDTD simulations. Figure 9.4(b) shows the measured total reflectivity spectrum for a flat uncoated Si wafer (black) and for an Al_2O_3-passivated Si wafer with the TiO_2 Mie coating (solid red line). As in Fig. 9.4(a), a broadband reduction is observed for the entire spectral range 420-980 nm. The average reflectivity of the TiO_2 Mie coating is found to be 2.6%. As before, excellent agreement with the simulated data (dashed red line) is observed. The simulated reflection spectrum for a TiO_2 Mie coating with optimal geometry (dashed blue) yields an average reflectivity as low as 1.6%.

Finally, we discuss the effect of the slightly different optical constants of TiO_2, due to electron-beam evaporation from different source materials. The inset in Fig. 9.4(b) shows the real (n) and imaginary part (k) of the refractive index of the TiO_2 used in the experiment of Fig. 9.4(a) (blue, A) and Fig. 9.4(b) (red, B), measured with spectroscopic ellipsometry. The TiO_2 evaporated using a Ti_3O_5 source (B) has a slightly higher n than the TiO_2 evaporated from a TiO_2 source (A), and a lower k (thus lower absorption) in the spectral range below 400 nm. The higher index leads to a lower simulated reflectivity spectrum (dashed blue line in Fig. 9.4(b)).

9.3 Conclusion

In summary, we have presented a TiO_2-nanoparticle-based coating for crystalline Si solar cells, which combines good surface passivation and anti-reflection properties. Carrier lifetimes higher than 4 ms were measured, by using a 5-nm-thick Al_2O_3 passivation layer placed underneath the TiO_2 nanoparticle coating. Total reflection measurements show a broadband AR effect in the spectral range 420-980 nm, with an AM1.5-averaged reflectivity of 2.8%. The low reflectivity stems from the preferential forward scattering of Mie resonances in the TiO_2 nanocylinders.

10

Applications of resonant nanostructures to solar cells

We present several new concepts and ideas for integrating metallic and dielectric resonant nanoparticles on realistic solar cell designs. We show that resonant nanostructures can be beneficial not only for several crystalline Si solar cell designs, but also for GaAs and polymer cells. Practical aspects such as the effect of polymer and glass encapsulation of solar modules are also analyzed.

10.1 Introduction

In the previous Chapters we have presented several ways to use metallic and dielectric resonant nanostructures to improve the solar cell performance. Most of our study focused on understanding the fundamentals of light scattering by resonant nanoparticles (NPs) placed on top of or embedded in a semiconductor substrate. Despite the different physics behind the optical resonances in plasmonic and Mie NPs, two key mechanisms governing the scattering properties of both kinds of NPs are beneficial for solar cell applications. First, both kinds of resonant NPs are characterized by a scattering cross section larger than the NP area. We demonstrated that this allows full interaction of the NPs with the incident light even if an array with less than 30% surface coverage is used. Second, the scattered light is directed preferentially towards the materials with higher refractive index, due to the higher

density of optical states. This effect can be used to enhance the trapping and absorption of light in solar cells based on high-index semiconductors.

In our studies, we have focused almost entirely on high-index crystalline Si (c-Si) substrates. We have used c-Si wafers as a test platform to study both optical properties (reflection, transmission, absorption) and electrical properties (surface passivation) of different resonant nanostructures for c-Si solar cells. However, the concepts shown in this thesis apply to a much wider range of solar cell materials and designs. As mentioned, the preferential forward scattering and light trapping can be used for all solar cells based on high index semiconductors, such as GaAs or CdTe. The case of low-index solar cells has been studied in Chapter 5. There, plasmonic NPs embedded in a polymer layer were used to enhance the absorption of light in the polymer, due to the plasmonic near-field enhancement in proximity of the NP.

In this Chapter, we discuss the application of the fundamental concepts studied so far to practical devices. In particular, we analyze the benefits and drawbacks of applying the resonant nanostructures proposed in this thesis to a wide variety of solar cell designs. The chapter is organized as follows:

- In section 10.2, we present and compare four realistic crystalline Si solar cell designs that can benefit from Mie nanoscatterer coatings.
- In section 10.3, the application of resonant nanostructures to high efficiency GaAs solar cells is studied.
- Section 10.4 describes the use Mie scatterers to direct light towards low-index polymer solar cells, by using the interference of magnetic and electric Mie resonances.
- In section 10.5, we study the antireflection effect of plasmonic and Mie NP coatings when the solar cell is encapsulated in a polymer protective layer.
- Section 10.6 compares and summarizes the results obtained for plasmonic and Mie nanostructure schemes applied to different solar cells designs.
- Section 10.7 presents a nanostructured antireflection coating for glass, with broadband and omnidirectional ultralow reflectivity, that can be used in solar panel encapsulation.

10.2 Crystalline Si solar cells

As a first application, we consider crystalline Si based solar cells. The photovoltaic market is currently dominated by monocrystalline or polycrystalline Si solar cells, which account for ~85% of the market [7]. Furthermore, c-Si based modules have the highest efficiencies amongst commercial single-junction modules [36]. Standard c-Si solar cells currently have thicknesses in the range 140-180 μm [5]. They

employ a pyramidal light-trapping texture coated with a 80-nm-thick Si_3N_4 antireflection layer [2]. The typical feature size of the texturing is in the range 3-10 μm [43, 44]. Despite providing excellent antireflection and light trapping properties for a 180-μm-thick cell, this scheme cannot be used for thinner cells in the micron range, due to the large feature size. Surface Mie nanoscatterers are an ideal candidate to substitute the micron-sized pyramidal texture on thinner cells. In fact, due to the high index of c-Si (~3.5 at 1100 nm), the strong scattering of light mediated by the Mie resonances in the nanoparticles can be used to preferentially couple light into the c-Si. In Chapter 7, we showed that it is possible to make 10-μm-thick c-Si cells with 20% efficiency by using a Si Mie coating. Here we present and discuss the integration of surface Mie nanoscatterers to four different c-Si solar cell devices.

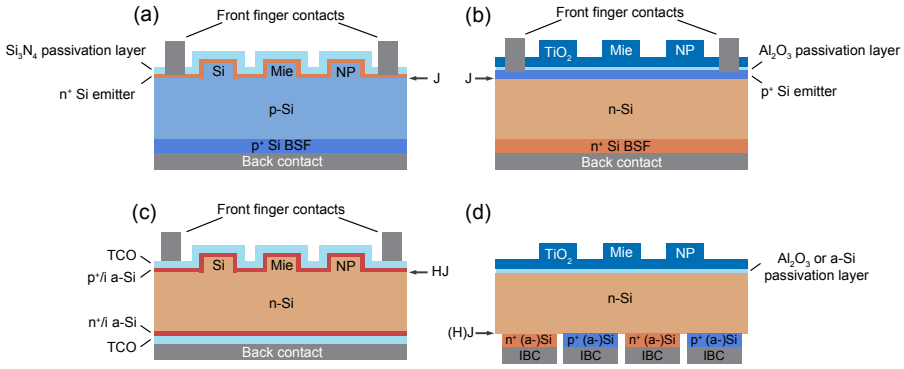

Figure 10.1: Four crystalline Si solar cell designs that can benefit from a Si and TiO_2 nanoparticle coating. **(a)** Si Mie coating applied to a standard p-type Si based solar cell with diffused front junction. **(b)** TiO_2 Mie coating on an n-type Si based solar cell with diffused front junction. **(c)** a-Si:H/c-Si heterojunction with intrinsic layer (HIT) solar cell with a Si Mie coating. **(d)** Interdigitated back contact (IBC) homo- (or hetero-) junction solar cell with a TiO_2 Mie coating.

Figure 10.1 shows the schematics of four existing c-Si solar cell designs on which the Si and TiO_2 Mie coating, presented in Chapters 6 and 9 can be integrated. Figure 10.1(a) shows the most widely used configuration in commercial c-Si cells. In this configuration, a p-type c-Si substrate is used, in combination with a highly doped p-type Si layer at the back acting as a back surface field (BSF) to repel minority carriers, and a metal back contact (usually Al). An n-type emitter is used at the front surface. The Si Mie coating can be integrated (by reactive ion etching) in the front surface of the p-type layer. A highly doped n-type Si layer at the front, conformal to the Si NPs, can then be made by phosphorus diffusion to form a shallow junction. A Si_3N_4 layer with thickness of 50 nm is finally applied to serve as an antireflection coating [137] and passivate the surface [152]. Metallic (Ag) finger contacts can be used at the front. The Mie coating provides excellent antireflection and light trapping properties (see Chapters 6 and 7). However, this geometry presents some drawbacks. The reactive ion etching (RIE) used to fabricate the Si nanopillars

creates additional surface area and near-surface defects in the Si, thus increasing carrier recombination. As shown in Chapter 9, a standard Al_2O_3 passivation layer is ineffective to fully passivate the Si Mie scatterer surface. A different RIE process, based on chemical etching of Si rather than on physical etching, must be used to yield Si surfaces that can be passivated with Al_2O_3 [148]. A second drawback of the geometry shown in Fig. 10.1(a) is that the Mie resonances in the Si NPs enhance the absorption of light in the NPs, i.e. close to the high-recombination region of the highly doped emitter. Finally, the metal contacts are highly recombination active and cause shadowing of light, thus limiting the efficiency of the cell.

Figure 10.1(b) shows a schematic of a solar cell based on an n-type Si wafer. These wafers present two important advantages with respect to p-type wafers: first, they do not suffer from light-induced degradation due to boron-oxygen centers [153–155]; second, they are less sensitive to interstitial iron impurities [156], so that high-quality n-type Si wafers with low bulk recombination rates can be made using a more cost-effective process. The cell configuration is similar to that of Fig. 10.1(a). A diffused heavily doped p-type layer is used in this case to form the junction. For p-type Si, Al_2O_3 yields excellent field-passivation due to the build-in negative charge [147, 157]. This cell configuration can thus take advantage of the TiO_2/Al_2O_3 anti-reflection and passivation coating presented in Chapter 9. As in the case of Fig. 10.1(a), metallic finger contacts can be applied at the front. The advantages of this configuration are the excellent antireflection and passivation properties provided by the TiO_2 Mie scatterers and by the thin Al_2O_3 layer, respectively (see Chapter 9), the low parasitic losses in the visible and infrared spectral range (see Fig. 9.4(b) in Chapter 9) and the good light trapping properties, as shown in Fig. 7.6 in Chapter 7. One drawback, as for the cell in Fig. 10.1(a), is that the TiO_2 Mie scatterers slightly enhance light absorption in the high-recombination p-type emitter at the front, due to the fact that the geometrical Mie resonance overlaps with this region. Shadowing from the front contact also limits the overall cell efficiency.

Figure 10.1(c) shows an application of the Si Mie coating to hetero-junction-with-intrinsic-thin-layer (HIT) c-Si solar cells. These cells are based on an n-type c-Si wafer. An n-doped hydrogenated amorphous Si (a-Si:H) layer is used at the back, as a wider bandgap layer to repel the minority carriers from recombining at the back surface. Similarly, a p-doped a-Si:H layer is used at the front, forming the solar cell junction. An intrinsic a-Si:H intermediate layer is used on both sides, between the doped layers and the c-Si wafer, to reduce the surface state density thus improving surface passivation [140]. Transparent conductive oxides (TCOs) such as Indium Tin Oxide (ITO) are then used in combination with metal grid contacts to extract the carriers from the cell. The separation of the active layer from the highly recombination-active metal contacts provides a high open circuit voltage and therefore a higher efficiency [140]. The Si Mie coating may be integrated in the HIT cell, as shown in Fig. 10.1(c). By making an ultrathin junction conformal to the Si NPs photocarriers generated inside the c-Si NPs can be efficiently extracted from the cell. The HIT Si cell can thus take full advantage of the antireflection

and light trapping properties of the Si Mie coating. Possible drawbacks for this configuration are the fact that it may be difficult to achieve good passivation of the Si Mie scatterer surface. Moreover, the HIT design suffers from increased parasitic losses in the front TCO and a-Si:H layers. As with the two designs above, front contact shadowing also limits the cell performance.

Figure 10.1(d) is a schematic of an interdigitated back-contact (IBC) back-junction c-Si solar cell. As the name indicates, this cell is characterized by the fact that all metallic contacts and the junction are at the backside of the cell. The junction can be either a c-Si homojunction, or an a-Si:H heterojunction similar to the one described in Fig. 10.1(c). The back of the cell alternates highly p-doped Si regions (forming the junction) with highly n-doped regions (forming a BSF), in a interdigitated finger configuration. The front of the cell is usually textured but can also be made totally flat, thus reducing surface recombination. For a flat front-side configuration, a TiO_2 Mie coating made on top of a thin passivation layer provides an ideal antireflection and light trapping scheme. Al_2O_3 can be used as a passivation layer also for n-type Si, as it creates an inversion layer near the surface where holes become majority carriers [158]. Alternatively, an intrinsic a-Si:H layer can be used as a passivation layer. The main advantage of this configuration is the absence of any front shadowing element. The front can be fully patterned with a TiO_2 Mie coating, which is an excellent ARC and has no parasitic losses in the spectral range above 400 nm (see Chapter 9). Another advantage with respect to the previous geometries is that the enhanced light absorption in proximity of the NPs due to the overlap of Mie resonances with the substrate is decoupled from the highly doped region of the emitter (which is at the back). Overall, the configuration in Fig. 10.1(d) takes full advantage of the strong scattering properties of the Mie coating, without any major drawback.

10.3 High-efficiency GaAs solar cells

GaAs solar cells currently hold the world record efficiency for single junction cells, both on cell and on module level [36]. Due to close-to-unity quantum efficiency open-circuit voltages up to 1.1 eV and efficiencies up to 28.8% have been demonstrated for cells under 1-sun illumination [159]. GaAs solar cells usually employ a flat TiO_2/SiO_2 double-layer ARC, but they use no light trapping scheme as the active layer is thick enough (~2 μm) to absorb nearly all light with wavelength up to the band-gap. Surface Mie scatterers can be used in this case to reduce the active layer thickness, and thus reduce the overall fabrication costs of the cell, while maintaining the same absorption of light.

Figure 10.2(a) shows a schematic of a GaAs cell with a TiO_2 Mie coating. The cell comprises an AlInP/GaAs/AlInP layer stack, a metal back contact and a TiO_2 NP array coated with a thin SiO_2 layer at the front. GaAs is used as the active layer of the cell, while AlInP is used for the two window layers. Due to the wider bandgap with respect to GaAs, the AlInP layers repel the minority carriers from the surface, thus

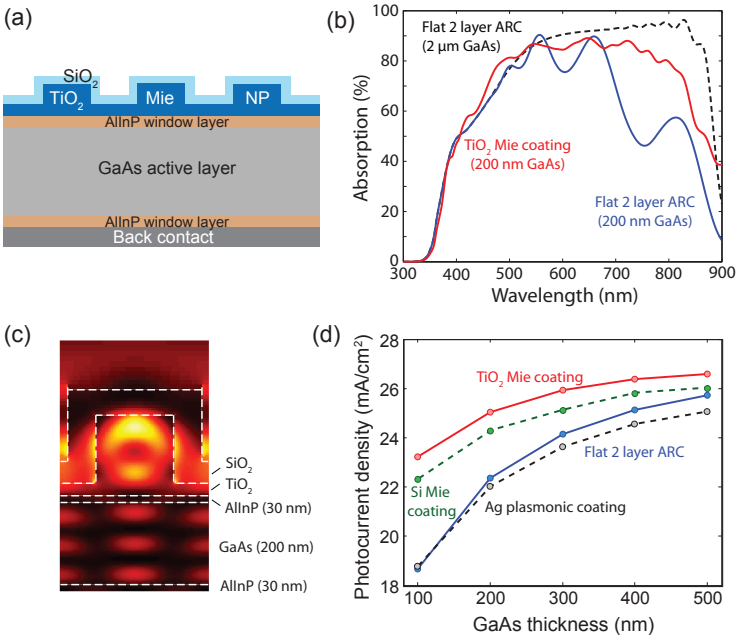

Figure 10.2: Application of Mie and plasmonic coatings to high-efficiency GaAs solar cells. **(a)** Schematic of a GaAs solar cell with the TiO_2 Mie coating. **(b)** Simulated absorption spectra for a 2 μm thick GaAs solar cell with double-layer ARC (dashed black line), a 200 nm thick GaAs cell with double-layer ARC (solid blue line) and for a 200 nm thick GaAs cell with TiO_2 Mie ARC (solid red line). **(c)** Electric field intensity distribution (color scale) in a vertical cross section of the GaAs cell with the TiO_2 Mie coating, for a wavelength of 800 nm. **(d)** Simulated photocurrent density as a function of solar cell thickness for a GaAs solar cell with a standard double-layer ARC (solid blue), a TiO_2 Mie coating (solid red), a Si Mie coating (dashed green) and a Ag plasmonic coating (dashed black).

avoiding surface recombination. Figure 10.2(b) shows the simulated absorption spectra for a 2 μm thick GaAs solar cell with a flat double-layer ARC (dashed black line), a 200 nm thick GaAs cell with a flat double-layer ARC (solid blue line) and for a 200 nm thick GaAs cell with a TiO_2 Mie ARC (solid red line). TiO_2 cylinders with a height of 100 nm and diameter of 350 nm are used in a square array with a pitch of 700 nm. The 2 μm thick cell with a flat double-layer ARC absorbs almost all the light in the spectral range 500-850 nm. The absorption drops below 500 nm due to parasitic losses in the TiO_2 and AlInP window layer. The drop in absorption at 870 nm corresponds to the bandgap of GaAs. From simulations, it follows that the absorption losses due to reflection or incomplete light trapping amount to less than 2%. The absorption of a 200 nm thick GaAs solar cell (solid blue) in the spectral range below 500 nm is similar to that of a 2 μm thick cell, and it is limited by parasitic absorption in the window layer. However, for wavelengths above 600

nm the absorption drops due to incomplete light trapping. The oscillations in the absorption spectrum are due to Fabry-Perot interference in the thin layer stack. Applying the TiO_2 Mie coating on the 200 nm thick cell strongly enhances light absorption in the visible and near-infrared spectral range (solid red line). A 4-fold absorption enhancement is observed for wavelengths close to the GaAs bandgap. The absorption enhancement is due to the coupling of light to waveguide modes in the thin GaAs layer through scattering by leaky Mie resonances in the TiO_2 NPs. Figure 10.2(c) shows an example of a waveguide mode in the GaAs layer. The Figure shows the electric field intensity distribution (color scale) in a vertical cross section of a GaAs cell with the TiO_2 Mie coating, for a wavelength of 800 nm. A periodic electric field pattern is observed in the GaAs layer, corresponding to a waveguide mode in the layer [144, 160]. A clear magnetic dipole Mie resonance is visible inside the TiO_2 NP. Note that no sharp peaks corresponding to waveguide modes are observed in the absorption spectrum of the cell with Mie coating. This is because the waveguide modes are very lossy, due to the strong absorption of GaAs.

The absorption spectra shown in Fig. 10.2(b) can be used to calculate the fraction of photons absorbed in the GaAs layer and the total generated photocurrent, assuming 100% photon-to-carrier conversion efficiency. Figure 10.2(d) shows the photocurrent density as a function of GaAs layer thickness, for a cell with a flat double-layer ARC (solid blue line) and a cell with the TiO_2 Mie coating (solid red). As can be seen, the photocurrent is strongly enhanced for all thicknesses due to the TiO_2 Mie scatterers. The photocurrent enhancement is more significant for thinner cells where light trapping is more relevant. For a 100 nm thick cell the photocurrent is enhanced by 30% due to the TiO_2 Mie coating. For thicker cells, the photocurrent of the cells with a flat coating and with the TiO_2 Mie coating converge to the same value, corresponding to full light absorption. Figure 10.2(d) shows that a 200-nm-thick cell with TiO_2 Mie coating generates nearly as much photocurrent as a 500-nm-thick planar cell. Therefore, the TiO_2 Mie coating allows a significant reduction of material usage, and thus costs, while maintaining similar performance. The graph also shows, for comparison, the simulated photocurrent obtained with a Si Mie coating (dashed green line) and a plasmonic Ag NP coating (dashed black). In both cases, a lower photocurrent is observed with respect to that of a TiO_2 Mie coating for all thicknesses, due to parasitic losses in the NPs. For the case of Ag NPs, the ohmic losses are so large that the cell is outperformed by a flat cell with a double-layer ARC.

10.4 Organic solar cells

So far, Si and GaAs solar cells with a high refractive index have been considered. For these cells, the plasmon-mediated or Mie-mediated scattering of light occurs preferentially towards the high index substrate, mainly due to the higher density of optical states. This yields ultralow reflectivities and strong light trapping properties. However, when lower index substrates are considered, such as e.g. organic solar

cells, the scattering is usually more isotropic. Therefore, alternative routes for light absorption and trapping must be investigated. In Chapter 5, we have shown that plasmonic nanoparticles embedded in a polymer solar cell enhance light absorption in the polymer due to the concentration of light in the near field of the metal NP. This absorption enhancement however comes at the expenses of strong parasitic losses in the metal NP due to ohmic damping. In the following, we propose an alternative concept to direct light into low-index polymer solar cells, based on lossless (or low-loss) dielectric nanoparticles.

Dielectric NPs possess electric and magnetic Mie modes [150]. The magnetic resonances stem from displacement currents excited by the incident light inside the NP. The interference of magnetic and electric modes inside the high-index dielectric NPs affects their scattering behavior. It can be shown that in dielectric NPs with large refractive index (n ~ 3-4), backscattering of light can be strongly suppressed if the electric and magnetic dipoles oscillate in phase [161]. This phenomenon is similar to the scattering behavior of a hypothetical $\epsilon = \mu \neq 1$ particle predicted by Kerker et al. in 1983 [162]. In the following we will thus refer to the suppressed backscattering by high-index dielectric NPs as "Kerker scattering". Recently, experimental demonstration of "Kerker scattering" has been shown for Si [163] and GaAs [161] NPs on glass. The "Kerker scattering" can be used to direct light into a low-index substrate, and thus it can be used to enhance absorption in polymer solar cells.

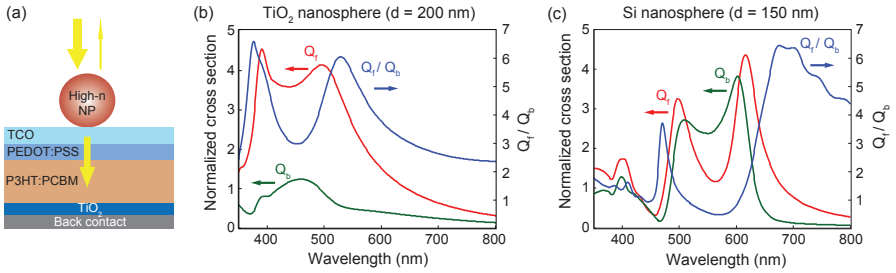

Figure 10.3: A concept based on the "Kerker scattering" of high-index dielectric NP for improving the absorption of light in low-index polymer solar cells. **(a)** Schematic of a typical polymer solar cell with a dielectric nano-scatterer at the front. **(b)** Forward (red) and backward (green) scattering cross sections, normalized to the NP area (left axis), for a 200-nm-diameter TiO_2 NP on glass. The forward-to-backward scattering ratio is also shown (blue, right axis). **(c)** Same plot as in **(b)**, for a 150-nm-diameter Si NP on glass.

Figure 10.3(a) shows a schematic of a typical organic solar cell [164, 165]. The active layer is a mixture of poly(3-hexylthiophene-2,5-diyl) (P3HT) and phenyl-C61-butyric acid methyl ester (PCBM). The index of this polymer blend is n~1.5. A TiO_2 (n~2.3) layer at the back acts as an electron transport layer (ETL), while a poly(3,4-ethylenedioxythiophene) and poly(styrenesulfonate) polymer blend (PEDOT:PSS, n~1.6) acts as a hole transport layer (HTL). The back and front contacts

are metal and TCO, respectively. A high-index dielectric spherical NP is placed on top of the TCO, in order to exploit the enhanced forward scattering of light due to Kerker scattering.

In order to study this effect we simulate a spherical dielectric NP on top of a glass (n=1.46) substrate. As explained before, a high-index NP needs to be chosen in order to effectively suppress the backscattering. Si, GaAs or Ge are good materials to achieve this. However, GaAs and Ge have high absorption in the visible spectral range, and are thus less interesting for achieving large forward scattering. On the other hand, TiO_2 has a lower index (n~2.3), but is lossless in the visible range. We will thus consider in the following TiO_2 and Si nano-scatterers.

Figure 10.3(b) shows the simulated forward (red) and backward (green) scattering cross section (SCS) spectra for a 200-nm-diameter TiO_2 sphere on glass. The SCS spectra are normalized to the geometrical cross section of the NP, and are shown on the left axis. The forward SCS shows two resonances: a magnetic-dipole resonance at ~500 nm and an electric-dipole resonance at ~400 nm [150]. At both resonances, the forward SCS is more than 4 times larger than the geometrical area of the NP. The graph also shows the forward to backward SCS ratio (blue line, right axis). As can be seen, the forward SCS dominates the backward SCS over the entire spectral range 350-800 nm. The forward SCS enhancement with respect to the backward SCS is larger than 2 in the entire spectral range considered. The ratio peaks at wavelengths below the electric dipole resonance and above the magnetic dipole resonance, due to Fano interference [53, 88, 101]. At the peak, the forward to backward SCS ratio is larger than 6.

Figure 10.3(c) shows the simulated forward (red) and backward (green) normalized SCS spectra (left axis) for a 75-nm-radius Si sphere on glass (n=1.45). The forward to backward SCS ratio is also shown (blue, right axis). Similarly to the case of a TiO_2 particle, the graph shows that the forward scattering is enhanced for wavelengths below the electric dipole resonance and above the magnetic dipole resonance. In the broad spectral range 600-800 nm, the forward scattering is strongly enhanced, with a forward to backward scattering ratio exceeding 4. Note however that the total forward SCS in this spectral range is relatively low (less than 2 times the geometrical cross section).

The strong broadband enhancement of the forward scattering may be used to provide an AR coating for low-index polymer solar cells. Changing the NP size gives some tunability of the spectral range over which the forward scattering is enhanced.

10.5 Ethylene vinyl acetate (EVA) encapsulation

In all the studies presented so far, Mie- or plasmon-based coatings have been applied to substrates or solar cells in direct contact with air on the front side. This assumption is useful as it simplifies understanding the fundamental physics of light scattering by resonant nanoparticles placed at an interface. However, in a solar panel, a solar cell is never directly in contact with air. In fact, in a solar module

a polymer layer is used to encapsulate the solar cells (and modules) in order to protect them from environmental degradation and to achieve mechanical rigidity. Usually, ethylene vinyl acetate (EVA) is used for encapsulation. Glass panels are then added on top of the EVA to add physical stability to the module.

The presence of a polymer at the front side of the cell changes the optical environment around the resonant NPs, and thus their scattering properties. In this section we study the effect of EVA encapsulation on the scattering behavior of plasmonic and Mie scatterers. We start our analysis by considering the plasmonic AR coating presented in Chapter 4. This is made of a square array of spheroidal Ag NPs with 180 nm diameter, 130 nm height and 450 nm array pitch, on top of a 50-nm-thick Si_3N_4 spacer layer on Si.

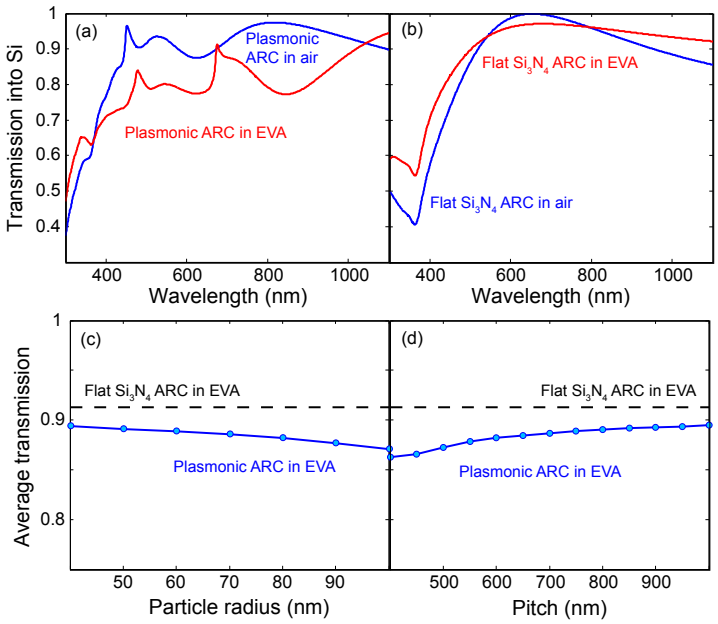

Figure 10.4: Effect of EVA encapsulation on a Ag plasmonic coating for c-Si solar cells. **(a)** Simulated transmission spectra of the plasmonic coating in air (blue) and in EVA (red). **(b)** Simulated transmission spectra of a standard 80-nm-thick Si_3N_4 ARC in air (blue) and EVA (red). **(c)** Average transmission in the Si wafer, weighted with the AM1.5 solar spectrum, of a Ag NP array in EVA, as a function of the NP radius. The average transmission using a standard Si_3N_4 coating in EVA is also shown (dashed black line). **(d)** Average transmission for a Ag NP array in EVA, as a function of the array pitch. The dashed black line is the average transmission for a standard Si_3N_4 coating in EVA.

Figure 10.4(a) shows the simulated transmission into the Si substrate as a function of wavelength, for the plasmonic coating in air (blue) and in EVA (red). Simulations were done using a semi-infinite EVA layer thickness. The plasmonic coating

in air shows a transmission larger than 90% for the entire 450-1100 nm spectral range. We note two main features in the transmission spectrum: a sharp feature at the wavelength of 450 nm and a broad S-shaped feature in the range 600-800 nm. The first is due to a Reyleigh anomaly of the [±1, 0] and [0, ±1] grating orders of the grating formed by the Ag NP, and occurs at a wavelength equal to the array pitch [132, 166]. Note that for wavelengths below 450 nm, the transmission drops because the [±1, 0] and [0, ±1] grating order are allowed in air, and thus contribute to the backscattering. The S-shaped feature at ~700 nm is due to Fano interference, i.e. the constructive interference between scattered and incident waves occurring for wavelengths above the particle LSPR wavelength [88, 167]. When the Ag nanoparticle array is embedded in EVA (red line), both features redshift. The Rayleigh anomaly of the [±1, 0] and [0, ±1] grating orders redshifts to a wavelength of 675 nm. A second Rayleigh anomaly, corresponding to the [±1, ±1] grating orders appears at a wavelength of ~480 nm. These wavelengths satisfy the Rayleigh anomaly conditions: $\lambda_{RA} = \frac{p \cdot n}{\sqrt{m_1+m_2}}$, where p is the array pitch, n the refractive index of the surrounding medium (1.5 for EVA), and m_1 and m_2 are two integers determining the [m_1, m_2] grating order. The redshift of the first order Rayleigh anomaly from 450 nm to 675 nm is thus due to the increase of the surrounding medium refractive index from 1 to 1.5. The Fano line-shape also redshifts to a wavelength of ~1000 nm when the EVA encapsulation is applied. This is also a direct consequence of the large redshift of the LSPR when the particle is embedded in a higher index medium [47]. Both effects drastically reduce the transmission of light into the Si substrate for the 300-1000 nm spectral range. The average transmission, weighted with the AM1.5 solar spectrum, drops from 91% to 80.7%. For comparison, Fig. 10.1(b) shows the transmission spectra of a flat 80-nm-thick Si_3N_4 ARC in air (blue) and EVA (red). For flat ARC in air, perfect impedance matching can be achieved for a single wavelength (λ = 640 nm) due to interference of light in the thin layer, as the condition $n_{ARC} = \sqrt{n_{Si} n_{air}}$ is nearly fulfilled ($n_{Si_3N_4} \simeq 2$, $n_{Si} = 3.5$). However, the transmission drops in the ultraviolet (UV) and near infrared (NIR) spectral ranges. When the same layer is embedded in EVA (red) perfect impedance matching is not achieved for any wavelength. However, overall transmission in the UV and NIR spectral ranges is better than for a flat ARC in air. The average transmission for a flat Si_3N_4 ARC in air and for the EVA covered ARC is 89.4% and 91.3%, respectively. Thus, while the plasmonic coating works better for light coupling than a standard flat Si_3N_4 ARC in air, the opposite is true when an EVA encapsulation is applied. The analysis of the transmission spectra in Fig. 10.1(a) suggests that one way to improve the transmission into Si for a plasmonic ARC is to blueshift both the LSPR of the Ag NPs and the Rayleigh anomalies. The first can be achieved by using smaller NPs, the latter by reducing the array pitch. However, small NPs have higher Ohmic losses (due to lower albedo, see Fig. 4.7 in Chapter 4); and a smaller pitch causes an unwanted redshift of the particle LSPR due to near-field coupling. Thus, a tradeoff of these competing mechanisms must be found. Alternatively, Al NPs may be used, as Al has a plasmon resonance in the blue.

Figure 10.4(c) shows the averaged transmission, weighted with the AM1.5 solar

spectrum, of a Ag NP array in EVA, as a function of the NP radius. The pitch is fixed at 450 nm. The dashed black line shows the average transmission of a flat 80-nm-thick Si_3N_4 coating in EVA (91%). The graph shows that the transmission of the plasmonic coating increases as the NP radius decreases. This is due to the blueshift of the LSPR and thus of the Fano line-shape which increases the overall transmission (see Chapter 3). However, none of the geometries considered yields higher transmission than the standard ARC. Particles with radius smaller than 40 nm are not worth considering, as the albedo is lower than 90% (thus the parasitic absorption is larger than 10%) [53]. The effect of changing the array pitch is shown in Fig. 10.1(d). Surprisingly, larger array pitches yield higher transmission into the Si. Increasing the array pitch has two effects: it blue-shifts the LSPR, due to reduced interparticle coupling, and it red-shifts the Rayleigh anomalies. The first effect increases the overall transmission, whereas the second reduces it. The fact that a higher transmission is observed for larger pitches means that the first effect dominates over the second. None of the geometries beats the standard ARC, as far as light incoupling is concerned. Overall, the trends in Figs. 10.4(c) and 10.4(d) show that a plasmonic coating cannot be better for light incoupling than a flat Si_3N_4 coating when an EVA encapsulation is considered. Full parameter space simulations confirmed this result. We note that, despite their slightly lower light incoupling, metal NPs can lead to enhanced light trapping in thinner solar cells, as was discussed in Chapter 4. To find out if Ag nanoparticles are effective the trade-off between light incoupling and light trapping must be further investigated.

Next, we consider the case of a dielectric NP coating embedded in EVA. In dielectric NPs light is mostly confined inside the particle into a geometrical (Mie) mode. This is different from the case of a plasmonic NP, where light is confined near the particle surface and in the near field outside the particle. For this reason, the scattering behavior of a dielectric nanoparticle is less sensitive to changes in the surrounding optical environment.

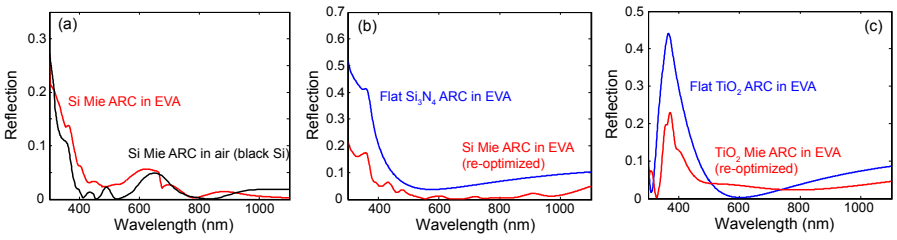

Figure 10.5: Effect of the EVA encapsulation on dielectric Mie coatings. **(a)** Simulated reflectivity spectra of a Si Mie coating in air (black) and in EVA (red). **(b)** Simulated reflection of a Si Mie coating in EVA with geometry optimized for minimal reflection (red). The reflection spectrum of a standard Si_3N_4 coating in EVA is also shown for reference (blue). **(c)** Simulated reflectivity spectra of an optimized TiO_2 Mie coating (red) and a flat TiO_2 coating (blue).

Figure 10.5(a) shows the simulated reflection spectrum for a Si Mie coating in

air (black) and in EVA (red). The Si Mie coating has the same geometry as that presented in Chapter 6, which yields black Si (250 nm diameter cylinders, 150 nm height, 450 nm array pitch, 50 nm Si_3N_4 coating). The graph shows that Si Mie coatings in air and in EVA both yield broadband ultralow reflectivities. The two reflection spectra do not significantly differ from each other. A broadband dip in reflectivity due to scattering of light through the leaky Mie resonance is present in both spectra at wavelengths around 800 nm. The reflection spectrum of the Si Mie coating in EVA shows a sharp feature at 675 nm, due to a first order Rayleigh anomaly (similarly to Fig. 10.1(a)). The scattering from the grating also explains the increase in reflectivity for wavelengths below 675 nm. Overall, the Si Mie coating in air has an AM1.5-weighted average reflectivity of only 1.8%, compared to 3.5% for the Si Mie coating in EVA. As discussed above for plasmonic NPs, we expect that a smaller array pitch can further reduce the reflectivity in the UV and visible range for the EVA covered geometry. However, differently from the case of plasmonic particles, reducing the array pitch does not change the resonant scattering of the single Mie NP, as the particles couple only very weakly through their near field. Figure 10.5(b) shows the simulated reflectivity spectra of an optimized Si Mie coating in EVA (red) and a standard flat Si_3N_4 ARC in EVA (blue). The Si Mie coating shows ultralow reflectivity over the entire 300-1100 nm spectral range. The AM1.5-weighted average reflectivity for the optimized Mie coating in EVA is 2.1%, compared to 9% for the flat Si_3N_4 coating. The optimal geometry found with simulations was: 210 nm particle diameter, 260 nm particle height, 345 nm array pitch and 65 nm Si_3N_4 coating.

Figure 10.5(c) shows the reflectivity spectra of an optimized TiO_2 Mie coating in EVA (red) and a flat single layer TiO_2 coating in EVA (blue). Also in this case, the Mie coating yields lower reflectivity than a flat dielectric coating. The AM1.5-weighted average reflectivity for the TiO_2 Mie coating is 4.2%, while the reflectivity of the flat TiO_2 coating is 6.4%. The simulated optimal geometry is this case is: 120 nm pillar diameter, 80 nm pillar height, 200 nm array pitch on top of a 65 nm thick TiO_2 layer. Interestingly, we note that a flat TiO_2 ARC gives lower reflectivity than a flat Si_3N_4 ARC when EVA is considered. This is due to the fact that almost perfect impedance matching is achieved at $\lambda = 600$ nm, where $n_{TiO_2} = \sqrt{n_{Si} n_{EVA}}$.

10.6 Application of resonant nanostructures to solar cells: summary

Table 10.1 summarizes all results discussed in this Chapter regarding the application of dielectric (Mie) or metallic (plasmonic) resonant nanostructures to different solar cell designs. The table also summarizes the main results presented in the previous Chapters of this thesis.

Three main kinds of resonant nanoscatterers have been considered: Si, TiO_2 (Mie) and Ag (plasmonic) NPs. The first column of the table lists several properties that are key to achieving high efficiency and different solar cell designs as analyzed

in this work. The first 5 rows refer to c-Si solar cells, whereas the last two rows refer to GaAs and polymer solar cells, respectively. The results regarding the Si, TiO_2 and Ag NP coatings are reported in the second, third and fourth column of the table, respectively. Green color is used to indicate good or excellent results, orange indicates that there are some limitations and red means that the NP coating is unsuited for that purpose or solar cell design. The number reported in square brackets in each entry indicates the Chapter of this thesis where more information can be found about that entry.

		Si Mie coating	TiO_2 Mie coating	Ag plasmonic coating
Application to c-Si cells	Antireflection	Excellent (1.3%) [6]	Excellent (1.6%) [9]	Fair (~7%) [4]
	Light trapping (in 1–100 μm cell)	Excellent (21.5% – 20 μm) [7,8]	Good (19.8% – 20 μm) [7]	Not explored (expected limited)*
	Surface passivation	Difficult (τ = 10 μs) [9]	Excellent (τ = 4 ms) [9]	Not explored (expected good)**
	Parasitic losses	None (integrated) [6,7]	Low (only < 400 nm) [9]	Relevant (> 5%) [4,5]
	AR effect with EVA encapsulation	Excellent (R < 2.1%) [10]	Very good (R < 4.2%) [10]	Worse than flat ARC [10]
	Application to GaAs cells	Fair (parasitic losses) [10]	Excellent [10]	Worse than flat ARC (parasitic losses) [10]
	Application to polymer cells	"Kerker" scattering [10]	"Kerker" scattering [10]	Near field (parasitic losses) [5]

Table 10.1: Summary of the effect for Si, TiO_2 and Ag nanoparticle coatings for several properties of solar cell designs that are key to achieving high efficiency. The numbers in square brackets refer to the corresponding thesis chapter. Notes:
* because of parasitic losses in the metal
** because the Ag plasmonic coating can be applied to a flat, passivated solar cell surface, similarly to the TiO_2 Mie coating.

Table 10.1 clearly shows that overall the TiO_2 Mie coating offers the best opportunities for application to solar cells, when compared to the Si and Ag NP coatings. The TiO_2 Mie coating provides excellent antireflection and passivation properties for Si solar cells; it also provides very good light trapping properties for Si and GaAs cells; it can be used in combination with EVA encapsulation; the parasitic losses are small and limited to the spectral range below 400 nm. TiO_2 NPs can also be used to direct light into low-index polymer cell by exploiting the "Kerker scattering".

The Si Mie coating can also be effectively applied to a variety of cell configurations and for different purposes. The AR and light trapping properties for c-Si cells are better than those of the TiO_2, and there are no parasitic losses as the coating is part of the active layer. However, the main drawback for the Si Mie coating is the difficulty in achieving good surface passivation. Furthermore, absorption in the Si NPs becomes an issue when they are applied to GaAs solar cells and polymer solar cells. For the latter however, the "Kerker scattering" can be used as an antireflection effect in the NIR spectral range.

The plasmonic coating is strongly limited in all applications by substantial parasitic losses due to Ohmic damping. A fairly good AR effect can be achieved for Si solar cells using Ag NPs. However, the high sensitivity of the plasmon-mediated scattering to changes in the local optical environment makes the plasmonic coating impractical in combination with EVA encapsulation. The light trapping properties of plasmonic NPs for Si solar cells where not studied in this work. However, based on the studies of AR effect and Ohmic losses carried out in Chapters 4 and 5, only a limited light trapping effect is expected. The effect of Ag NPs on surface passivation was also not investigated in this work. We note that the plasmonic coating can be made on top of a Si_3N_4 dielectric layer, which is usually employed also for surface passivation in c-Si solar cells. We thus expect the plasmonic coating to be easily integrated with a passivation layer, similarly to the TiO_2 Mie coating. The Si_3N_4 spacer layer can also be substituted with Al_2O_3 for better surface passivation, as the two materials have similar refractive index (n~2). Finally, the near-field enhancement occurring near the surface of a plasmonic NP can be exploited to improve the absorption of light in polymer solar cells, if the plasmonic NP are embedded in the active organic layer. Ohmic losses, however, prevent the application of the plasmonic coating to high-efficiency solar cells, such as GaAs cells.

As a final remark, note that in this work only resonant nanoscatterers placed at the front of the solar cell device have been considered (with the exception of Chapter 5). Placing scattering nanostructures at the back of the solar cell as well can also improve the solar cell performance, as demonstrated by many recent studies [56–65] using patterned metallic back contacts. As shown recently, the light trapping by corrugated metal back contacts mainly results from Mie scattering in the dielectric layers that are conformally shaped over the metal [168]. This once again demonstrated the power of dielectric Mie scatterers for light trapping in solar cells.

10.7 Beyond solar cells: a nano-coating for glass

In this last section, we present a nanostructured antireflection coating for glass. Glass is used for several everyday-use applications: windows, lenses, computer and tv screens, portable electronic devices, and solar modules. A bare air-glass interface reflects ~4% of the light. This might seem a low number, however human eyes are very sensitive to light in the visible spectral range and even this small reflection is unwanted in many applications. For example, it is very difficult to read a text on a standard liquid crystal display (LCD) screen in sunlight. Also, 4% reflection loss in a solar panel is ideally avoided.

Glass has a refractive index of about 1.5. A single layer coating with index 1.23 would be needed for optimal antireflection properties. Unfortunately, there are no dielectrics with such a low refractive index. Materials whose index comes close to the optimal value are MgF_2 (n = 1.38) and fluoropolymers (n = 1.3) or nano-porous dielectrics [169]. MgF_2 on a glass surface reduces the reflectance from 4% to about

1%. Multiple-layer coatings made by alternating low- and high-index dielectrics can reduce the reflectivity down to 0.1% [113]. These AR coatings however are more difficult to make and work only for illumination at normal incidence at a fixed wavelength. Here, we present a nanostructured broadband and omnidirectional AR coating for glass, which was inspired by the Si Mie coating presented in Chapter 6. The coating is is comprised of a periodic or random array of glass nanocylinders with dimensions of 150 nm (diameter) and 100 nm (height). In the case of a periodic array, the pitch is 400 nm. The random array has the same surface coverage as the periodic one. From now on, we will refer to this nanostructured coating for glass as nano-glass.

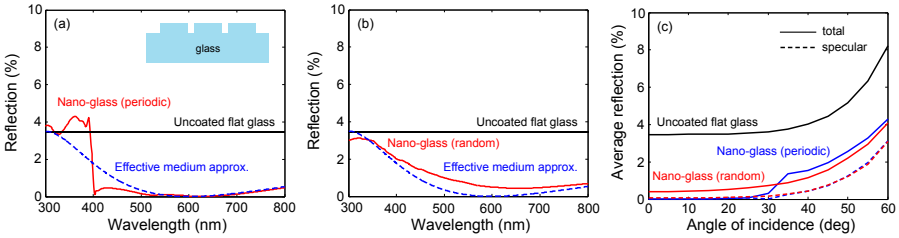

Figure 10.6: Nanostructured coating for glass (nano-glass). **(a)** Simulated reflectivity spectra of uncoated glass (black) and periodic nano-glass (red). The reflectivity calculated with an effective medium approximation is also shown (dashed blue). **(b)** Reflectivity spectra of uncoated glass (black), random nano-glass (red) and an effective medium geometry (dashed blue). **(c)** Reflectivity as a function of angle of incidence for uncoated glass (black), periodic (solid blue) and random (solid red) nano-glass. The dashed lines represent the specular reflectivity. The incident light has wavelength of 600 nm. The data are an average of s- and p-polarization.

First, we consider the case of periodic nano-glass. Figure 10.6(a) shows the simulated reflectivity spectra for uncoated glass (black, ~4%) and for periodic nano-glass (red). This latter shows a broadband reduction in reflectivity over the spectral range 400-800 nm. In the spectral range below 400 nm, the reflectivity is as high as that of a flat uncoated glass. The sudden step in the reflectivity spectrum at a wavelength of 400 nm is due to scattering from the grating. As shown before, for wavelengths below 400 nm the [±1, 0] and [0, ±1] grating orders are allowed in air, and thus contribute to the reflectivity. In order to understand the broadband ultralow reflectivity in the spectral range above 400 nm, we calculate the reflectivity using an effective-medium layer with thickness equal to the glass particle height (100 nm). The effective-medium index is calculated by a weighted-average of the index of glass and air, calculated using the volume filling fractions of the two media. The calculated reflectivity of the effective medium layer is shown by the dashed blue line. Despite being a coarse approximation, the effective-medium reflectivity matches very well the reflectivity of the periodic nano-glass in the spectral range 450-800 nm. For wavelengths below 450 nm, the scattering is dominated by grating

effects. From this analysis we can conclude that the nano-glass coating creates a layer with an effective index (n = 1.25) that effectively acts as an interference ARC. This is different from the case of the Si Mie scattering, where the leaky Mie resonances in the Si nanoparticles played a crucial role in reducing the reflectivity. Overall, the AM1.5-weighted average of the periodic nano-glass is only 0.4%.

Figure 10.6(b) shows the simulated reflectivity spectrum of random nano-glass (red). The reflectivity of uncoated glass is also shown for reference (black). As for the case of periodic nano-glass, the reflectivity is reduced over the entire 300-800 nm spectral range. In this case however, the spectrum does not show the sharp step originated from the scattering by the grating. In contrast, the reflectivity increases smoothly for shorter wavelengths. The graph also shows the reflectivity of an effective-medium layer, calculated as described above (dashed blue line). The nano-glass and effective medium reflectivity spectra have very similar spectral shape. This suggests once again that the physical mechanism behind the reduction of reflection is the creation of a layer with an effective index of 1.25. The small discrepancy between the two spectra can be due to the fact that the random particle configuration creates macroscopic areas with different effective indices. The average reflectivity for the random nano-glass is 0.5%.

Next, we study the angle-dependent reflectivity of nano-glass. Figure 10.6(c) shows the total reflection (solid lines) as a function of angle of incidence (AOI), for uncoated glass (black), and for periodic (blue) and random (red) nano-glass. In all cases, the wavelength of the incident light is fixed at 600 nm and the average reflectivity for s- and p- polarization is calculated. Both periodic and random nano-glass reduce the reflectivity of uncoated glass for all angles of incidence. In both cases, the reflectivity increases up to 4%, for an AOI of 60°, compared to 8% for uncoated glass. The reflection of the periodic nano-glass shows a sudden step at an AOI of 30°, due to the reflection of non-specular grating orders for AOI larger than 30°. The periodic nano-glass performs better for smaller angles of incidence, whereas the random nano-glass yields lower reflecivities for larger angles of incidence. The graph also shows (dashed lines) the specular reflection of the periodic (blue) and random (red) nano-glass. Specular reflection is what causes the unwanted glare on a smartphone or laptop screen in sunlight. The graph shows that the specular reflection of both a random and periodic nano-glass is below 1% for AOI up to 50°, a major improvement over standard glass. The nano-glass can thus be used to reduce unwanted glare effects on glass surfaces. Moreover, it is an ideal geometry to reduce the reflectivity of the solar panel glass encapsulation. Furthermore, the nano-glass geometry can also have hydrophobic properties [170], which is beneficial for many applications.

Finally, we note that the optimal nano-glass design presented here can be readily made using soft imprint lithography.

References

[1] P. Würfel, *Physics of Solar Cells: From Basic Principles to Advanced Concepts*, Wiley-VCH, 2009.

[2] M. A. Green, *Solar Cells: Operating Principles, Technology and System Applications*, Univ. New South Wales, 1998.

[3] M. A. Green, *High Efficiency Silicon Solar Cells*, Aedermannsdorf, Trans Tech Publications, 1987.

[4] *Key World Energy Statistics*, Technical report, International Energy Agency, 2012.

[5] *International Technology Roadmap for Photovoltaic*, Technical report, SEMI PV Group, 2013.

[6] *Technology Roadmap - Solar Photovoltaic Energy*, Technical report, International Energy Agency, 2012.

[7] A. Jäger-Waldau, *PV Status Report 2013*, Technical report, Joint Research Center, 2013.

[8] J. Zhao, A. Wang, M. A. Green, and F. Ferrazza, *Novel 19.8% efficient "honeycomb" textured multicrystalline and 24.4% monocrystalline silicon solar cells*, Applied Physics Letters **73**, 1991 (1998).

[9] N. W. Ashcroft and N. D. Mermin, *Solid State Physics*, Brooks Cole, 1976.

[10] D. J. Friedman, *Progress and challenges for next-generation high-efficiency multijunction solar cells*, Current Opinion in Solid State and Materials Science **14**, 131 (2010).

[11] R. A. Sherif, R. R. King, N. H. Karam, and D. R. Lillington, *The path to 1 GW of concentrator photovoltaics using multijunction solar cells*, in *Photovoltaic Specialists Conference, 2005. Conference Record of the Thirty-first IEEE*, 2005.

[12] R. R. King, D. C. Law, K. M. Edmondson, C. M. Fetzer, G. S. Kinsey, H. Yoon, R. A. Sherif, and N. H. Karam, *40% efficient metamorphic GaInP/GaInAs/Ge multijunction solar cells*, Applied Physics Letters **90**, 183516 (2007).

[13] T. J. Coutts, J. S. Ward, D. L. Young, K. A. Emery, T. A. Gessert, and R. Noufi, *Critical issues in the design of polycrystalline, thin-film tandem solar cells*, Progress in Photovoltaics: Research and Applications **11**, 359 (2003).

[14] K. Tanabe, *A review of ultrahigh effciency III-V semiconductor compound solar cells: multijunction tandem, lower dimensional, photonic up/down conversion and plasmonic nanometallic structures*, Energies **2(3)**, 504 (2009).

[15] A. G. Imenes and D. R. Mills, *Spectral beam splitting technology for increased conversion effciency in solar concentrating systems: a review*, Solar Energy Materials & Solar Cells **84**, 19 (2004).

[16] A. Barnett et al., *Very High Efficiency Solar Cell Modules,* Progress in Photovoltaics: Research and Applications **17**, 75 (2009).

[17] M. A. Green and A. Ho-Baillie, *Forty three per cent composite split-spectrum concentrator solar cell effciency,* Progress in Photovoltaics: Research and Applications **18**, 42 (2010).

[18] A. Polman and H. Atwater, *Photonic design principles for ultrahigh-efficiency photovoltaics,* Nature Materials **11**, 174 (2012).

[19] M. A. Green, *Third Generation Photovoltaics: Ultra-high Conversion Efficiency at Low Cost,* Progress in Photovoltaics: Research and Applications **9**, 123 (2001).

[20] M. A. Green, *Third Generation Photovoltaics: Advanced Solar Energy Conversion*, Springer, 2003.

[21] A. Martí and A. Luque, *Next Generation Photovoltaics: High Efficiency through Full Spectrum Utilization*, Institute of Physics, 2003.

[22] T. Trupke, M. A. Green, and P. Würfel, *Improving solar cell efficiencies by down-conversion of high-energy photons,* Journal of Applied Physics **92**, 1668 (2002).

[23] B. S. Richards, *Luminescent layers for enhanced silicon solar cell performance: Down-conversion,* Solar Energy Materials & Solar Cells **90**, 1189 (2006).

[24] W. G. J. H. M. van Sark, A. Meijerink, R. E. I. Schropp, J. A. M. van Roosmalen, and E. H. Lysen, *Enhancing solar cell efficiency by using spectral converters,* Solar Energy Materials & Solar Cells **1987**, 395 (2005).

[25] C. Strümpel, M. McCann, G. Beaucarne, V. Arkhipov, A. Slaoui, V. Švrček, C. del Cañizo, and I. Tobias, *Modifying the solar spectrum to enhance silicon solar cell efficiency - An overview of available materials,* Solar Energy Materials & Solar Cells **91**, 238 (2007).

[26] A. Shalav, B. S. Richards, and M. A. Green, *Luminescent layers for enhanced silicon solar cell performance: Up-conversion,* Solar Energy Materials & Solar Cells **91**, 829 (2007).

[27] A. Luque, A. Martí, and A. J. Nozik, *Solar Cells Based on Quantum Dots: Multiple Exciton Generation and Intermediate Bands,* MRS Bulletin **32**, 236 (2007).

[28] A. J. Nozik, M. C. Beard, J. M. Luther, M. Law, R. J. Ellingson, and J. C. Johnson, *Semiconductor Quantum Dots and Quantum Dot Arrays and Applications of Multiple Exciton Generation to Third-Generation Photovoltaic Solar Cells,* Chemical Reviews **110**, 6873 (2010).

[29] J. J. H. Pijpers, R. Ulbricht, K. J. Tielrooij, A. Osherov, Y. Golan, C. Delerue, G. Allan, and M. Bonn, *Assessment of carrier-multiplication efficiency in bulk PbSe and PbS,* Nature Physics **5**, 811 (2009).

[30] R. T. Ross and A. J. Nozik, *Efficiency of hot-carrier solar energy converters,* Journal of Applied Physics **53**, 3813 (1982).

[31] M. W. Knight, H. Sobhani, P. Nordlander, and N. J. Halas, *Photodetection with Active Optical Antennas,* Science **332**, 702 (2011).

[32] A. Luque and A. Martí, *Increasing the effciency of ideal solar cells by photon induced transitions at intermediate levels,* Physical Review Letters **78**, 5014 (1997).

[33] A. Martí, M. López, E. Antolín, E. Cánovas, C. Stanley, C. Farmer, L. Cuadra, and A. Luque, *Novel semiconductor solar cell structures: The quantum dot intermediate band solar cell,* Thin Solid Films **511**, 638 (2006).

[34] A. Martí, L. Cuadra, and A. Luque, *Partial filling of a quantum dot intermediate band for solar cells,* IEEE Transactions on Electronic Devices **48**, 2394 (2002).

[35] W. Shockley and H. J. Queisser, *Detailed Balance Limit of Efficiency of pn Junction Solar Cells,* Journal of Applied Physics **32**, 510 (1961).

[36] M. A. Green, K. Emery, Y. Hishikawa, W. Warta, and E. D. Dunlop, *Solar cell efficiency*

tables (version 42), Progress in Photovoltaics: Research and Applications **21**, 827 (2013).

[37] *http://rredc.nrel.gov/solar/spectra/am1.5/ASTMG173/ASTMG173.html*.

[38] M. A. Green, *Limits on the Open-circuit Voltage and Efficiency of Silicon Solar Cells Imposed by Intrinsic Auger Processes*, IEEE Transactions on Electronic Devices **31**, 671 (1984).

[39] T. Kinoshita, D. Fujishima, A. Yano, A. Ogane, S. Tohoda, K. Matsuyama, Y. Nakamura, N. Tokuoka, H. Kanno, H. Sakata, M. Taguchi, and E. Maruyama, *The approaches for high efficiency HIT solar cell with very thin (<100 µm) silicon wafer over 23%*, Proceedings, 26th European Photovoltaic Solar Energy Conference, Hamburg , 871 (2011).

[40] H. A. Atwater and A. Polman, *Plasmonics for improved photovoltaic devices*, Nature Materials **9**, 205 (2010).

[41] E. Yablonovitch, *Statistical ray optics*, Journal of Optical Society of America **72**, 899 (1982).

[42] H. W. Deckman, C. R. Roxlo, and E. Yablonovitch, *Maximum statistical increase of optical absorption in textured semiconductor films*, Optics Letters **8**, 491 (1983).

[43] P. Campbell and M. A. Green, *Light trapping properties of pyramidally textured surfaces*, Journal of Applied Physics **62**, 243 (1987).

[44] P. Campbell and M. A. Green, *High performance light trapping textures for monocrystalline silicon solar cells*, Solar Energy Materials & Solar Cells **65**, 369 (2001).

[45] P. Spinelli, B. Macco, M. A. Verschuuren, W. M. M. Kessels, and A. Polman, *Al_2O_3/TiO_2 nano-pattern antireflection coating with ultralow surface recombination*, Applied Physics Letters **102**, 233902 (2013).

[46] J. Barbè, A. F. Thomson, E.-C. Wang, K. McIntosh, and K. R. Catchpole, *Nanoimprinted TiO_2 sol-gel passivating diffraction gratings for solar cell applications*, Progress in Photovoltaics: Research and Applications **20**, 143 (2012).

[47] U. Kreibig and M. Vollmer, *Optical Properties of Metal Clusters*, Springer, 1995.

[48] C. F. Bohren and D. R. Huffman, *Absorption and Scattering of Light by Small Particles*, Wiley, 2008.

[49] H. R. Stuart and D. G. Hall, *Absorption enhancement in silicon-on-insulator waveguides using metal island films*, Applied Physics Letters **69**, 2327 (1996).

[50] D. M. Schaadt, B. Feng, and E. T. Yu, *Enhanced semiconductor optical absorption via surface plasmon excitation in metal nanoparticles*, Applied Physics Letters **86**, 063106 (2005).

[51] K. R. Catchpole and A. Polman, *Design principle for particle plasmon enhanced solar cells*, Applied Physics Letters **93**, 191113 (2008).

[52] S. Mokkapati, F. J. Beck, K. R. Catchpole, and A. Polman, *Designing periodic arrays of metal nanoparticles for light-trapping applications in solar cells*, Applied Physics Letters **95**, 053115 (2009).

[53] P. Spinelli, M. Hebbink, R. de Waele, L. Black, F. Lenzmann, and A. Polman, *Optical Impedance Matching Using Coupled Plasmonic Nanoparticle Arrays*, Nano Letters **11**, 1760 (2011).

[54] D. Derkacs, S. H. Lim, P. Matheu, W. Mar, and E. T. Yu, *Improved performance of amorphous silicon solar cells via scattering from surface plasmon polaritons in nearby metallic nanoparticles*, Applied Physics Letters **89**, 093103 (2006).

[55] S. Pillai, K. R. Catchpole, T. Trupke, and M. A. Green, *Surface plasmon enhanced silicon solar cells*, Journal of Applied Physics **101**, 093105 (2007).

[56] K. Tvingstedt, N. K. Person, O. Inganäs, A. Rahachou, and I. V. Zozoulenko, *Surface plasmon increase absorption in polymer photovoltaic cells*, Applied Physics Letters **91**, 113514 (2007).

[57] M. J. Keevers, T. L. Young, U. Schubert, and M. A. Green, *10% efficient CSG minimodules*, Proc. 22nd Eur. Photovoltaic Solar Energy Conf. Milan, Italy, 3-7 September 2007 .

[58] F. J. Haug, T. Söderström, O. Cubero, V. Terrazzoni-Daudrix, and C. Ballif, *Plasmonic absorption in textured silver back reflectors of thin film solar cells*, Journal of Applied Physics **104**, 064509 (2008).

[59] R. Franken, R. L. Stolk, H. Li, C. H. M. van der Werf, J. K. Rath, and R. E. I. Schropp, *Understanding light trapping by light-scattering textured back electrodes in thin-film n-i-p silicon solar cells*, Journal of Applied Physics **014503**, 2007 (102).

[60] R. E. I. Schropp, H. B. T. Li, R. Franken, J. K. Rath, C. H. M. van der Werf, J. A. Schüttauf, and R. L. Stolk, *Nanostructured thin films for multibandgap silicon triple junction solar cells*, Solar Energy Materials & Solar Cells **93**, 1129 (2009).

[61] C. Rockstuhl, S. Fahr, and F. Lederer, *Absorption enhancement in solar cells by localized plasmon polaritons*, Journal of Applied Physics **104**, 123102 (2008).

[62] P. N. Saeta, V. E. Ferry, D. Pacifici, J. N. Munday, and H. A. Atwater, *How much can guided modes enhance absorption in thin film solar cells?*, Optics Express **17**, 20975 (2009).

[63] V. E. Ferry, M. A. Verschuuren, H. B. T. Li, R. E. I. Schropp, H. A. Atwater, and A. Polman, *Improved red-response in thin film a-Si:H solar cells with soft-imprinted plasmonic back reflectors*, Applied Physics Letters **95**, 183503 (2009).

[64] V. E. Ferry, M. A. Verschuuren, H. B. T. Li, E. Verhagen, R. J. Walters, R. E. I. Schropp, H. A. Atwater, and A. Polman, *Light trapping in ultrathin plasmonic solar cells*, Optics Express **18**, 128370 (2010).

[65] V. E. Ferry, M. A. Verschuuren, M. van Lare, R. E. I. Schropp, H. A. Atwater, and A. Polman, *Optimized spatial correlations for broadband light trapping nanopatterns in high effciency ultrathin film a-Si:H solar cells*, Nano Letters **11**, 4239 (2011).

[66] B. P. Rand, P. Peumans, and S. R. Forrest, *Long-range absorption enhancement in organic tandem thin-film solar cells containing silver nanoclusters*, Journal of Applied Physics **96**, 7519 (2004).

[67] S. S. Kim, S.-I. Na, J. Jo, D. Y. Kim, and Y.-C. Nah, *Plasmon enhanced performance of organic solar cells using electrodeposited Ag nanoparticles*, Applied Physics Letters **93**, 073307 (2008).

[68] A. J. Morfa, K. L. Rowlen, T. H. Reilly III, M. J. Romero, and J. van de Lagemaat, *Plasmon-enhanced solar energy conversion in organic bulk heterojunction photovoltaics*, Applied Physics Letters **92**, 013504 (2008).

[69] N. C. Lindquist, W. A. Luhman, S. H. Oh, and R. J. Holmes, *Plasmonic nanocavity arrays for enhanced effciency in organic photovoltaic cells*, Applied Physics Letters **93**, 123308 (2008).

[70] S. Vedraine, P. Torchio, H. Derbal-Habak, F. Flory, V. Brissonneau, D. Duche, J. J. Simon, and L. Escoubas, *Plasmonic structures integrated in organic solar cells*, S.P.I.E. Proceedings to the "Optics and Photonics" 2010, "Next Generation (Nano) Photonic and Cell Technologies for Solar Energy Conversion" Conference, San Diego (US) **7772**, 777219 (2010).

[71] M. Westphalen, U. Kreibig, J. Rostalski, H. Lüth, and D. Meissner, *Metal cluster enhanced organic solar cells*, Solar Energy Materials & Solar Cells **61**, 97 (2000).

[72] C. Hägglund, M. Zäch, and B. Kasemo, *Enhanced charge carrier generation in dye sensitized solar cells by nanoparticle plasmons*, Applied Physics Letters **92**, 013113 (2008).

[73] S. D. Standridge, G. C. Schatz, and J. T. Hupp, *Distance dependence of plasmon-enhanced photocurrent in dye-sensitized solar cells*, Journal of American Chemical Society **131**, 8407 (2009).

[74] M. A. Verschuuren, *Substrate conformal imprint lithography for nanophotonics*, PhD thesis, Utrecht University, 2010.

[75] M. A. Verschuuren and H. van Sprang, *3D photonic structures by sol-gel imprint lithography*, 2007 Material Research Society Symposium Proceedings **1002**, N03 (2007).

[76] D. Xu, B. Xiong, G. Wu, Y. Ma, Y. Wang, and E. Jing, *Characterization of wafer-level XeF_2 Gas-phase Isotropic Etching For MEMS Processing*, 7th IEEE International Conference on Nano/Micro Engineered and Molecular Systems (NEMS) , 274 (2012).

[77] H. B. Pogge, J. A. Bondur, and P. J. Burkhardt, *Reactive Ion Etching of Silicon with Cl_2/Ar*, Journal of Electrochemical Society **7**, 1592 (1983).

[78] I. W. Rangelow and H. Löschner, *Reactive ion etching for microelectrical mechanical system fabrication*, Journal of Vacuum Science & Technology, B **13(6)**, 2394 (1995).

[79] R. Legtenberg, H. Jansen, M. de Boer, and M. Elwenspoek, *Anisotrapic Reactive Ion Etching of Silicon Using $SF_6/O_2/CHF_3$ Gas Mixtures*, Journal of Electrochemical Society **142(6)**, 2020 (1995).

[80] P. M. Kopalidis and J. Jorne, *Langmuir Probe Measurements and Characterization of Silicon Etching in SF_6/O_2 Discharges*, Journal of Electrochemical Society **139**, 839 (1992).

[81] Y. Tzeng and T. H. Lin, *Dry Etching of Silicon Materials in SF_6 Based Plasmas*, Journal of the Electrochemical Society **134**, 2304 (1987).

[82] M. Zhang, J. Z. Li, I. Adesida, and E. D. Wolf, *Reactive ion etching for submicron structures of refractory metal silicides and polycides*, Journal of Vacuum Science & Technology, B **1**, 1037 (1983).

[83] G. Mie, *Beiträge zur Optik trüber Medien, speziell kolloidaler Metallösungen*, Annalen der Physik **330**, 377 (1908).

[84] H. R. Stuart and D. G. Hall, *Island size effects in nanoparticle-enhanced photodetectors*, Applied Physics Letters **73**, 3815 (1998).

[85] P. Matheu, S. H. Lim, D. Derkacs, C. McPheeters, and E. T. Yu, *Metal and dielectric nanoparticle scattering for improved optical absorption in photovoltaic devices*, Applied Physics Letters **93**, 113108 (2008).

[86] K. R. Catchpole and A. Polman, *Plasmonic solar cells*, Optics Express **16**, 21793 (2008).

[87] S. H. Lim, W. Mar, P. Matheu, D. Derkacs, and E. T. Yu, *Photocurrent spectroscopy of optical absorption enhancement in silicon photodiodes via scattering from surface plasmon polaritons in gold nanoparticles*, Journal of Applied Physics **101**, 106309 (2007).

[88] B. Luk'yanchuk, N. I. Zheludev, S. A. Maier, N. J. Halas, P. Nordlander, H. Giessen, and C. T. Chong, *The Fano resonance in plasmonic nanostructures and metamaterials*, Nature Materials **9**, 707 (2010).

[89] C. Hägglund, M. Zäch, G. Petersson, and B. Kasemo, *Electromagnetic coupling of light into a silicon solar cell by nanodisk plasmons*, Applied Physics Letters **92**, 053110 (2008).

[90] *Lumerical, FDTD Solutions 7 (www.lumerical.com).*

[91] http://docs.lumerical.com/en/fdtd/user_guide_tfsf_sources.html.
[92] E. D. Palik, *Handbook for Optical Constants for solids,* Academic, 1985.
[93] J. Mertz, *Radiative absorption, fluorescence, and scattering of a classical dipole near a lossless interface: a unified description,* Journal of Optical Society of America B **17**, 1906 (2000).
[94] F. J. Beck, A. Polman, and K. R. Catchpole, *Tunable light trapping for solar cells using localized surface plasmons,* Journal of Applied Physics **105**, 114310 (2009).
[95] G. Xu, M. Tazawa, P. Jin, S. Nakao, and K. Yoshimura, *Wavelength tuning of surface plasmon resonance using dielectric layers,* Applied Physics Letters **82**, 3811 (2003).
[96] D. Derkacs, W. V. Chen, P. M. Matheu, S. H. Lim, P. K. L. Yu, and E. T. Yu, *Nanoparticle-induced light scattering for improved performance of quantum-well solar cells,* Applied Physics Letters **93**, 091197 (2008).
[97] K. Nakayama, K. Tanabe, and H. A. Atwater, *Plasmonic nanoparticle enhanced light absorption in GaAs solar cells,* Applied Physics Letters **93**, 121904 (2008).
[98] T. L. Temple, G. D. K. Mahanama, H. S. Reehal, and D. M. Bagnall, *Influence of localized surface plasmon excitation in silver nanoparticles on the performance of silicon solar cells,* Solar Energy Materials & Solar Cells **93**, 1978 (2009).
[99] T. J. Kippenberg, A. L. Tchebotareva, J. Kalkman, A. Polman, and K. J. Vahala, *Purcell-Factor-Enhanced Scattering from Si Nanocrystals in an Optical Microcavity,* Physical Review Letters **103**, 027406 (2009).
[100] N. A. Mirin, K. Bao, and P. Nordlander, *Fano Resonances in Plasmonic Nanoparticle Aggregates,* Journal of Physical Chemistry A **113**, 4028 (2009).
[101] J. B. Lassiter, H. Sobhani, J. A. Fan, J. Kundu, F. Capasso, P. Nordlander, and N. J. Halas, *Fano Resonances in Plasmonic Nanoclusters: Geometrical and Chemical Tunability,* Nano Letters **10**, 3184 (2010).
[102] P. Spinelli, V. E. Ferry, J. van de Groep, M. van Lare, M. A. Verschuuren, R. E. I. Schropp, H. A. Atwater, and A. Polman, *Plasmonic light trapping in thin-film Si solar cells,* Journal of Optics **14**, 24002 (2012).
[103] E. Thimsen, F. Le Formal, M. Grätzel, and S. C. Warren, *Influence of plasmonic Au nanoparticles on the photoactivity of Fe_2O_3 electrodes for water splitting,* Nano Letters **11**, 35 (2011).
[104] M. Kirkengena, J. Bergli, and Y. M. Galperin, *Direct generation of charge carriers in c-Si solar cells due to embedded nanoparticles,* Journal of Applied Physics **102**, 093713 (2007).
[105] J.-Y. Lee and P. Peumans, *The origin of enhanced optical absorption in solar cells with metal nanoparticles embedded in the active layer,* Optics Express **18(10)**, 10078 (2010).
[106] A. Alù and N. Engheta, *Effect of small random disorders and imperfections on the performance of arrays of plasmonic nanoparticles,* New Journal of Physics **12**, 013015 (2010).
[107] A. Alù and N. Engheta, *Multifrequency optical invisibility cloak with layered plasmonic shells,* Physical Review Letters **100**, 113901 (2008).
[108] L. H. Slooff, S. C. Veenstra, J. M. Kroo, D. J. D. Moet, J. Sweelssen, and M. M. Koetse, *Determining the internal quantum effciency of highly effcient polymer solar cells through optical modeling,* Applied Physics Letters **90**, 143506 (2007).
[109] I. Cesar, K. Sivula, A. Kay, R. Zboril, and M. Grätzel, *Influence of feature size, film thickness, and silicon doping on the performance of nanostructured hematite photoanodes for solar water splitting,* Physical Chemistry C **113**, 772 (2009).
[110] S. Vedraine, P. Torchio, D. Duche, F. Flory, J. J. Simon, J. Le Rouzo, and L. Escoubas,

Intrinsic absorption of plasmonic structures for organic solar cells, Solar Energy Materials & Solar Cells **95**, S57 (2011).

[111] *Nature's guiding light (editorial),* Nature Photonics **2**, 639 (2008).

[112] D. Gevaux, *Reflection! What reflection?,* Nature Photonics **1**, 186 (2007).

[113] H. A. Macleod, *Thin-Film Optical Filters,* Elsevier, 1969.

[114] M. W. P. E. Lamers, C. Tjengdrawira, M. Koppes, I. J. Bennett, E. E. Bende, T. P. Visser, E. Kossen, B. Brockholz, A. A. Mewe, I. G. Romijn, E. Sauar, L. Carnel, S. Julsrud, T. Naas, P. C. de Jong, and A. W. Weeber, *17.9% Metal-wrap-through mc-Si cells resulting in module effciency of 17.0%,* Progress in Photovoltaics: Research and Applications **20**, 62 (2012).

[115] W. H. Southwell, *Pyramid-array surface-relief structures producing antireflection index matching on optical surfaces,* Journal of Optical Society of America **8**, 549 (1991).

[116] E. Yablonovitch and G. D. Cody, *Intensity Enhancement in Textured Optical Sheets for Solar Cells,* IEEE Transactions on Electron Devices **29**, 300 (1982).

[117] P. B. Clapham and M. C. Hutley, *Reduction of lens reflection by the "Moth Eye" principle,* Nature **244**, 281 (1973).

[118] A. R. Parker and H. E. Townley, *Biomimetics of photonic nanostructures,* Nature Nanotechnology **2**, 347 (2007).

[119] Y.-F. Huang, S. Chattopadhyay, Y.-J. Jen, C.-Y. Peng, T.-A. Liu, Y.-K. Hsu, C.-L. Pan, H.-C. Lo, C.-H. Hsu, Y.-H. Chang, C.-S. Lee, K.-H. Chen, and L.-C. Chen, *Improved broadband and quasi omnidirectional anti-reflection properties with biomimetic silicon nanostructures,* Nature Nanotechnology **2**, 770 (2008).

[120] J.-Q. Xi, M. Schubert, J. Kim, E. Schubert, M. Chen, S.-Y. Lin, W. Liu, and J. A. Smart, *Optical thin-film materials with low refractive index for broadband elimination of Fresnel reflection,* Nature Photonics **1**, 176 (2007).

[121] T.-H. Her, R. J. Finlay, C. Wu, S. Deliwala, and E. Mazur, *Microstructuring of silicon with femtosecond laser pulses,* Applied Physics Letters **73**, 1673 (1998).

[122] H. M. Branz, V. E. Yost, S. Ward, K. M. Jones, B. To, and P. Stradins, *Nanostructured black silicon and the optical reflectance of graded-density surfaces,* Applied Physics Letters **94**, 231121 (2009).

[123] H.-C. Yuan, V. E. Yost, M. R. Page, P. Stradins, D. L. Meier, and H. M. Branz, *Efficient black silicon solar cell with a density-graded nanoporous surface: optical properties, performance, limitations, and design rules,* Applied Physics Letters **95**, 123501 (2009).

[124] S. Koynov, M. S. Brandt, and M. Stutzmann, *Black nonreflecting silicon surfaces for solar cells,* Applied Physics Letters **88**, 203107 (2006).

[125] J. Zhu, Z. Yu, G. Burkhard, C.-M. Hsu, S. T. Connor, Y. Xu, Q. Wang, M. McGehee, S. Fan, and Y. Cui, *Optical absorption enhancement in amorphous silicon nanowire and nanocone arrays,* Nano Letters **9**, 279 (2009).

[126] J. Zhu, C.-M. Hsu, Z. Yu, S. Fan, and Y. Cui, *Nanodome solar cells with efficient light management and self-cleaning,* Nano Letters **10**, 1979 (2010).

[127] L. Hu and G. Chen, *Analysis of optical absorption in silicon nanowire arrays for photovoltaic applications,* Nano Letters **7**, 3249 (2007).

[128] S. L. Diedenhofen, G. Vecchi, R. E. Algra, A. Hartsuiker, O. L. Muskens, G. Immink, E. P. A. M. Bakkers, W. L. Vos, and J. Gómez Rivas, *Broadband and omnidirectional antireflection coating based on semiconductor nanorods,* Advanced Materials **21**, 973 (2009).

[129] O. L. Muskens, J. Gómez Rivas, R. E. Algra, E. P. A. M. Bakkers, and A. Lagendijk, *Designing light scattering in nanowire materials for photovoltaic applications,* Nano

Letters **8**, 2638 (2008).

[130] S. L. Diedenhofen, O. T. A. Janssen, G. Grzela, E. P. A. M. Bakkers, and J. Gómez Rivas, *Strong geometrical dependence of the absorption of light in arrays of semiconductor nanowires*, ACS Nano **5**, 2316 (2011).

[131] L. Cao, P. Fan, A. P. Vasudev, J. S. White, Z. Yu, W. Cai, J. A. Schuller, S. Fan, and M. L. Brongersma, *Semiconductor Nanowire Optical Antenna Solar Absorbers*, Nano Letters **10**, 439 (2010).

[132] J. W. S. Rayleigh, *Note on the remarkable case of diffraction spectra discovered by Prof. Wood*, Philosophical Magazine **14**, 60 (1907).

[133] S. Varlamov, J. Dore, R. Evans, D. Ong, B. Eggleston, O. Kunz, U. Schubert, T. Young, J. Huang, T. Soderstrom, K. Omaki, K. Kim, A. Teal, M. Jung, J. Yun, Z. M. Pakhuruddin, R. Egan, and M. A. Green, *Polycrystalline silicon on glass thin-film solar cells: A transition from solid-phase to liquid-phase crystallised silicon*, Solar Energy Materials & Solar Cells **119**, 246 (2013).

[134] C. Becker, D. Amkreutz, T. Sontheimer, V. Preidel, D. Lockau, J. Haschke, L. Jogschies, C. Klimm, J. J. Merkel, P. Plocica, S. Steffens, and B. Rech, *Polycrystalline silicon thin-film solar cells: Status and perspectives*, Solar Energy Materials & Solar Cells **119**, 112 (2013).

[135] J. H. Petermann, D. Zielke, J. Schmidt, F. Haase, E. G. Rojas, and R. Brendel, *19%-efficient and 43-µm-thick crystalline Si solar cell from layer transfer using porous silicon*, Progress in Photovoltaics: Research and Applications **20**, 1 (2012).

[136] F. Dross et al., *Crystalline thin-foil silicon solar cells: where crystalline quality meets thin-film processing*, Progress in Photovoltaics: Research and Applications **20**, 770 (2012).

[137] P. Spinelli, M. A. Verschuuren, and A. Polman, *Broadband omnidirectional antireflection coating using subwavelength surface Mie resonators*, Nature Communications **3**, 692 (2012).

[138] T. Coenen, J. van de Groep, and A. Polman, *Resonant Mie modes of single silicon nanocavities excited by electron irradiation*, ACS Nano **7**, 1689 (2013).

[139] M. van Lare, F. Lenzmann, M. A. Verschuuren, and A. Polman, *Mode coupling by plasmonic surface scatterers in thin-film silicon solar cells*, Applied Physics Letters **101**, 221110 (2012).

[140] S. De Wolf, A. Descoeudres, Z. C. Holman, and C. Ballif, *High-efficiency Silicon Heterojunction Solar Cells: A Review*, Green **2**, 7 (2012).

[141] A. Luque and S. Hegedus, *Handbook of Photovoltaic Science and Engineering*, Wiley, 2011.

[142] M. J. Kerr and A. Cuevas, *General parametrization of Auger recombination in crystalline silicon*, Journal of Applied Physics **91**, 2473 (2002).

[143] R. A. Sinton and A. Cuevas, *Contactless determination of current-voltage characteristic and minority carrier lifetimes in semiconductors from quasisteadystate photoconductance data*, Applied Physics Letters **69**, 2510 (1996).

[144] A. W. Snyder and J. D. Love, *Optical Waveguide Theory*, Chapman & Hall, 1983.

[145] J. van de Groep, *Light trapping in thin silicon waveguides by plasmon mediated mode coupling*, Master's thesis, Utrecht University, 2011.

[146] J. Zhao and M. A. Green, *Optimized antireflection coatings for high-efficiency silicon solar cells*, IEEE Transactions on Electronic Devices **38(8)**, 1925 (1991).

[147] G. Dingemans and W. M. M. Kessels, *Status and prospects of Al_2O_3-based surface passivation schemes for silicon solar cells*, Journal of Vacuum Science & Technology,

A: Vacuum, Surfaces, and Films **30(4)**, 040802 (2012).

[148] M. Otto, M. Kroll, T. Käsebier, R. Salzer, A. Tünnermann, and R. B. Wehrspohn, *Extremely low surface recombination velocities in black silicon passivated by atomic layer deposition*, Applied Physics Letters **100**, 191603 (2012).

[149] H. B. Profijt, P. Kudlacek, M. C. M. van de Sanden, and W. M. M. Kessels, *Ion and Photon Surface Interaction during Remote Plasma ALD of Metal Oxides*, Journal of Electrochemical Society **158**, G88 (2011).

[150] A. I. Kuznetsov, A. E. Miroshnichenko, Y. H. Fu, J. Zhang, and B. Luk'yanchuk, *Magnetic light*, Scientific Reports **2**, 492 (2012).

[151] B. S. Richards, *Single-material TiO_2 double-layer antireflection coatings*, Solar Energy Materials & Solar Cells **79**, 369 (2003).

[152] W. Soppe, H. Rieffe, and A. Weeber, *Bulk and Surface Passivation of Silicon Solar Cells Accomplished by Silicon Nitride Deposited on Industrial Scale by Microwave PECVD*, Progress in Photovoltaics: Research and Applications **13**, 551 (2005).

[153] J. Schmidt and A. Cuevas, *Electronic properties of light-induced recombination centers in boron-doped Czochralski silicon*, Journal of Applied Physics **1999**, 3175 (86).

[154] S. W. Glunz, S. Rein, J. Y. Lee, and W. Warta, *Minority carrier lifetime degradation in boron-doped Czochralski silicon*, Journal of Applied Physics **90**, 2397 (2001).

[155] D. Macdonald, F. Rougieux, A. Cuevas, B. Lim, J. Schmidt, M. Di Sabatino, and L. J. Geerligs, *Light-induced boron-oxygen defect generation in compensated p-type Czochralski silicon*, Journal of Applied Physics **105**, 093704 (2009).

[156] D. Macdonald and L. J. Geerligs, *Recombination activity of interstitial iron and other transition metal point defects in p- and n-type crystalline silicon*, Applied Physics Letters **85**, 4061 (2004).

[157] J. Schmidt, A. Merkle, R. Brendel, B. Hoex, M. C. M. van de Sanden, and W. M. M. Kessels, *Surface passivation of high-efficiency silicon solar cells by atomic-layer-deposited Al_2O_3*, Progress in Photovoltaics: Research and Applications **16**, 461 (2008).

[158] G. Dingemans, *Nanolayer surface passivation schemes for silicon solar cells*, PhD thesis, Eindhoven University of Technology, 2011.

[159] B. M. Kayes, H. Nie, R. Twist, S. G. Spruytte, F. Reinhardt, I. C. Kizilyalli, and G. S. Higashi, *27.6% conversion efficiency, a new record for single-junction solar cells under 1 sun illumination*, 2011.

[160] A. W. Snyder and W. R. Young, *Modes of optical waveguides*, Journal of Optical Society of America **68**, 297 (1978).

[161] S. Person, M. Jain, Z. Lapin, J. J. Sàenz, G. Wicks, and L. Novotny, *Demonstration of Zero Optical Backscattering from Single Nanoparticles*, Nano Letters **13**, 1806 (2013).

[162] M. Kerker, D. Wang, and C. L. Giles, *Electromagnetic scattering by magnetic spheres*, Journal of Optical Society of America **73**, 765 (1983).

[163] Y. H. Fu, A. I. Kuznetsov, A. E. Miroshnichenko, Y. F. Yu, and B. Luk'yanchuk, *Directional visible light scattering by silicon nanoparticles*, Nature Communications **4**, 1527 (2013).

[164] W. Ma, C. Yang, X. Gong, K. Lee, and A. J. Heeger, *Thermally Stable, Efficient Polymer Solar Cells with Nanoscale Control of the Interpenetrating Network Morphology*, Advanced Functional Materials **15**, 1617 (2005).

[165] J. Y. Kim, K. Lee, N. E. Coates, D. Moses, T.-Q. Nguyen, M. Dante, and A. J. Heeger, *Efficient Tandem Polymer Solar Cells Fabricated by All-Solution Processing*, Science **317**, 222 (2007).

[166] C. Uhrenfeldt, T. F. Villesen, B. Johansen, J. Jung, T. G. Pedersen, and A. Nyland-

sted Larsen, *Diffractive coupling and plasmon-enhanced photocurrent generation in silicon*, Optics Express **21**, A774 (2013).

[167] P. Spinelli, C. van Lare, E. Verhagen, and A. Polman, *Controlling Fano lineshapes in plasmon-mediated light coupling into a substrate*, Optics Express **19**, 303 (2011).

[168] M. van Lare, F. Lenzmann, and A. Polman, *Dielectric back scattering patterns for light trapping in thin-film Si solar cells*, Optics Express **21**, 20738 (2013).

[169] J. Moghal, J. Kobler, J. Sauer, J. Best, M. Gardener, A. A. R. Watt, and G. Wakefield, *High-Performance, Single-Layer Antireflective Optical Coatings Comprising Mesoporous Silica Nanoparticles*, ACS Applied Materials & Interfaces **4**, 854 (2012).

[170] K.-C. Park, H. J. Choi, C.-H. Chang, R. E. Cohen, G. H. McKinley, and G. Barbastathis, *Nanotextured Silica Surfaces with Robust Superhydrophobicity and Omnidirectional Broadband Supertransmissivity*, ACS Nano **6**, 3789 (2012).

Summary

Photovoltaics is a sustainable and environmentally clean source of energy that has the potential to become a major source of energy for our society. In order for this to happen, photovoltaics needs to be economically competitive with other conventional energy sources. This can be achieved by reducing the production costs of solar panels and by improving their photovoltaic conversion efficiency. For Si solar cells, both challenges can be achieved by reducing the thickness of the solar cell. However, major optical losses occur when the thickness of Si solar cell is reduced, due to incomplete absorption of light.

In this thesis, we investigate new ways of enhancing light absorption in Si solar cells by using nanostructures that show resonant interaction with light. We study the fundamental aspects of resonant scattering of light by metallic and dielectric nanoparticles placed on top of thick and thin dielectric substrates. If optimally designed these nanostructures can lead to efficient light coupling and trapping in solar cells. This allows the realization of novel solar cell architectures with higher efficiency that can be made at lower costs.

Chapter 2 presents the nanofabrication techniques used to fabricate the nanoparticles. Substrate conformal imprint lithography (SCIL) is presented as a large area, non-expensive, high-fidelity technique to fabricate nanoparticle arrays on full wafers. Furthermore, a reactive ion etching (RIE) recipe based on fluorine compound gases is used to fabricate Si nano-pillar arrays on large-area Si wafers.

In Chapter 3, we study with numerical simulations the scattering of light by Ag plasmonic nanoparticles placed on a substrate. In particular, we identify the key role of Fano resonances and we define guidelines for designing a plasmonic antireflection coating (ARC) for Si solar cells.

Based on these results, in Chapter 4 we demonstrate that an optimized array of plasmonic Ag nanoparticles placed on top of a Si wafer provides an effective antireflection effect which outperforms a standard Si_3N_4 coating. This is a result of a full parameter space optimization carried out with numerical simulations. We use electron beam lithography (EBL) to fabricate Ag nanoparticle arrays on crystalline Si solar cells. Reflection spectroscopy is used to quantify the light coupling into the Si solar cells.

In Chapter 5 we discuss the possibility to use the near-field enhancement of plasmonic (Ag) nanoparticles embedded in a solar cell, to enhance the absorption of light in the active layer of the cell. We find that this approach cannot be used for crystalline or amorphous Si solar cells as Ohmic losses in the metal nanoparticles dominate over the absorption in the semiconductor. However, Ag nanoparticles can be used to enhance the absorption of light in ultrathin organic/polymer based solar cells.

Chapter 6 presents a new way of suppressing the reflection of light from a Si surface. The reflectivity of a full-size Si wafer is reduced from over 35% to 1.3% (averaged over the solar spectrum) by covering the wafer with an optimized array of Si Mie resonators. The wafer patterned with a Si nanoparticle array appears thus completely black. The low reflectivity is maintained for angles of incidence up to 60°. Several fundamental aspects of light scattering by Mie resonances in the Si nanoparticles and the coupling into the substrate are studied.

The same Si Mie coating is used in Chapter 7 to study light trapping in thin (20-100 μm) and ultrathin (1-20 μm) crystalline Si solar cells. We use numerical simulations to calculate the absorption in the thin Si slab covered with the Si Mie coating. An electrical model including bulk and surface recombination is then used to estimate the solar cell efficiency. We demonstrate that for realistic values of surface recombination velocity and carrier bulk lifetime, 20-μm-thick Si solar cells with efficiency of 21.5% can be made.

In Chapter 8 we experimentally demonstrate light trapping beyond the Lambertian $4n^2$ limit using Si Mie nanoscatterers. Thin film polycristalline Si layers are made on glass and patterned with an array of Si nanocylinders. Total reflection and transmission spectroscopy is used to measure the absorption spectrum of the thin Si slab with the Si Mie coating, and compare it to that of a flat Si slab. In the infrared spectral range, optical path length enhancements up to a factor of 65 are measured, well beyond the geometric Lambertian $4n^2$ limit for Si at this wavelength.

Chapter 9 presents a TiO_2/Al_2O_3 Mie coating that combines very good antireflection properties with excellent surface passivation. The antireflection effect stems from the preferential forward scattering of light by Mie resonances in the TiO_2 nanoparticles and yields a solar-spectrum averaged reflectivity as low as 1.6%. An ultrathin Al_2O_3 layer provides excellent passivation of the Si surface, with a surface recombination velocity of only 3.3 cm/s after fabrication of the TiO_2 nanoparticles.

Finally, Chapter 10 presents several new concepts and ideas for integrating plasmonic and Mie nanoparticles on realistic solar cell designs. We show that resonant nanostructures can be beneficial not only for several crystalline Si solar cell designs, but also for GaAs and polymer cells. Practical aspects such as the effect of polymer and glass encapsulation of solar modules are also analyzed.

Overall, this thesis provides new fundamental insights in light scattering and trapping by resonant metallic and dielectric nanoparticles integrated with solar cells. The results may be used to design Si solar cell with higher efficiency that can be made at lower costs.

Samenvatting

Photovoltaica is een duurzame en milieuvriendelijke schone bron van energie die de potentie heeft om een substantiële bron van energie te worden voor onze samenleving. Om dit te laten gebeuren moet photovoltaica competitief zijn met andere conventionele energiebronnen. Dit kan worden bereikt door de productiekosten van zonnepanelen te reduceren en hun photovoltaïsche conversie-efficiëntie te verbeteren. Voor Si zonnecellen kunnen beide uitdagingen opgelost worden door de dikte van de zonnecel te reduceren. Er treden echter grote verliezen op bij het reduceren van de dikte van de zonnecel door incomplete absorptie van het licht.

In dit proefschrift onderzoeken we nieuwe manieren om de lichtabsorptie in Si zonnecellen te verbeteren door het gebruik van nanostructuren die een resonante interactie hebben met licht. We bestuderen de fundamentele aspecten van resonante verstrooiing van licht door metalen en diëlektrische nanodeeltjes geplaatst op dikke en dunne diëlektrische substraten. Mits goed ontworpen kunnen deze nanostructuren zorgen voor het efficiënt inkoppelen en opsluiten van licht in zonnecellen. Hierdoor kunnen nieuwe zonnecelarchitecturen gerealiseerd worden met hogere efficiëntie die voor lagere kosten gefabriceerd kunnen worden.

Hoofdstuk 2 presenteert de nanofabricagetechnieken die gebruikt worden om de nanodeeltjes te fabriceren. Substrate conformal imprint lithography (SCIL) wordt gepresenteerd als een techniek waarmee grote oppervlakken met nanodeeltjes goedkoop en met grote precisie gefabriceerd kunnen worden. Verder wordt er een reactive ion etching (RIE) recept gebruikt dat is gebaseerd op fluorbevattende gassen om Si nanopilaarroosters te fabriceren op silicium wafers met een groot oppervlak.

In Hoofdstuk 3 bestuderen we de verstrooiing van licht door plasmonische Ag nanodeeltjes op een substraat met behulp van numerieke simulaties. In het bijzonder identificeren we de belangrijke rol van Fano resonanties en definiëren we belangrijke richtlijnen voor het ontwerpen van een plasmonische antireflectiecoating (ARC) voor Si zonnecellen.

Gebaseerd op deze resultaten laten we in Hoofdstuk 4 zien dat een geoptimaliseerd rooster van plasmonische Ag deeltjes op een silicium wafer zorgt voor een effectief antireflectie-effect dat beter is dan dat van een standaard Si_3N_4 coating.

Dit is het resultaat van een optimalisatie van de volledige parameterruimte. We gebruiken elektronenbundellithografie (EBL) om roosters van Ag nanodeeltjes te fabriceren op Si zonnecellen. Reflectie-spectroscopie wordt gebruikt om de lichtinkoppeling in het substraat te kwantificeren.

In Hoofdstuk 5 bespreken we de mogelijkheid om de nabije-veld versterking van plasmonische Ag nanodeeltjes die in de zonnecel zijn ingebed te gebruiken om de absorptie van licht in de actieve laag van de cel te versterken. Onze bevinding is dat deze aanpak niet kan worden gebruikt voor kristallijne of amorfe Si zonnecellen omdat de Ohmische verliezen in de metalen deeltjes sterker zijn dan de absorptie in de halfgeleider. Ag nanodeeltjes kunnen echter wel worden gebruikt om de absorptie van licht te versterken in ultradunne organische/polymeer zonnecellen.

Hoofdstuk 6 presenteert een nieuwe manier om de reflectie van licht van een Si oppervlak te onderdrukken. De reflectiviteit van een volledige wafer wordt gereduceerd van meer dan 35% naar 1.3% (gemiddeld over het zonnespectrum) door de wafer te bedekken met een geoptimaliseerd rooster van Si Mie resonatoren. De wafer met dit patroon erop lijkt dus helemaal zwart. De lage reflectiviteit blijft behouden voor hoeken van inval tot ± 60 graden. Diverse fundamentele aspecten van lichtverstrooiing door Mie resonanties in de Si deeltjes en de koppeling naar het substraat worden bestudeerd.

Dezelfde Si Mie coating wordt gebruikt in Hoofdstuk 7 om het opsluiten van licht te bestuderen in dunne (20-100 μm) en ultradunne (1-20 μm) kristallijne Si zonnecellen. We gebruiken numerieke simulaties om de absorptie te berekenen in de dunne Si laag die bedekt is met de Si Mie coating. Vervolgens wordt er een elektrisch model gebruikt dat de bulk- en oppervlakte-recombinatie meeneemt om de rendement van zonnecel te berekenen. We laten zien dat met realistische waardes voor oppervlakterecombinatiesnelheid en bulklevensduur van de ladingsdragers, 20-μm dikke Si zonnecellen met een efficiëntie van 21.5% realiseerbeer zijn.

In Hoofdstuk 8 demonstreren we experimenteel dat licht kan worden opgesloten voorbij de Lambertiaanse $4n^2$ limiet door middel van Si Mie nanoverstrooiers. Dunne-film polykristallijne Si lagen worden gedeponeerd op glas en voorzien van een rooster van Si nanocylinders. Totale reflectie- en transmissie-spectroscopie wordt gebruikt om het absorptiespectrum van de dunne siliciumlaag met de Si Mie coating te meten en te vergelijken met die van een vlakke Si laag. In het infrarode deel van het spectrum meten we optische padlengtevergrotingen tot een factor 65 wat significant meer is dan de geometrische Lambertiaanse $4n^2$ limiet voor Si bij deze golflengte.

Hoofdstuk 9 presenteert een TiO_2/Al_2O_3 Mie coating die hele goede antireflectie eigenschappen combineert met een uitmuntende oppervlaktepassivatie. Het antireflectie-effect wordt veroorzaakt doordat de Mie resonanties in de TiO_2 nanodeeltjes het licht preferentieel voorwaarts verstrooien, wat leidt tot een zeer lage reflectiviteit van 1.6% gemiddeld over het zonnespectrum. Een ultradunne Al_2O_3 laag zorgt voor zeer goede passivatie van het Si oppervlak, met oppervlakterecombinatiesnelheden van slechts 3.3 cm/s na fabricage van TiO_2 nanodeeltjes.

Ten slotte presenteren we in Hoofdstuk 10 een aantal nieuwe concepten en

ideeën voor de integratie van plasmonische en Mie nanodeeltjes met realistische ontwerpen van zonnecellen. We laten zien dat resonante nanostructuren niet alleen helpen voor een aantal ontwerpen van kristallijne Si zonnecellen, maar ook voor GaAs en polymeer zonnecellen. Praktische aspecten zoals het effect van polymeer- en glas-encapsulatie van zonnemodules worden ook geanalyseerd.

Samenvattend geeft dit proefschrift nieuwe fundamentele inzichten in het verstrooien en opsluiten van licht door resonante metalen en diëlektrische nanodeeltjes die zijn geïntegreerd met zonnecellen. De resultaten kunnen worden gebruikt om Si zonnecellen te ontwerpen met een hoger rendement die gefabriceerd kunnen worden voor lagere kosten.

Riassunto

Il fotovoltaico è una fonte di energia pulita e rinnovabile, che ha grandi potenzialità per soddisfare i bisogni energetici della nostra società. Perché questo avvenga, è necessario che il fotovoltaico divenga economicamente competitivo rispetto ad altre fonti di energia convenzionali. Per ridurre il costo dell'energia solare bisogna da un lato ridurre i costi di produzione dei pannelli solari e dall'altro migliorarne l'efficienza di conversione. Per celle solari in silicio, entrambi gli obiettivi possono essere raggiunti riducendo lo spessore della cella solare. In questo caso, tuttavia, la cella fotovoltaica non assorbe tutta la radiazione solare, causando pertanto perdite di efficienza sostanziali.

In questa tesi sono presentate nuove idee per incrementare l'assorbimento della luce in celle solari in silicio a film sottile, usando nanoparticelle che interagiscono con la luce in maniera risonante. In particolare, sono studiati gli aspetti fondamentali di come nanoparticelle dielettriche o metalliche poste su un substrato dielettrico diffondono la luce in risonanza. Ottimizzando la geometria delle nanoparticelle è possibile forzare e intrappolare la luce all'interno di una cella solare, aumentandone l'assorbimento. Utilizzando questo effetto è possibile realizzare celle solari più efficienti e a costi ridotti.

Il capitolo 2 introduce le tecniche di nano-fabbricazione utilizzate per realizzare i campioni con nanoparticelle. La "Litografia tramite Imprint Conforme al Substrato" (SCIL) è una tecnica che può essere utilizzata per fabbricare una matrice di nanoparticelle su un wafer di silicio in maniera non costosa, con alta riproducibilità e su larga scala. In aggiunta alla SCIL, un'altra tecnica presentata nel capitolo 2 è l'etching con ioni reattivi (RIE). Questa tecnica utilizza un gas contenente fluoro con il quale è possibile incidere nano-cilindri di silicio su un wafer di silicio.

Nel capitolo 3 viene analizzato, tramite simulazioni numeriche, il processo di diffusione della luce da parte di nanoparticelle di argento con proprietà plasmoniche, collocate sulla superficie di un substrato dielettrico. Nello specifico, sono studiate le risonanze di Fano, che svolgono un ruolo importante nel determinare la direzionalità della luce diffusa. Cambiando le proprietà ottiche delle nanoparticelle è possibile ridurre la riflessione della luce in una cella solare in silicio, incrementandone pertanto l'assorbimento.

Alla luce di questi risultati, nel capitolo 4 una matrice di nanoparticelle di argento, disposte in un reticolo quadrato, viene utilizzata per sopprimere la riflessione della luce in celle solari in silicio. La matrice di nanoparticelle di argento permette di ottenere risultati migliori di quelli ottenuti con un rivestimento antiriflessione in nitruro di silicio, comunemente utilizzato per celle solari in silicio cristallino. Questo importante risultato è stato ottenuto tramite un'ottimizzazione della geometria delle nanoparticelle. La matrice di nanoparticelle di argento è stata fabbricata su una cella solare in silicio, utilizzando la litografia con fascio elettronico (EBL). In seguito, misure di spettroscopia ottica sono state eseguite per verificare la riduzione della riflessione della luce.

Nel capitolo 5 viene studiata un'altra configurazione di particelle plasmoniche di argento. A differenza dei capitoli precedenti, le nanoparticelle sono disposte all'interno di una cella solare. In questo caso, il campo elettrico in prossimità della nanoparticella è potenziato significativamente, e pertanto si può ottenere un maggiore assorbimento della luce. Utilizzando simulazioni numeriche, si dimostra che questo approccio è limitato da sostanziali perdite ottiche nelle nanoparticelle metalliche. Pertanto, celle solari in silicio cristallino o amorfo non possono trarre vantaggio da particelle plasmoniche collocate all'interno del materiale. Le nanoparticelle di argento tuttavia possono essere usate per migliore l'assorbimento della luce in celle solari a film sottile realizzate con materiali organici o polimerici.

Il capitolo 6 presenta un nuovo modo per sopprimere la riflessione della luce di una superficie di silicio. Ricoprendo la superficie di un wafer di silicio con una matrice di nanoparticelle dielettriche (risonatori ottici di Mie) è possibile ridurne la riflettività da 35% a 1.3% (media pesata sullo spettro solare). A causa di questa riduzione della riflettività, il wafer di silicio diventa nero. La riflettività è ridotta anche quando l'angolo di incidenza della luce sul campione raggiunge i 60 gradi. Questo capitolo analizza in dettaglio la fisica della diffusione della luce tramite risonanze di Mie in nanoparticelle dielettriche.

La stessa matrice di risonatori di Mie, utilizzata nel capito 6 per ridurre la riflessione della luce, è utilizzata nel capitolo 7 per intrappolare la luce in celle solari in silicio a film sottile (20-100 μm) o ultrasottile (1-20 μm). Utilizzando simulazioni numeriche è possibile calcolare l'assorbanza ottica di film sottili di silicio ricoperti con una matrice di nano-cilindri di silicio. Il valore dell'assorbanza può essere quindi usato per calcolare analiticamente l'efficienza di una cella solare a film sottile, assumendo stime realistiche per le probabilità di ricombinazione di bulk e di superficie. Per celle solari con uno spessore di 20 μm, possono essere ottenute efficienze oltre il 20%.

Nel capitolo 8 viene dimostrato sperimentalmente l'intrappolamento della luce in un film sottile (1 μm) di silicio policristallino, fabbricato su un substrato di vetro. Il film di silicio è ricoperto da una matrice di nano-cilindri di silicio. Misurando gli spettri di trasmissione e riflessione, è possibile ottenere lo spettro di assorbimento per il film di silicio con risonatori di Mie, e compararlo con un film di silicio non ricoperto. Nell'infrarosso, viene misurato un aumento del percorso ottico della luce di un fattore pari a 65. Questo aumento è più alto di quello calcolato nel limite

Lambertiano ($4n^2$) in questo intervallo di lunghezze d'onda.

Il capitolo 9 introduce un nuovo ricoprimento per celle solari in silicio, reallizzato con risonatori di Mie. Questo ricoprimento consiste in uno strato ultrasottile (5 nm) di ossido di alluminio e in una matrice di nano-cilindri di ossido di titanio. Questo ricoprimento consente non solo di ridurre la riflettività del silicio, ma anche di ottenere la passivazione della superficie del silicio. L'effetto di anti-riflessione è ottenuto grazie alla diffusione della luce tramite risonanze di Mie nelle nanoparticelle di ossido di titanio. La passivazione invece è ottenuta grazie allo strato sottile di ossido di alluminio. Utilizzando tali risonatori di Mie, si ottengono una riflettività pari a 1.6% e una velocità di ricombinazione di superficie pari a 3.3 cm/s.

Infine, il capitolo 10 presenta diversi concetti e nuove idee riguardanti l'integrazione delle nanostrutture risonanti studiate nella tesi in celle solari commerciali. Queste nanostrutture infatti possono migliorare l'efficienza non solo di celle solari in silicio cristallino, ma anche in arsenuro di gallio o di celle solari organiche. Vengono inoltre analizzati gli effetti pratici dell'incapsulamento delle nanostrutture nel polimero o nel vetro utilizzati nei pannelli solari.

Riassumendo, questa tesi studia sia gli aspetti fondamentali che quelli applicativi della diffusione della luce da parte di nanoparticelle dielettriche o metalliche con risonanze ottiche, integrate in celle solari. I risultati ottenuti in questa tesi permettono di ideare celle solari con efficienze di conversione più elevate, che possono essere realizzate a costi ridotti.

List of publications

This thesis is based on the following publications:

- *Controlling Fano lineshapes in plasmon-mediated light coupling into a substrate*, P. Spinelli, M. van Lare, E. Verhagen and A. Polman, Optics Express **19**, A303-A311 (2011). **(Chapter 3)**
- *Optical impedance matching using coupled plasmonic nanoparticle arrays*, P. Spinelli, M. Hebbink, R. de Waele, L. Black, F. Lenzmann and A. Polman, Nano Letters **11**, 1760-1765 (2011). **(Chapter 4)**
- *Prospects of near-field plasmonic absorption enhancement in semiconductor materials using embedded Ag nanoparticles*, P. Spinelli and A. Polman, Optics Express **20**, A641-A654 (2012). **(Chapter 5)**
- *Broadband omnidirectional antireflection coating based on subwavelength surface Mie resonators*, P. Spinelli, M. A. Verschuuren and A. Polman, Nature Communications **3**, 692 (2012). **(Chapter 6)**
- *Light trapping in thin crystalline Si solar cells using surface Mie scatterers*, P. Spinelli and A. Polman, IEEE Journal of Photovoltaics **3**, in press (2013). **(Chapter 7)**
- *Experimental demonstration of light trapping beyond the $4n^2$ limit in thin Si slabs using resonant surface Si Mie scatterers*, P. Spinelli, C. Teplin, M. A. Verschuuren and A. Polman, in preparation. **(Chapter 8)**
- *Al_2O_3/TiO_2 nano-pattern antireflection coating with ultralow surface recombination*, P. Spinelli, B. Macco, M. A. Verschuuren, W. M. M. Kessels and A. Polman, Applied Physics Letters **102**, 233902 (2013). **(Chapter 9)**
- *Effect of EVA encapsulation on light trapping in thin-film c-Si solar cells by using plasmonic and Mie nanoscatterers*, P. Spinelli, B. Newman and A. Polman, in preparation. **(Chapter 10)**

Other publications by the author:

- *Microphotonic parabolic light directors fabricated by two-photon lithography*, J. H. Atwater, P. Spinelli, E. D. Kosten, J. Parsons, M. van Lare, J. van de Groep, F. J. García de Abajo, A. Polman and H. A. Atwater, Applied Physics Letters **99**, 151113 (2011).
- *Plasmonic light trapping in thin-film Si solar cells*, P. Spinelli, V. E. Ferry, J. van de Groep, M. van Lare, M. A. Verschuuren, R. E. I. Schropp, H. A. Atwater and A. Polman, Journal of Optics **14**, 024002 (2012).
- *Transparent conducting silver nanowire networks*, J. van de Groep, P. Spinelli and A. Polman, Nano Letters **12**, 3138-3144 (2012).

Acknowledgements

Many people helped me with the realization of the work presented in this thesis.

First and foremost I would like to thank my supervisor Albert Polman. Albert, hartelijk bedankt voor jouw hulp en begeleiding. It was really a great pleasure for me to work in your group. I learned a lot from you, both scientifically and from a personal point of view. Your enthusiasm and your always constructive criticism, were very important for the success of this work. Thank you also for always encouraging me to present our work at so many conferences.

This thesis is the result of lots of discussions, ideas, comments and feedback received from the Photonic Materials PV team: Maarten Hebbink, René de Waele, Claire van Lare, Jorik van de Groep, Vivian Ferry, Hugo Doeleman, Bonna Newman, and Lourens van Dijk. Maarten and René, thank you for helping me to get started with the FDTD simulation world. Claire and Jorik, you have been the "hard-core" of the PV team in these four years. It has been absolutely great to work with you. Claire, thank you for teaching me the nanoimprint lithography and for all the nice time we had at the conferences. Jorik, thank you for your help in the optics lab and for your always-sharp questions that have constantly been a "reality check" for my results. Vivian, Hugo, Bonna and Lourens, our collaboration has been short but intense. We had lots of interesting discussions and shared many ideas on PV. Thank you very much and I hope to be in touch with you in future.

I owe a big thank you to Marc Verschuuren. The experimental part of this thesis could not be possible without your help. Thank you for the several collaborations and for being a constant source of advice for everything related to nanofabrication.

I would like to thank all the group members of the Photonic Materials group I had the pleasure to work with during these four years. Ewold Verhagen, Robb Walters, James Parsons, Ernst Jan Vesseur, Toon Coenen, Rutger Thijssen, Ruben Maas, Bas Zegers, MarieAnne van de Haar, and Benjamin Brenny, I have learned a lot from all of you during our weekly group meetings. Toon, MarieAnne and Jorik, it was a lot of fun to be in the office with you, and very productive as well, despite the constant chatting!

Being a PhD at Amolf gives you the possibility to interact with many people in the Nanophotonics department. I would like to thank them all for the useful dis-

cussions, for the fair and direct feedback received in the Nanophotonics Colloquia and poster sessions, and for the enjoyable activities outside the working hours.

At the beginning of my PhD, there were not so many people involved in solar cell research at Amolf. Luckily for me, this number has significantly grown during this four year and I have been able to learn a lot on PV from all these people. I would like to thank the people involved in the Nano-Photovoltaics program: Jaime Gomez-Rivas, Silke Diedenhofen, Grzegorz Grzela, Mischa Bonn, Enrique Canovas, Søren Jensen. Grzegorz, thank you very much for your help with the optical measurements in Eindhoven. Furthermore, I would like to thank the Nanoscale Solar Cells group: Erik, Sander, Sebastian, Beniamino, and Cristina for the enjoyable and interesting discussions.

One of the great aspects of doing research at Amolf is that you have chance to collaborate with many people all over the world. First, I would like to thank Harry Atwater for having invited and hosted me at Caltech for almost 6 months. It was a great experience for me, and I learned on-the-job how challenging making a solar cell can be! Thank you Dennis Callahan and Ragip Pala for working together on GaAs solar cells and for the interesting discussions we had in the coffee breaks.

My first and most long-lived collaboration has been with ECN. I would like to thank Frank Lenzmann and Lachlan Black for providing me with silicon solar cells on which I could test my nanostructures. I enjoyed not only our scientific discussions but also the chats on socio-economic aspects of PV. Furthermore, I had an extremely enjoyable and efficient collaboration with Bart Macco and Erwin Kessels from the TUE. It was amazing to see our collaboration leading to a nice publication in only a few weeks! Finally, I would like to thank Chaz Teplin from NREL for the very recent collaboration on light trapping in thin Si cells.

Most of the nanofabrication work presented in this thesis was carried in the Amsterdam Nanocenter at Amolf. I owe big thanks to all the technicians who keep it running smoothly: Hans Zeijlemaker, Gijs Vollenbroek, Chris Rétif, Dimitry Lamers, and Andries Lof. Thank you also for your help and training. In a similar way, the simulation part of this thesis could not be possible without the support of the Amolf ICT department. In particular, I would like to thank Wiebe de Boer, Jan van Elst and Carl Schulz for my endless requests of help with setting up the FDTD licenses. Thank you also John Donners from SARA for the support with the Lisa supercomputer facilities.

Life in Amsterdam was not only work, fortunately! Thank you Marco Baggio for the uncounted espressi we had together in the weekends. It was great to have a chat with you, even if it was often on Italian politics. Thank you also to Nastia, Adrien, Ivan, Francesca, Elena, Vito, Marco, Alessandro, and Angela for visiting me in Amsterdam, hosting me and travelling with me all over Europe (and China). My biggest thank you goes to Beata who has always supported me, cheered for me, and who is my best travel mate. Dziekuje bardzo kochanie.

Per finire, ultimi ma non per questo meno importanti, vorrei ringraziare i miei genitori e le mie sorelle per il supporto e la fiducia che mi hanno sempre dato. Dedico a voi questa tesi.

About the author

Pierpaolo (Piero) Spinelli was born in Putignano, Italy, on April 24, 1985. After receiving his high school diploma from the Liceo Scientifico "E. Majorana" in Putignano in 2004, he studied Physics at the University of Padova, Italy. He graduated cum laude in 2009, with a thesis on ferromagnetic semiconductors, which was prepared during a 6-month internship at the Interuniversity Center for Micro Electronics (IMEC) in Leuven, Belgium. In 2009, he also graduated from the Scuola Galileiana di Studi Superiori, a higher learning institution in Padova.

In 2010 he started working as a PhD-student at the FOM Institute for Atomic and Molecular Physics (AMOLF) in Amsterdam, The Netherlands, under the supervision of prof. dr. Albert Polman. The results of this project are presented in this thesis. During his PhD, he spent a period of 6 months at the California Institute of Technology in the group of prof. Harry Atwater, working on light trapping in GaAs solar cells.

Besides his scientific interests, Piero is also interested in economics, finance and aviation. In his free time, Piero enjoys biking, cooking and travelling.

The work described in this thesis was performed at the FOM Institute AMOLF, Science Park 104, 1098 XG Amsterdam, The Netherlands.